

# Development of a high-accuracy continuous CO<sub>2</sub>/CH<sub>4</sub>/H<sub>2</sub>O analyzer for deployment on board a commercial airliner

## Dissertation

zur Erlangung des akademischen Grades doctor rerum naturalium  
(Dr. rer. nat.)

durchgeführt am Max-Planck-Institut für Biogeochemie Jena

vorgelegt dem Rat der Chemisch-Geowissenschaftlichen Fakultät der  
Friedrich-Schiller-Universität Jena



von Huilin Chen  
geboren am 18 April 1980 in Jilin, China

Gutachter:

1. Prof. Dr. Wolfgang Weigand Friedrich-Schiller-Universitaet Jena
2. Prof. Dr. Martin Heimann Max-Planck-Institut fuer Biogeochemie, Jena

Datum der öffentlichen Verteidigung: Sep. 17, 2010

# Table of contents

<b>Abstract.....</b>	<b>III</b>
<b>Kurzfassung.....</b>	<b>V</b>
<b>List of abbreviations and acronyms .....</b>	<b>VIII</b>
<b>Chapter 1 Introduction.....</b>	<b>1</b>
1.1 Background.....	1
1.1.1 Greenhouse gases.....	1
1.1.2 The carbon cycle .....	3
1.1.3 Climate change.....	5
1.1.4 Understanding the sources and sinks .....	6
1.2 Atmospheric CO <sub>2</sub> and CH <sub>4</sub> monitoring .....	8
1.2.1 Observational platforms.....	8
1.2.2 Observational networks .....	10
1.3 The commercial airliner programs.....	12
1.3.1 Overview of existing/past programs .....	12
1.3.2 The IAGOS-DS/ IAGOS-ERI project.....	16
1.4 Thesis outline.....	18
1.5 References.....	20
<b>Chapter 2 Advancing the techniques for high-accuracy continuous measurements of CO<sub>2</sub>/CH<sub>4</sub>/H<sub>2</sub>O on board a commercial airliner.....</b>	<b>25</b>
2.1 Introduction.....	25
2.2 Measurement techniques.....	28
2.2.1 The Beer-Lambert law .....	28
2.2.2 The NDIR technique .....	30
2.2.3 The CRDS technique .....	32
2.2.4 Other techniques .....	34
2.3 Characterization and advancement of an NDIR analyzer.....	37
2.3.1 The NDIR analyzer .....	37
2.3.2 System stability and linearity.....	39
2.3.3 Flow modifications .....	44
2.3.4 The calibration system .....	47
2.3.5 Performance under simulated flight conditions .....	49
2.4 Characterization and advancement of a CRDS analyzer .....	51
2.4.1 The CRDS analyzer .....	52
2.4.2 System stability and linearity.....	54
2.4.3 Water corrections .....	56

2.4.4 Water calibrations .....	65
2.4.5 Performance under simulated flight conditions .....	67
2.5 Summary and outlook.....	70
2.6 References.....	71
<b>Chapter 3 Validation of in situ airborne CO<sub>2</sub>/CH<sub>4</sub> measurements .....</b>	<b>77</b>
3.1 Introduction.....	77
3.2 Methodology for comparison of in situ with flask measurements.....	79
3.2.1 Flask sampler .....	80
3.2.2 Method for comparison of in situ with single flask measurements .....	82
3.2.3 Method for comparison of in situ with paired flask measurements.....	84
3.3 Validation of regular airborne in situ CO <sub>2</sub> profiles over Bialystok Tall Tower .....	88
3.3.1 Comparison of in situ with flask CO <sub>2</sub> measurements .....	90
3.3.2 Corrections for the bias due to insufficient drying .....	92
3.4 Validation of airborne CO <sub>2</sub> /CH <sub>4</sub> measurements using the CRDS technique.....	95
3.4.1 Stability of measurements of CO <sub>2</sub> concentrations by the CRDS analyzer .....	96
3.4.2 Accuracy of in situ CO <sub>2</sub> and CH <sub>4</sub> measurements during BARCA .....	110
3.5 Conclusions.....	114
3.6 References.....	115
<b>Chapter 4 Representativeness analysis of aircraft CO/CO<sub>2</sub> profiles .....</b>	<b>118</b>
4.1 Introduction.....	118
4.2 Representativeness analysis of CO profiles from a commercial airliner program	122
4.2.1 Statistical analysis of CO profiles over Frankfurt.....	122
4.2.2 Representativeness of CO profiles over Frankfurt.....	128
4.3 Representativeness analysis of CO/CO <sub>2</sub> profiles from a remote site.....	141
4.3.1 Spatial variability of mixed-layer CO <sub>2</sub> averages.....	141
4.3.2 Representativeness of aircraft CO/CO <sub>2</sub> profiles .....	144
4.4 Conclusions and discussion .....	149
4.5 References.....	150
<b>Chapter 5 Conclusions and future work.....</b>	<b>155</b>
<b>Appendix A.....</b>	<b>161</b>
A1. Single flask model.....	161
A2. Paired flask model.....	164
<b>Acknowledgements .....</b>	<b>171</b>
<b>CURRICULUM VITAE.....</b>	<b>174</b>
<b>Selbständigkeitserklärung.....</b>	<b>175</b>

## Abstract

Observations of atmospheric CO<sub>2</sub>, CH<sub>4</sub>, and H<sub>2</sub>O mixing ratios are of central interest for understanding the global carbon cycle and the impact of these greenhouse gases on climate change. Airborne measurements provide important information about vertical and horizontal distribution of trace gases. Using commercial airliners, such observations can be routinely performed. This thesis presents investigations into CO<sub>2</sub> and CH<sub>4</sub> measurements aboard commercial airliners, and potential applications for carbon cycle studies within the In-service Aircraft for a Global Observing System (IAGOS) project.

The design of a high-accuracy continuous CO<sub>2</sub>/CH<sub>4</sub>/H<sub>2</sub>O analyzer suitable for use aboard commercial airliners has been accomplished based on improvements of a commercially available instrument using the cavity ring-down spectroscopy (CRDS) technique. Since water vapor modifies the mixing ratio of CO<sub>2</sub>/CH<sub>4</sub> in wet air, efforts have been made to employ the water vapor mixing ratio simultaneously measured by the CRDS analyzer to derive the mixing ratio of CO<sub>2</sub>/CH<sub>4</sub> in dry air. Quadratic water correction functions that are sufficient for correcting the dilution and the pressure-broadening effects caused by the water vapor were established based on laboratory experiments. Furthermore, these water corrections were found to be transferable from one instrument to another and stable over time. These achievements eliminate the necessity of drying the air to obtain mixing ratios in dry air and contribute to the expertise of atmospheric trace gas measurements using spectroscopy techniques.

The CRDS analyzer was flown without a drying system or any in-flight calibration gases during a campaign over the Amazon rain forest in Brazil in May 2009. A comparison of CO<sub>2</sub> measurements between the CRDS analyzer and a nondispersive infrared (NDIR) analyzer on board the same aircraft showed that the CRDS analyzer was highly stable. To validate the continuous in situ CO<sub>2</sub>/CH<sub>4</sub> measurements made by the CRDS analyzer with reliable discrete CO<sub>2</sub>/CH<sub>4</sub> measurements from air samples taken with glass flasks during flight, weighting functions have been derived for both single flasks and paired flasks. These weighting functions are useful for the comparison by accounting for the

atmospheric variability of CO<sub>2</sub>/CH<sub>4</sub> during the flask sampling. Both CO<sub>2</sub> and CH<sub>4</sub> measurements showed good agreement with the flask measurements.

The high performance and low-maintenance requirement of the CRDS analyzer have made it the analyzer of choice for measurements of greenhouse gases aboard commercial aircraft. The first instrument will be deployed in 2011 and 7 aircraft are foreseen to be equipped with the CO<sub>2</sub>/CH<sub>4</sub>/H<sub>2</sub>O analyzer within the IAGOS project.

To investigate whether profiles from a commercial airliner program are regionally representative, given that these profiles are made near major cities and are potentially contaminated by local pollution, CO profiles over Frankfurt (Main) were assessed as a proxy for fossil fuel CO<sub>2</sub> components. The analyses showed that measurements in the upper half of the planetary boundary layer (PBL) are regionally representative. An underestimation of CO enhancements in the PBL was found and was attributed to the underestimation of fossil fuel emissions in the inventory.

Spatial representation errors and total uncertainties in fossil fuel CO<sub>2</sub> from Frankfurt and in both fossil fuel and biospheric CO<sub>2</sub> from a reference site, Bialystok, are estimated. Both spatial representation errors and total uncertainties in fossil fuel CO<sub>2</sub> from Frankfurt are significantly larger than those in fossil fuel CO<sub>2</sub> from Bialystok, but are smaller than the total uncertainty of biospheric CO<sub>2</sub> from Bialystok when observations from the upper half of the PBL in summertime are considered. These suggest that the upper half of the PBL over Frankfurt can be useful for carbon cycle studies to constrain biospheric fluxes. To deal with the unresolved variability of fossil fuel CO<sub>2</sub> from a commercial airliner program, a joint CO<sub>2</sub>-CO inversion is suggested. With the additional information about the fossil fuel emissions provided by CO observations, such a joint inversion is expected to be able to optimize both anthropogenic and biospheric CO<sub>2</sub> fluxes simultaneously.

## Kurzfassung

Atmosphärische Messungen von Kohlendioxid ( $\text{CO}_2$ ), Methan ( $\text{CH}_4$ ) und Wasserdampf ( $\text{H}_2\text{O}$ ) liefern wichtige Erkenntnisse zum Verständnis des globalen Kohlenstoffkreislaufes und zum Beitrag dieser Treibhausgase zum Klimawandel. Dabei spielen flugzeuggestützte Messungen eine wichtige Rolle, da sie zur Verbesserung atmosphärischer Transportmodelle und zur Validierung von Fernerkundungsdaten verwendet werden können. An Bord von Linienflugzeugen können solche Messungen routinemäßig durchgeführt werden. In dieser Arbeit wurden im Rahmen des Projekts IAGOS (In-service Aircraft for a Global Observing System)  $\text{CO}_2$ - und  $\text{CH}_4$ -Messungen an Bord von Linienflugzeugen und deren potentielle Anwendungen für Studien des Kohlenstoffkreislaufes untersucht.

Zunächst wurde das Design eines Messgeräts für hochpräzise, kontinuierliche Messungen von  $\text{CO}_2$ ,  $\text{CH}_4$  und  $\text{H}_2\text{O}$  an Bord von Linienflugzeugen entwickelt, basierend auf einem kommerziellen Gerät, welches die Methode der Cavity-Ringdown-Spektroskopie (CRDS) als Messprinzip verwendet. Da der Wasserdampf, der in feuchter Luft enthalten ist, die  $\text{CO}_2$ - und  $\text{CH}_4$ -Konzentration beeinflusst, wurde die gleichzeitige  $\text{H}_2\text{O}$ -Messung des CRDS-Geräts dazu verwendet, um die entsprechende  $\text{CO}_2$ - bzw  $\text{CH}_4$ -Konzentration in trockener Luft zu berechnen. Dazu wurden auf der Basis von Laborexperimenten quadratische Korrekturfunktionen entwickelt, mit denen sowohl Verdünnungs- als auch Druckverbreiterungseffekte, die durch den Wasserdampf hervorgerufen werden, korrigiert werden können. Diese Funktionen können auch auf andere Geräte desselben Typs übertragen werden und erwiesen sich als zeitlich stabil. Damit wird eine Trocknung des Probengases überflüssig, was den Wartungsaufwand des Gerätes signifikant reduziert. Zudem stellt die Verwendung der Korrekturfunktionen einen wesentlichen Beitrag zur Verbesserung der Messung von Spurengasen mit spektroskopischen Techniken dar.

Das CRDS-Messgerät wurde im Mai 2009 im Rahmen einer Flugkampagne über dem brasilianischen Regenwald getestet, wobei während der Flüge weder Kalibriergase noch ein Trocknungssystem für die Probenluft verwendet wurden. Vergleiche der  $\text{CO}_2$ -

Messungen des CRDS-Geräts mit einem NDIR-Messgerät (NDIR = nicht-dispersives Infrarot) an Bord desselben Flugzeugs zeigten gute Übereinstimmung und Stabilität der Messwerte im Rahmen der Messgenauigkeit. Um die kontinuierlichen CO<sub>2</sub>- und CH<sub>4</sub>-Messungen des CRDS-Geräts zusätzlich durch CO<sub>2</sub>/CH<sub>4</sub>-Messungen aus Luftproben zu validieren, die während des Fluges in 1l-Glasbehältern (sogenannten Flasks) genommen wurden, wurden Wichtungsfunktionen entwickelt. Diese Wichtung der in-situ Daten ist nötig, um die atmosphärische Variabilität während der Flask-Befüllung zu berücksichtigen. Wichtungsfunktionen wurden sowohl für die Probennahme einzelner Flasks als auch von Flaskpaaren berechnet. Sowohl für die CO<sub>2</sub>- als auch die CH<sub>4</sub>-Daten ergibt sich eine gute Übereinstimmung zwischen den gewichteten in-situ Messungen und den Ergebnissen der Flaskanalyse.

Aufgrund seiner guten Leistungsfähigkeit und seines niedrigen Wartungsbedarfs wurde das CRDS-Gerät für den Einsatz an Bord von Linienflugzeugen ausgewählt. Das erste Gerät soll bereits 2011 eingesetzt werden, insgesamt sollen im Rahmen des IAGOS-Projekts sieben Flugzeuge mit diesem CO<sub>2</sub>/CH<sub>4</sub>/H<sub>2</sub>O-Messgerät ausgestattet werden.

Profilmessungen, die an Bord von Linienflugzeugen durchgeführt werden, stammen oft aus der Nähe von größeren Städten und sind daher möglicherweise durch lokale Luftverschmutzung kontaminiert. Um zu überprüfen, ob diese Profile dennoch regional repräsentativ sein können, wurden CO-Profilmessungen über Frankfurt (Main) untersucht, wobei CO als Indikator für fossile CO<sub>2</sub>-Signale verwendet wurde. Die Analysen zeigen, dass Messdaten aus der oberen Hälfte der planetaren Grenzschicht (planetary boundary layer, PBL), durchaus repräsentativ für die gesamte Region sind. Zudem wurde nachgewiesen, dass die Modellrechnungen die CO-Erhöhung innerhalb der PBL unterschätzen, was mit der Unterschätzung fossiler Emissionen in den verwendeten Datenbanken zu erklären ist.

Räumliche Repräsentationsfehler und Unsicherheiten in der fossilen CO<sub>2</sub>-Komponente wurden abgeschätzt, sowohl für die Frankfurt-Profile als auch Profilmessungen einer abgelegenen Referenzstation, Bialystok (Polen). Für Bialystok wurden diese



Abschätzungen zusätzlich für die biosphärische CO<sub>2</sub>-Komponente vorgenommen. Sowohl die Repräsentationsfehler als auch die Unsicherheiten in der fossilen CO<sub>2</sub>-Komponente sind in Frankfurt größer als in Bialystok, aber kleiner als die Unsicherheit der biosphärischen CO<sub>2</sub>-Komponente der Bialystok-Messungen, wenn Messungen aus dem oberen Teil der PBL im Sommer berücksichtigt werden. Dies suggeriert, dass der obere Teil der PBL über Frankfurt nützlich für Studien des Kohlenstoffkreislaufs sein kann, um biosphärische Flussabschätzungen einzugrenzen. Um mit dem ungeklärten Anteil der fossilen CO<sub>2</sub>-Variabilität umzugehen, wird eine gekoppelte CO<sub>2</sub>-CO-Inversion vorgeschlagen. Mit der zusätzlichen Information über fossile Emissionen, die man aus den CO-Messungen erhält, kann eine solche gekoppelte Inversion dazu verwendet werden, um gleichzeitig anthropogene und biosphärische CO<sub>2</sub>-Flüsse zu optimieren.

## List of abbreviations and acronyms

AREP	– Atmospheric Research and Environmental Programme
BARCA	– Balanço Atmosférico Regional de Carbono na Amazônia
CARIBIC	– Civil Aircraft for the Regular Investigation of the atmosphere Based on an Instrument Container
CEAS	– Cavity Enhanced Absorption Spectroscopy
CONTRAIL	– Comprehensive Observation Network for TRace gases by AIRLiner
CRDS	– Cavity Ring-Down Spectroscopy
ECMWF	– European Center for Medium-Range Weather Forecasts
ENSO	– El Niño/Southern Oscillation
FTS	– Fourier Transform Spectroscopy
GASP	– Global Atmospheric Sampling Project
GAW	– Global Atmosphere Watch
GC	– Gas Chromatograph
GOSAT	– Greenhouse gases Observing SATellite
GWP	– Global Warming Potential
HITRAN	– HIgh resolution TRANsmission
IAGOS	– In-service Aircraft for a Global Observing System
–DS	– Design Study
–ERI	– European Research Infrastructure
ICOS	– Integrated Cavity Output Spectroscopy
IER	– Institute of Economics and the Rational use of energy
IPCC	– Intergovernmental Panel of Climate Change
JAL	– Japan Airlines
MOZAIC	– Measurements of OZone and water vapor by AIRbus in-service airCRAFT
MPI-BGC	– Max-Planck Institute for BioGeoChemistry (Germany)
WMO	– World Meteorological Organization
NASA	– National Aeronautics and Space Administration
NDIR	– Non-Dispersive InfraRed

NEE	– Net Ecosystem Exchange
NMHC	– Non-Methane HydroCarbons
OD	– Optical Density
OVOC	– Oxygenated Volatile Organic Compounds
PBL	– Planetary Boundary Layer
PTR-MS	– Proton Transfer Reaction Mass Spectrometer
QCL	– Quantum Cascade Laser
RDT	– Ring-Down Time
STILT	– Stochastic Time Inverted Lagrangian Transport
UT/LS	– Upper Troposphere/Lower Stratosphere
VAI	– Volcanic Aerosol Index
VOC	– Volatile Organic Carbons
VPDB	– Vienna Pee Dee Belemnite
VPRM	– Vegetation Photosynthesis and Respiration Model
VSMOW	–Vienna Standard Mean Ocean Water
WDCGG	– World Data Center for Greenhouse Gases
NOAA	– National Oceanic & Atmospheric Administration (USA)
–ESRL	– Earth System Research Laboratory

# Chapter 1 Introduction

## 1.1 Background

### 1.1.1 Greenhouse gases

The major greenhouse gases in the Earth's atmosphere are water vapor ( $\text{H}_2\text{O}$ ), carbon dioxide ( $\text{CO}_2$ ), methane ( $\text{CH}_4$ ), nitrous oxide ( $\text{N}_2\text{O}$ ), tropospheric ozone ( $\text{O}_3$ ), and chlorofluorocarbons (CFCs). They are able to absorb long wave radiation emitted from the Earth's surface, which results in a so-called greenhouse effect that keeps the Earth's and atmosphere warm. Without the greenhouse effect, the Earth's surface temperature would be on average about 33 °C colder than the present average temperature of 15 °C. Human activities have disturbed most of these major greenhouse gases (except water vapor), causing increases of their concentrations in the atmosphere. This thesis focuses on measurements and analyses of the two most important anthropogenic greenhouse gases, atmospheric  $\text{CO}_2$  and  $\text{CH}_4$ . The physics of the greenhouse effect was already described by a Swedish scientist, Svante Arrhenius, in 1896; further, global warming was, for the first time, predicted (Arrhenius 1896).

#### 1.1.1.1 Carbon Dioxide

Carbon Dioxide ( $\text{CO}_2$ ) is the most abundant anthropogenic greenhouse gas, which accounts for about 0.038%, i.e. 380 parts per million (ppm) of the atmosphere. Accurate continuous measurements of atmospheric  $\text{CO}_2$  concentrations have been made since 1958 at Mauna Loa Observatory (Pales et al., 1965). Fig.1.1 shows the longest record of  $\text{CO}_2$  concentrations at this monitoring site (not shown for the period 1958-1973). This curve clearly shows that  $\text{CO}_2$  concentrations have been increasing. Besides this, seasonal variations in the  $\text{CO}_2$  signal can also be observed. The rise of  $\text{CO}_2$  in the atmosphere is believed to be the main cause of ongoing global warming (IPCC, 2007). As the most

important anthropogenic greenhouse gas, CO<sub>2</sub> is of central interest to climate change studies.

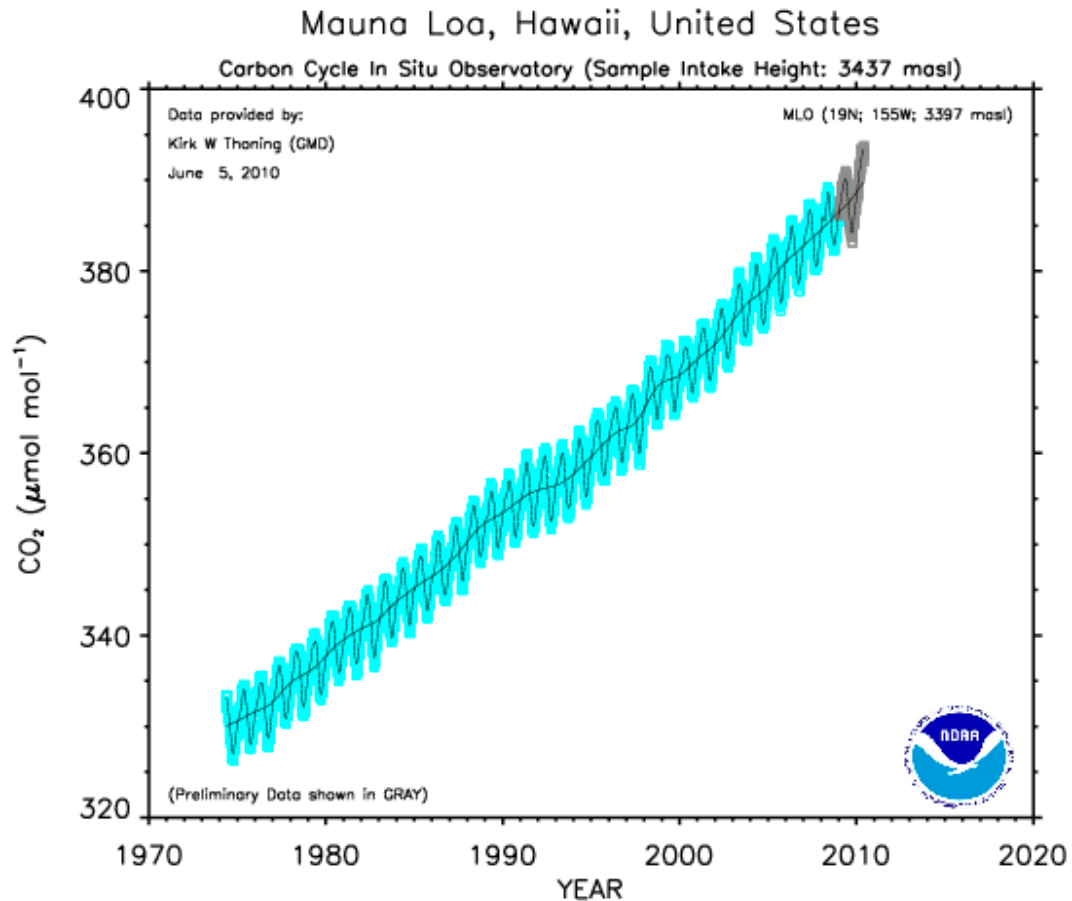


Figure 1.1 Atmospheric CO<sub>2</sub> observations at Mauna Loa for the period of 1974 – 2010, from <http://www.esrl.noaa.gov/gmd/ccgg/iadv/>

#### 1.1.1.2 Methane

Methane (CH<sub>4</sub>) is the second most important anthropogenic greenhouse gas. Its abundance in the atmosphere has increased from the pre-industrial level of 700 parts per billion (ppb) to approximately 1750 ppb in 2009. The observation record of CH<sub>4</sub> at Mauna Loa is shown in Fig. 1.2. The CH<sub>4</sub> growth rate since the early 1900s has decreased significantly and is close to zero for the six-year period from 1999 to 2005; however, the reason for the slowing down of the CH<sub>4</sub> growth rate is still uncertain.

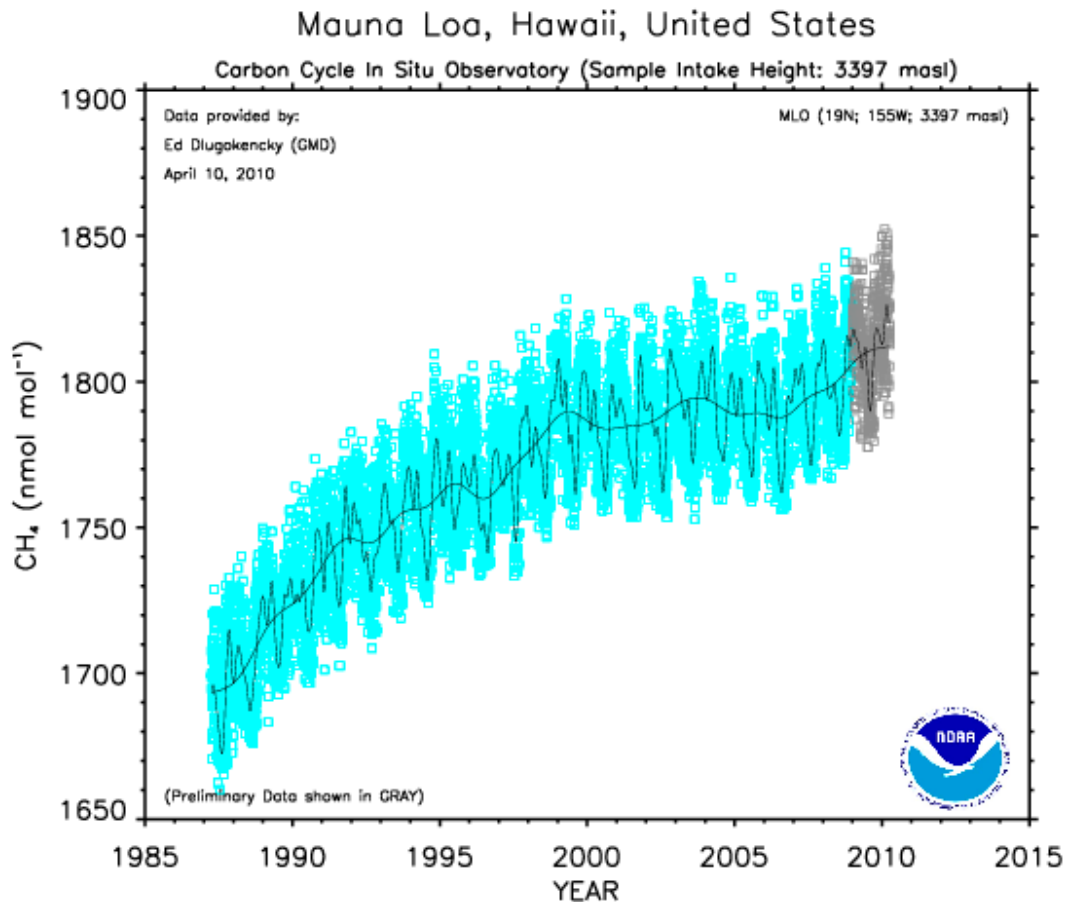


Figure 1.2 Atmospheric CH<sub>4</sub> observations at Mauna Loa for the period of 1987 – 2010, from <http://www.esrl.noaa.gov/gmd/ccgg/iadv/>

### 1.1.2 The carbon cycle

The carbon cycle describes the exchange of carbon between different major reservoirs, which are the atmosphere, the hydrosphere, the terrestrial biosphere, and the lithosphere. In the carbon cycle, the atmosphere is of central interest because it is an important active reservoir and interacts directly with all other major reservoirs. In the atmosphere, carbon is present mainly as CO<sub>2</sub>, with minor amounts present as CH<sub>4</sub>, CO, NMHC (non-methane hydrocarbons) and other minor gases. Both CO<sub>2</sub> and CH<sub>4</sub> play important roles in the natural cycle of carbon. Carbon is taken up from atmosphere by terrestrial plants through photosynthesis and is returned to the atmosphere as CO<sub>2</sub> through respiration or as CH<sub>4</sub> under anaerobic conditions by plant, soil and animal respiration. Besides this, carbon is also continuously exchanged between the atmosphere and the ocean. The lithosphere is a large reservoir of carbon; however, the flux due to the weathering process is very small.

The magnitudes of carbon storage in the major reservoirs as well as annual fluxes between reservoirs are shown in Fig. 1.3, including both the pre-industrial natural process (in black) and perturbations from human activities (in blue).

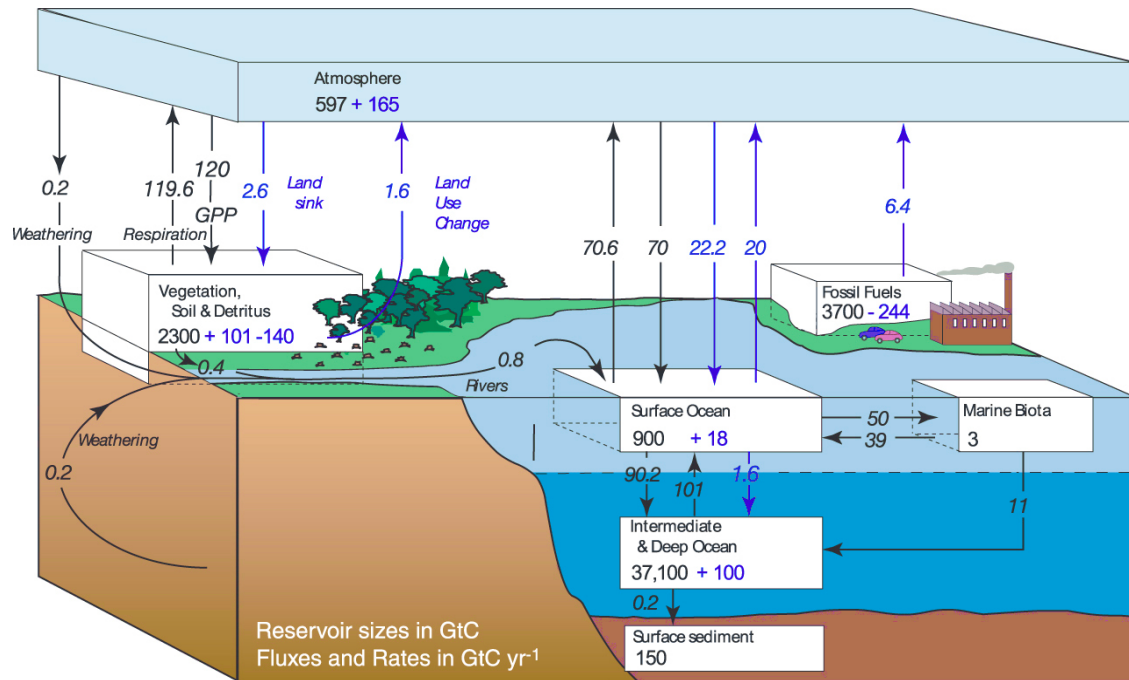
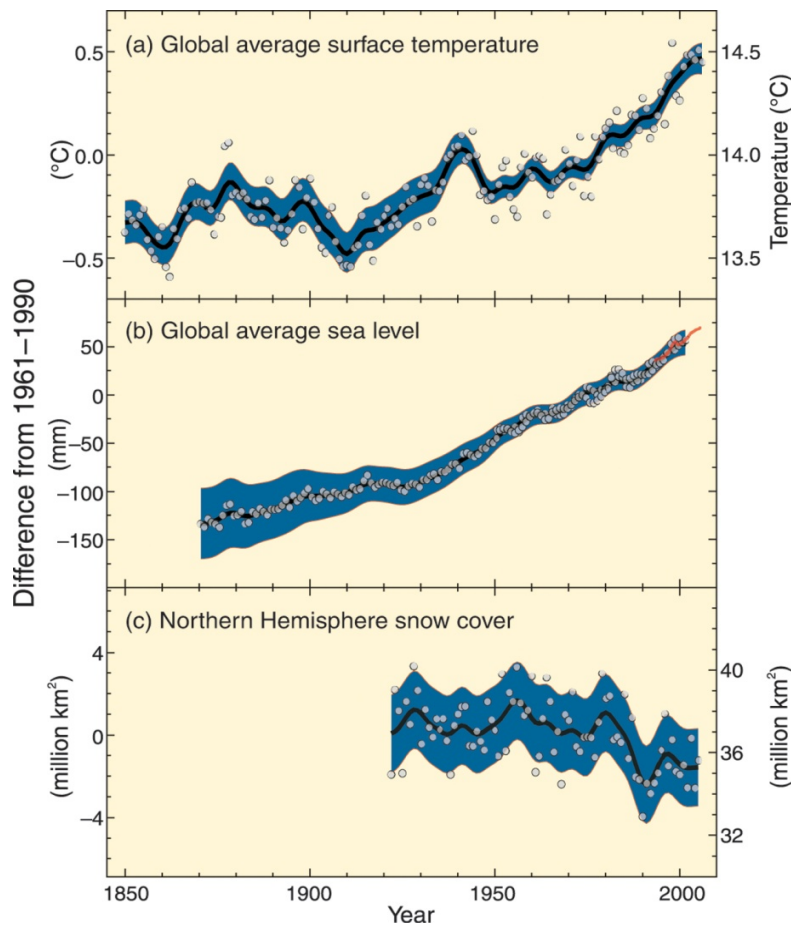


Figure 1.3 The global carbon cycle for the 1990s, showing the main annual fluxes in GtC yr<sup>-1</sup>: pre-industrial ‘natural’ fluxes in black and ‘anthropogenic’ fluxes in blue. Gross fluxes generally have uncertainties of more than 20%. Atmospheric carbon content and all cumulative fluxes since 1750 are as of the end of 1994 (from IPCC AR4).

Atmospheric CO<sub>2</sub> has increased from the preindustrial level of around 280 ppm (Siegenthaler et al., 2005) to the present value of more than 380 ppm (GLOBALVIEW-CO<sub>2</sub> 2009) and CH<sub>4</sub> has increased from about 700 ppb (Spahni et al., 2005) to the present value of more than 1700 ppb (GLOBALVIEW-CH<sub>4</sub> 2009) for the same period, which are levels that the earth has not experienced for at least 650 thousand years according to ice core studies (Petit et al., 1999; Siegenthaler et al., 2005; Spahni et al., 2005). The increase of CO<sub>2</sub> and CH<sub>4</sub> was evidently caused by human activities, mainly through fossil fuel emissions (Andres et al., 1996) and land use change (Andreae et al., 2001; Houghton 2003).

### 1.1.3 Climate change

In the Intergovernmental Panel on Climate Change (IPCC) report, climate change refers to “a change in the state of the climate that can be identified (e.g. using statistical tests) by changes in the mean and/or the variability of its properties, and that persists for an extended period, typically decades or longer.” With respect to the property of temperature, climate warming has been directly and indirectly observed from the increase of the global mean temperature, snow melting and global average sea level rise (see Fig.1.4).



*Figure 1.4 Observed changes in (a) global average surface temperature; (b) global average sea level from tide gauge (blue) and satellite (red) data; and (c) Northern Hemisphere snow cover for March-April. All differences are relative to corresponding averages for the period 1961-1990. Smoothed curves represent decadal averaged values while circles show yearly values. The shaded areas are the uncertainty intervals estimated from a comprehensive analysis of known uncertainties (from IPCC AR4).*



A summary of different radiative forcings based on 2005 emissions and relative changes since 1750 reveals (Forster et al., 2007) reveals that climate warming is caused mainly by the increase in anthropogenic greenhouse gas concentrations, with minor contribution from changes in solar irradiance. There are several components with negative radiative forcings, such as aerosols, stratospheric ozone and surface albedo changes due to land use; however, these forcings are overwhelmed by the radiative forcings due to increases of greenhouse gases (CO<sub>2</sub>, CH<sub>4</sub> and N<sub>2</sub>O). Note that different greenhouse gases are not equally effective in causing global warming because they have different radiative efficiencies and different lifetimes. CO<sub>2</sub> and CH<sub>4</sub> are long-lived greenhouse gases in the atmosphere. CH<sub>4</sub> has a lifetime of  $8.7 \pm 1.3$  years (Stevenson et al., 2006), while CO<sub>2</sub> does not have a specific lifetime but a lifetime range from a few to more than a hundred years (Forster et al., 2007). Taking these factors into account, the Global Warming Potential (GWP) can estimate how much one greenhouse gas contributes to global warming relative to that of the same mass of CO<sub>2</sub>. For example, CH<sub>4</sub> and N<sub>2</sub>O have GWP values of 25 and 298 for time horizons of 100 years, respectively.

#### **1.1.4 Understanding the sources and sinks**

In previous sections, it was clarified that the long-term atmospheric CO<sub>2</sub> increase since the pre-industrial era is caused by human activities, mainly through fossil fuel emissions and land use change; however, only a fraction of these anthropogenic emissions stayed in the atmosphere, while the rest were absorbed by the land and the oceans. The fraction of total emissions accumulating in the atmosphere (the so-called airborne fraction) was estimated to have an average value of 43% and a proportional growth rate of  $0.25 \pm 0.21$  % y<sup>-1</sup> over the period 1959 – 2008 (Canadell et al., 2007; Raupach et al., 2008; Le Quere et al., 2009). Understanding how the airborne fraction changes over time is a key point since this may provide information on the climate sensitivity of ecosystems and oceans. However, the increase of the airborne fraction was found out to be insignificant by Knorr (2009) when the El Niño/Southern Oscillation (ENSO) and the global Volcanic Aerosol Index (VAI) were not included in the trend estimate. On one hand, the existence of the airborne fraction means that the land and the oceans are currently removing CO<sub>2</sub> from the atmosphere and therefore have a negative feedback on the carbon-climate system. On the

other hand, the increase of the airborne fraction implies that the feedback is weakening, which of course depends on whether the increase is significant or not. There are a number of less well-understood mechanisms that tend to diminish the negative feedback (Field et al., 2007). Above all, understanding the sources and sinks of atmospheric CO<sub>2</sub> is indispensable for understanding the mechanisms of the feedback and further predicting the sensitivity of the climate feedback.

An effort to partition the sinks and sources of carbon on the global scale demonstrates that the main carbon sources are fossil fuel combustion and land use change, while the dominant sinks are the ecosystem and the oceans, with the rest staying in the atmosphere (Le Quere et al., 2009). The estimations for the sources and sinks for the period 2000 – 2008 are illustrated in Fig.1.5, showing that 45% remains in the atmosphere, 29% is absorbed by the ecosystem and 26% is absorbed by the oceans. Note that there is a residual of about 0.3 Pg C in this study. There are uncertainties in these estimates, for example, in 2008, fossil fuel emissions account for  $8.7 \pm 0.5$  Pg C, land use change is  $1.2 \pm 0.7$  Pg C, while the land takes up  $4.7 \pm 1.2$  Pg C, Oceans takes up  $2.3 \pm 0.4$  Pg C yr<sup>-1</sup> and  $3.9 \pm 0.1$  Pg C remains in the atmosphere (Le Quere et al., 2009).

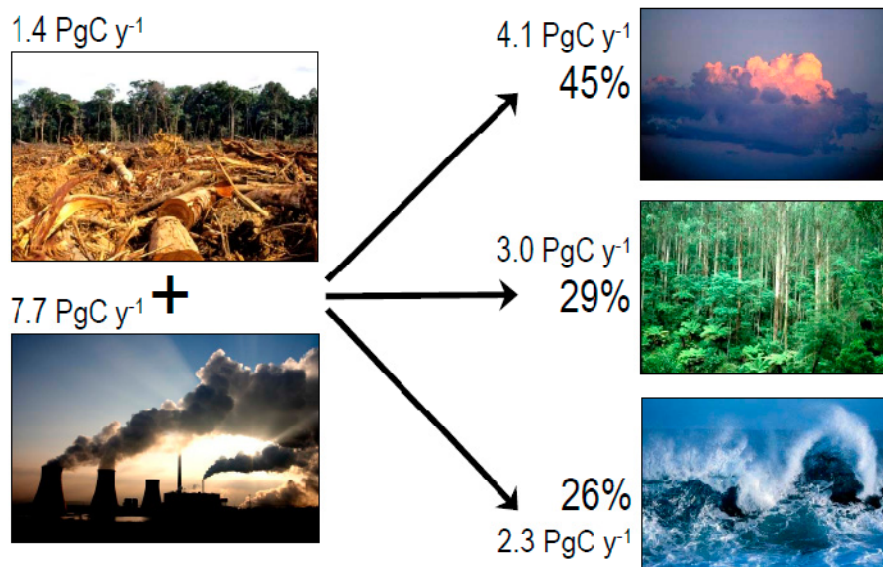


Figure 1.5. Sources and sinks of CO<sub>2</sub> for the period 2000 – 2008, from the global carbon budget project at <http://www.globalcarbonproject.org/carbonbudget/>; note that there is a residual of 0.3 PgC y<sup>-1</sup> between the total sources and sinks.

## 1.2 Atmospheric CO<sub>2</sub> and CH<sub>4</sub> monitoring

Due to their atmospheric lifetime, both CO<sub>2</sub> and CH<sub>4</sub> are relatively well mixed in the atmosphere but continuously perturbed by natural and anthropogenic fluxes. Both fossil fuel burning and land use change release carbon to the atmosphere directly/indirectly with spatial and temporal variations. As described in Chapter 1.1.4, some of the emissions will be absorbed by the oceans and some by the biosphere. Atmospheric concentrations of CO<sub>2</sub> and CH<sub>4</sub> capture the spatial and temporal pattern of carbon sources and sinks, and thus can be used to infer the carbon sources and sinks. Measurements of CO<sub>2</sub> concentrations play an important role in understanding the global carbon cycle and its contribution to global warming (Bischof 1962; Keeling et al., 1968; Tans et al., 1996; Heimann 2009).

### 1.2.1 Observational platforms

Atmospheric monitoring of CO<sub>2</sub> and CH<sub>4</sub> have been made on a variety of observational platforms, such as ground-based stations, towers, aircraft, ships, high altitude balloons and satellites (illustrated in Fig. 1.6).



*Figure 1.6. Observational platforms for measurements of CO<sub>2</sub> and CH<sub>4</sub> concentrations*

The spatial and temporal coverage as well as the primary advantages and disadvantages of using these observational platforms for measurements of CO<sub>2</sub> and CH<sub>4</sub> concentrations in the atmosphere are summarized in Table 1. These observations are normally made in rural monitoring sites to avoid the influence of nearby anthropogenic emissions so that point measurements can represent larger scales. Tall towers (> 200 m height) can be used to sample air from different heights and obtain a vertical profile of trace gases. The observations at high levels, for example 300 m, provide information on the mixed layer during daytime and often the residual layer during nighttime, while observations at the lower levels might be influenced by processes at the surface. Long term records of these observations are becoming more useful for trend analyses since short-term variability can be easily distinguished.

*Table 1. Comparison of observational platforms for measurements of CO<sub>2</sub> and CH<sub>4</sub> concentrations in the atmosphere*

<b>Platforms Types</b>	<b>Stations</b>	<b>Ships</b>	<b>Towers</b>	<b>Aircraft</b>	<b>Balloons</b>	<b>Satellites</b>
<b>Horizontal coverage</b>	Points	Routes	Points	Regional to continental	Points	global
<b>Vertical coverage</b>	Several meters	Several meters	Up to several hundred meters	Up to 20 km	Up to 30 km ~ 40 km	Total column
<b>Temporal</b>	Decades	Decades	Decades	Hours	Hours	Years

Since observations on mobile platforms provide information about large scales and three-dimensional distributions, they are essential observing methods for understanding the global carbon cycle. In January 2009, the Greenhouse gases Observing SATellite (GOSAT) was successfully launched as the first satellite dedicated to carbon cycle science. GOSAT measures total column mean CO<sub>2</sub> and CH<sub>4</sub> concentrations and provides information about global distributions of CO<sub>2</sub> and CH<sub>4</sub>. The information from GOSAT will also help determine the geographical distributions of fluxes of CO<sub>2</sub> and CH<sub>4</sub> that are of central interest for studying climate-ecosystem feedbacks. Note that column mean CO<sub>2</sub> and CH<sub>4</sub> concentrations can be obtained from other ground-based remote sensing techniques, e.g. Fourier Transform Spectroscopy (FTS). Both observations from GOSAT

and FTS measurements need to be validated so that the measurements are linked to the WMO scales for CO<sub>2</sub> and CH<sub>4</sub>.

Aircraft measurements are a key method for monitoring CO<sub>2</sub> and CH<sub>4</sub> concentrations in the atmosphere. First, aircraft measurements provide vertical profiles from the ground level up to 20 km, covering the whole free troposphere and lower stratosphere, while the tall towers can only acquire profiles of trace gases up to a few hundred meters. Second, aircraft measurements, together with balloon measurements, provide a unique way to validate observations from remote sensing techniques, such as satellite and FTS. Last but not least, the profiles of trace gases contain information on actual vertical mixing and can be used to improve the vertical mixing for transport models. The vertical gradients are not well represented by transport models, and the misrepresentation of the vertical gradients by the models tends to bias the estimations of carbon fluxes (Stephens et al., 2007).

Regional scale CO<sub>2</sub> fluxes have been investigated by aircraft campaigns over North America by the CO<sub>2</sub> Budget and Rectification Airborne (COBRA) study (Gerbig et al, 2003) as well as over Southern West France by the CarboEurope Regional Experiment Strategy (CERES) (Sarrat et al, 2007). However these campaign-based aircraft measurements are predominantly to provide intensive regional CO<sub>2</sub> information for a specific region over a short period, and as such are not able to provide long-term variations of the atmosphere. Besides the other advantages in using aircraft for obtaining vertical profiles, use of commercial airliners complements campaign-based aircraft observations by providing routine and intercontinental observations that will greatly strengthen the observational network.

### **1.2.2 Observational networks**

The Global Atmosphere Watch (GAW) program of the World Meteorological Organization (WMO) is coordinated by the Atmospheric Research and Environmental Programme (AREP) under guidance from the Commission for Atmospheric Sciences

(CAS). The GAW project coordinates activities to achieve the global monitoring of atmospheric composition with “the need to understand and control the increasing influence of human activity on the global atmosphere.” One of the most important focuses of the GAW project is the global network for greenhouse gases that addresses the issue of climate change. Major anthropogenic greenhouse gases ( $\text{CO}_2$ ,  $\text{CH}_4$ , tropospheric  $\text{O}_3$ , CFCs,  $\text{N}_2\text{O}$ ) and related trace gases ( $\text{CO}$ ,  $\text{NO}_x$ ,  $\text{SO}_2$ , VOC etc.) are monitored in the global network. The monitoring locations of the global network are shown in Fig. 1.7, including locations of ground-based stations and routes of aircraft and ships. The three stations labeled by crosses are comparison sites for greenhouse gases with the purpose of ensuring inter-laboratory comparability. To link the observations across the globe, central calibration laboratories have been established for different species. These laboratories are responsible for maintaining WMO reference standards and providing references to other institutions. The observation data from this network are collected and archived in the World Data Center for Greenhouse Gases (WDCGG) at the Japan Meteorological Agency.

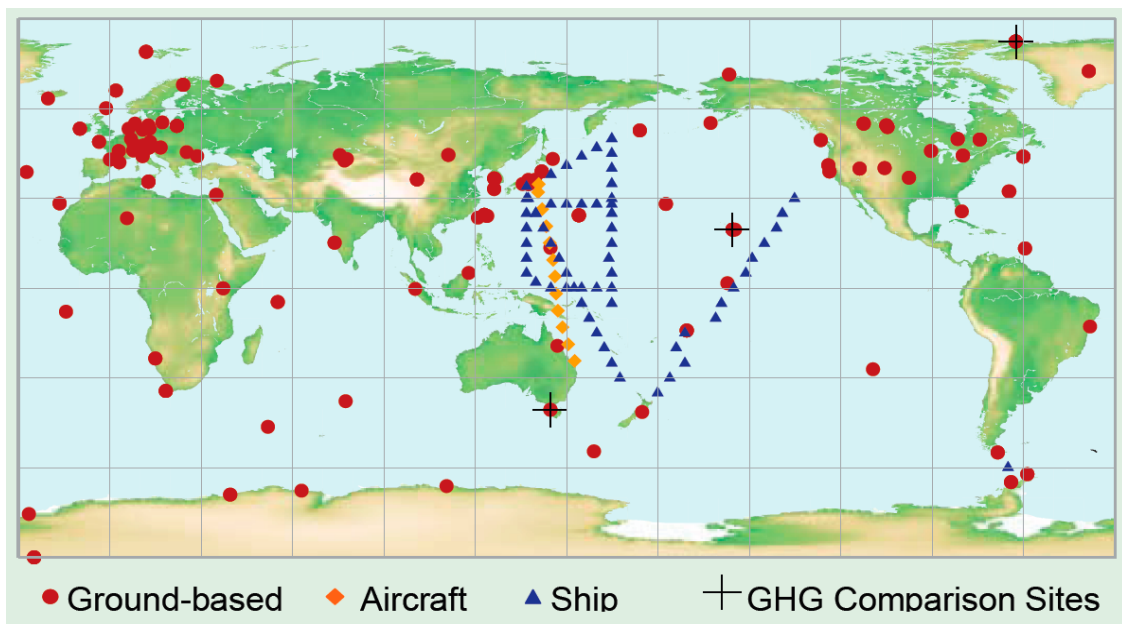


Fig. 1.7. The WMO-GAW global observation network for  $\text{CO}_2$ . The network for  $\text{CH}_4$  is similar to this (from WMO Greenhouse Gas Bulletin No. 5, November 2009)

These atmospheric observations have been used to infer the sources and sinks of carbon in inverse studies (Rayner et al., 1999; Peylin et al., 2002; Roedenbeck et al., 2003; Peters et al., 2007). However, these observations are not adequate to constrain regional carbon fluxes since they are still quite sparse (Gurney et al., 2002). There is a strong need for expansion of the measurement network. Also note that most observations in the WMO-GAW network are ground based and adding aircraft observations into this network is particularly important.

### **1.3 The commercial airliner programs**

#### **1.3.1 Overview of existing/past programs**

Using commercial airliners as a measurement platform, one can obtain worldwide observations for the upper troposphere/lower stratosphere region (UT/LS) with aircraft cruising at an altitude of 9 to 12 km, and large numbers of profiles during takeoff and landing. The advantage is that these observations could be routinely performed even under relatively bad weather conditions. Meanwhile, using commercial airliners is also cost effective. On the other hand, there is a major restriction for using commercial airliners: the flight routes are fixed, and only choosing aircraft from different routes or different airlines enable observations in areas of interest. The idea of using commercial airliners was already employed by Walter Bischof to collect air samples for CO<sub>2</sub> concentration measurements in 1962 (Bischof 1970). In the 1970s, measurements of trace gases, such as CO and O<sub>3</sub>, were performed using Boeing aircraft within the Global Atmospheric Sampling Project (GASP) project of National Aeronautics and Space Administration (NASA) (Falconer et al., 1976; Pratt et al., 1979). In the 1990s, several major projects started to use commercial airliners for measurements of atmospheric trace gases in Europe and in Japan. These projects are summarized in Table 2, with related characteristics shown in different columns. The general descriptions of these projects are given below.

Table 2. Routine aircraft measurement projects using commercial airliners since 1990s

Project	Period	Consortium	Aircraft type	CO <sub>2</sub> , CH <sub>4</sub> and related tracers	Frequency
MOZAIC	1993 -2007	Europe	Airbus A340	In situ CO	5 aircraft, > 25,000 flights since 1994
CARIBIC	1997 -	Europe	Boeing 767-300 ER; Airbus A340-600	In situ CO <sub>2</sub> , CO, O <sub>2</sub> ; Flask CH <sub>4</sub> , <sup>13</sup> CO <sub>2</sub> , CO <sup>18</sup> O, COS	1 aircraft, monthly since 2005
CONTRAIL	1993 -	Japan	Boeing 747-400/200ER	In situ CO <sub>2</sub> ; Flask CO <sub>2</sub> CH <sub>4</sub> , CO	5 aircraft for in situ starting from 2005; 1 aircraft for flask since 1993

#### 1.3.1.1 MOZAIC

MOZAIC (Measurements of ozone and water vapor by Airbus in-service aircraft) was initiated in January 1993 to study the influence of human activities on atmospheric species of O<sub>3</sub> and H<sub>2</sub>O. It was carried out by European scientists, Airbus Industries, and several European airlines (Lufthansa, Air France, Austrian, and Sabena) with the support of the European Commission (Marenco et al., 1998). The measurements of O<sub>3</sub> and H<sub>2</sub>O started in 1993 aboard five Airbus A340 airliners. Later in 2001, all five aircraft were successfully instrumented with a CO analyzer, and a total-odd-nitrogen (NO<sub>y</sub>) instrument was deployed on one MOZAIC aircraft operated by Lufthansa (Nedelec et al., 2003; Volz-Thomas et al., 2005). More than 25,000 flights, each including two profiles and about 8 hours of data in the UT/LS, have been collected since 1994 (see Fig. 8).





system (Ionicon, Innsbruck, Austria) has been strongly modified and deployed in the container for measuring selected oxygenated volatile organic compounds (OVOCs), such as acetone, methanol, acetaldehyde and acetonitrile (Brenninkmeijer et al., 2007). The advantage of CARIBIC is that it observes extensive species of atmospheric compositions and collects related information such as cloud conditions. On the other hand, it only flies once a month on the routes available for the specific type of aircraft and thus the coverage is limited.

### 1.3.1.3 CONTRAIL

CONTRAIL (Comprehensive Observation Network for TRace gases by AirLiner) is a Japan Airlines (JAL) project with the collaboration of several Japanese institutes. During the first phase of the JAL project from 1993 to 2005, an automatic air sampling equipment (ASE) was deployed on a Boeing 747-200 to collect air samples over the western Pacific between Australia and Japan for measurements of CO<sub>2</sub> and other trace gases (Matsueda et al., 1996). During the second phase starting from 2005, both continuous CO<sub>2</sub> measuring equipment (CME) and ASE have been deployed on Boeing aircraft. The CMEs were installed on two Boeing 747-400 and three Boeing 747-200 aircraft while the ASEs were only installed on the two Boeing 747-400 aircraft. A large number of flights with global coverage have been made during the first 15 months of the CONTRAIL project (see Fig. 9). The CONTRAIL project focuses on observations of greenhouse gases and related trace gases. During the flight of three Boeing 747-200 aircraft, only continuous CO<sub>2</sub> concentration measurements were made. The data will become more useful when other tracers such as CO are measured at the same time.

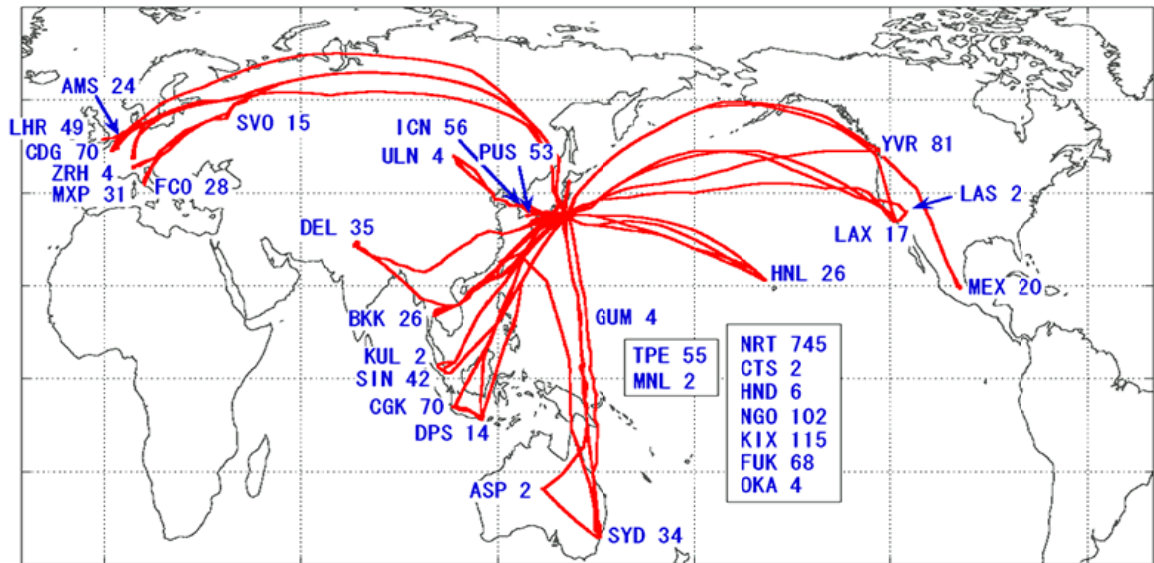


Figure 1.9 Flight route and number of successfully obtained vertical profiles during the trial observation period from November 2005 to January 2007 (figure from [http://www.jal-foundation.or.jp/shintaikikansokue/Contrail\\_index\(E\).htm](http://www.jal-foundation.or.jp/shintaikikansokue/Contrail_index(E).htm)).

### 1.3.2 The IAGOS-DS/ IAGOS-ERI project

IAGOS (In-service Aircraft for a Global Observing System) has continued the European MOZAIC project, seeking to establish a research infrastructure for global observations of atmospheric compositions initially using 10 – 20 long-range aircraft. The IAGOS project has two phases: IAGOS-DS (Design Study) and IAGOS-ERI (European Research Infrastructure). IAGOS-DS is a design study for new infrastructures. A number of instruments are being developed based on the former MOZAIC instrumentation, such as for O<sub>3</sub>, H<sub>2</sub>O, CO, and NO<sub>y</sub>/NO<sub>x</sub>. The designs for new instruments include aerosol, cloud particles and CO<sub>2</sub> analyzers. Besides instrument development, getting certifications for advanced instruments on board the Airbus A340 aircraft is also one of the tasks. The IAGOS-DS initiates the design for real time data transmission. The IAGOS-ERI establishes and operates a European infrastructure for long-term global observations of atmospheric compositions. CARIBIC has become a member of IAGOS-ERI. During this phase, the new instrument packages based on the results of the design study are certified for deployment on board Airbus A340/A320 operated by various airlines. IAGOS-ERI is expected to result in an increased fleet with more frequent flights than MOZAIC with

measurements of CO<sub>2</sub>, CH<sub>4</sub> and other trace gases. These data will be of importance for understanding the global carbon cycle and greenhouse gases related climate studies.

### 1.3.2.1 Objectives

The objective of IAGOS-DS is to explore designs for instrumentation on the basis of former MOZAIC project and prepare for establishing a European infrastructure for observations of atmospheric composition with global coverage using commercial aircraft. The project intends to increase the number of atmospheric species that are monitored, while reducing the size and weight of the instrumentation (see Fig. 1.10). New instruments for CO<sub>2</sub>, cloud, and aerosol observations are envisioned in the project. Note that the size and weight reduction is to be achieved through restrictions for all the instrumentation. Real time data transmission will also be designed. Besides the technological development, the certification and maintenance procedure will also be explored.

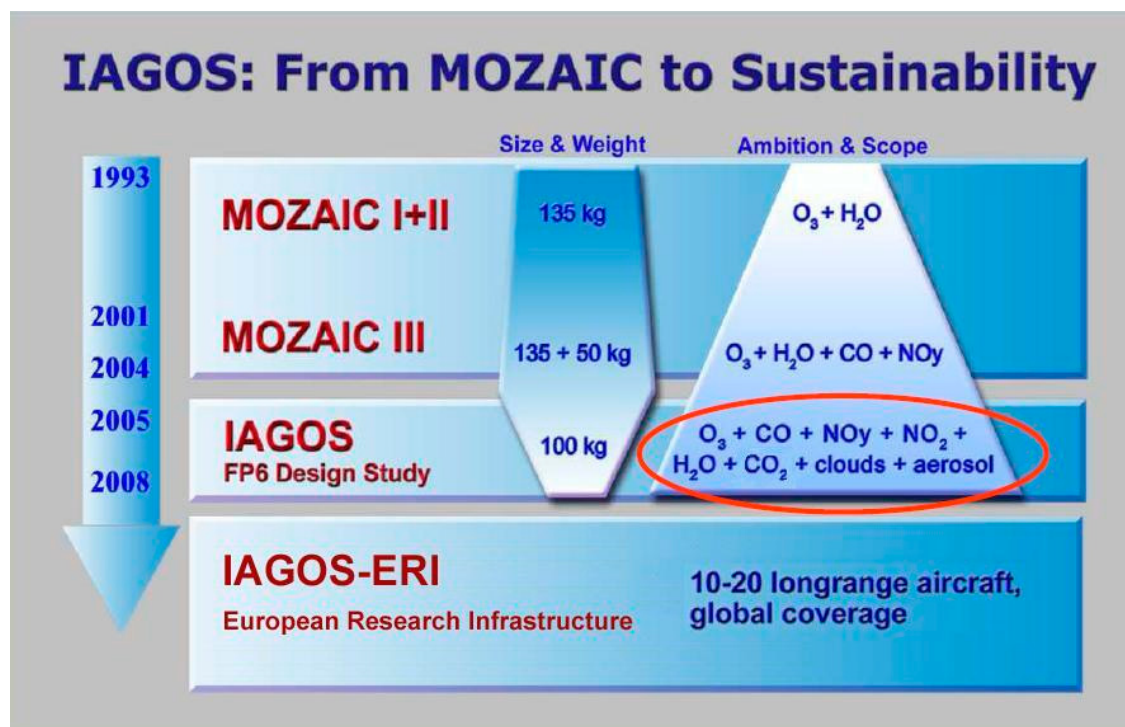


Figure 1.10 The road map of the commercial airliner program: time frame for the different EU projects, development and advancement of instrumentation with respect to size & weight, and the number of species that are monitored

### 1.3.2.2 Instrumentation

The IAGOS instrumentation consists of two instrument packages. Package I is the master package, containing the data acquisition and transmission system and instruments for measurements of O<sub>3</sub>, CO, H<sub>2</sub>O and cloud particles. Package II contains instrumentation for the monitoring of one of four species: NO<sub>y</sub>, NO<sub>x</sub>, aerosols, or CO<sub>2</sub>.

These four options for package II will have the same interfaces so that they can be replaced by each other. During the IAGOS-ERI phase, aeronautic certification of the CO<sub>2</sub> instrument will be accomplished in collaboration with Enviscope GmbH, a German company, which provides service to the scientific community for development and adaptation of instrumentation. In addition, work associated with modification and packaging is required for getting the certificate.

The design of the CO<sub>2</sub> instrument must meet the following requirements: 1) measurement precision (accuracy) to be better than 0.1 (0.2) ppm for CO<sub>2</sub>; 2) weight to be less than 30 kg; 3) size to be within 30×35×53 cm<sup>3</sup> and 4) unattended operation for 6 weeks. The precision and accuracy meet those recommended by WMO (WMO 2003). The accuracy requirement is important for use of the observations, especially for measurements at the cruise altitude (about 12 km), where variations of CO<sub>2</sub> concentrations are relatively small (Bischof 1962). The size requirement is restricted by the available space on the Airbus A340 aircraft. Since it is neither convenient nor possible in most cases to visit the aircraft for checking or maintaining the instrument, the analyzer needs to be able to operate without maintenance for at least 6 weeks, the time period between regular aircraft checks.

## 1.4 Thesis outline

This thesis focuses on the development work of a CO<sub>2</sub>/CH<sub>4</sub>/H<sub>2</sub>O analyzer for deployment on board commercial airliners within the IAGOS project; the representativeness of aircraft CO<sub>2</sub>/CO profiles from commercial airliner programs is assessed with respect to the potential use of these profiles.

Chapter 2 describes the preparation of a high-accuracy continuous greenhouse gas analyzer for deployment on board a commercial airliner. Techniques for measuring CO<sub>2</sub> and CH<sub>4</sub> are introduced and compared. Based on the availability of these techniques, investigations on two different types of analyzers, one based on the non-dispersive infrared (NDIR) technique and the other on the cavity ring-down spectroscopy (CRDS) technique, are described. Laboratory results regarding the stability and qualifications of the two analyzers for the IAGOS project are presented and discussed. Further experiments to derive water vapor corrections and assess the stability under simulated flight conditions for the CRDS analyzer are shown.

Chapter 3 presents regular aircraft measurements of in situ CO<sub>2</sub> using an NDIR analyzer near a tall tower in northeastern Poland and aircraft measurements of CO<sub>2</sub> and CH<sub>4</sub> during a BARCA (Balanço Atmosférico Regional de Carbono na Amazônia) campaign using a CRDS analyzer. For the regular flights in Poland, the in situ measurements of CO<sub>2</sub> have been validated by comparison with flask measurements of CO<sub>2</sub>. The in situ measurements were weighted with averaging kernels that have been derived from a paired-flask model. For the measurements during the BARCA campaign, the in situ measurements of CO<sub>2</sub> have been validated first by comparison with measurements of an NDIR analyzer that was flown on board the same aircraft. Furthermore, the in situ measurements of both CO<sub>2</sub> and CH<sub>4</sub> have been validated by comparison with corresponding flask measurements.

Chapter 4 assesses the representativeness of aircraft CO<sub>2</sub> profiles from the future IAGOS operation to learn how they could be used for applications such as satellite validation and inverse modeling. The goal was to determine whether IAGOS profiles from ascents and descents at airports in proximity to major metropolitan areas are to be regarded as influenced by local pollution, or if there are times during which such observations can be regarded as regionally representative. To that end, CO profiles over Frankfurt airport from the MOZAIC project have been analyzed using the Stochastic Time Inverted Lagrangian Transport (STILT) model combined with a diagnostic Vegetation Photosynthesis and Respiration Model (VPRM) and a high resolution fossil fuel emission map. CO<sub>2</sub> profiles over northeast Poland are analyzed in a similar way, in a region where

fossil fuel emissions are insignificant. Combining STILT footprints (maps of sensitivities to upstream surface fluxes) with high-resolution emission inventories allows one to attribute the contribution of fossil fuel emissions to local vs. regional sources.

Chapter 5 concludes the thesis and discusses the future work.

## 1.5 References

- Andreae, M. O. and P. Merlet (2001). "Emission of trace gases and aerosols from biomass burning." Global Biogeochemical Cycles **15**(4): 955-966.
- Andres, R. J., G. Marland, I. Fung and E. Matthews (1996). "A 1 degrees x 1 degrees distribution of carbon dioxide emissions from fossil fuel consumption and cement manufacture, 1950-1990." Global Biogeochemical Cycles **10**(3): 419-429.
- Arrhenius, S. (1896). "On the influence of carbonic acid in the air upon the temperature of the ground." Philosophical Magazine and Journal of Science **41**: 237-276.
- Bischof, W. (1962). "Variations in Concentration of Carbon Dioxide in the Free Atmosphere." Tellus **14**(1): 87-90.
- Bischof, W. (1970). "Carbon Dioxide Measurements from Aircraft." Tellus **22**(5): 545-&.
- Brenninkmeijer, C. A. M., P. Crutzen, F. Boumard, T. Dauer, B. Dix, R. Ebinghaus, D. Filippi, H. Fischer, H. Franke, U. Friess, J. Heintzenberg, F. Helleis, M. Hermann, H. H. Kock, C. Koepfel, J. Lelieveld, M. Leuenberger, B. G. Martinsson, S. Miemczyk, H. P. Moret, H. N. Nguyen, P. Nyfeler, D. Oram, D. O'Sullivan, S. Penkett, U. Platt, M. Pucek, M. Ramonet, B. Randa, M. Reichelt, T. S. Rhee, J. Rohwer, K. Rosenfeld, D. Scharffe, H. Schlager, U. Schumann, F. Slemr, D. Sprung, P. Stock, R. Thaler, F. Valentino, P. van Velthoven, A. Waibel, A. Wandel, K. Waschitschek, A. Wiedensohler, I. Xueref-Remy, A. Zahn, U. Zech and H. Ziereis (2007). "Civil Aircraft for the regular investigation of the atmosphere based on an instrumented container: The new CARIBIC system." Atmospheric Chemistry and Physics **7**(18): 4953-4976.
- Brenninkmeijer, C. A. M., P. J. Crutzen, H. Fischer, H. Gusten, W. Hans, G. Heinrich, J. Heintzenberg, M. Hermann, T. Immelmann, D. Kersting, M. Maiss, M. Nolle, A. Pitscheider, H. Pohlkamp, D. Scharffe, K. Specht and A. Wiedensohler (1999). "CARIBIC - Civil aircraft for global measurement of trace gases and aerosols in the tropopause region." Journal of Atmospheric and Oceanic Technology **16**(10): 1373-1383.

- Canadell, J. G., C. Le Quere, M. R. Raupach, C. B. Field, E. T. Buitenhuis, P. Ciais, T. J. Conway, N. P. Gillett, R. A. Houghton and G. Marland (2007). "Contributions to accelerating atmospheric CO<sub>2</sub> growth from economic activity, carbon intensity, and efficiency of natural sinks." Proceedings of the National Academy of Sciences of the United States of America **104**(47): 18866-18870.
- Falconer, P. D. and J. D. Holdeman (1976). "Measurements of Atmospheric Ozone Made from a Gasp-Equipped 747-Airliner - Mid-March, 1975." Geophysical Research Letters **3**(2): 101-104.
- Field, C. B., D. B. Lobell, H. A. Peters and N. R. Chiariello (2007). "Feedbacks of terrestrial ecosystems to climate change." Annual Review of Environment and Resources **32**: 1-29.
- Forster, P., V. Ramaswamy, P. Artaxo, T. Berntsen, R. Betts, D.W. Fahey, J. Haywood, J. Lean, D.C. Lowe, G. Myhre, J. Nganga, R. Prinn, and M. S. a. R. V. D. G. Raga (2007). "Changes in Atmospheric Constituents and in Radiative Forcing. In: Climate Change 2007: The Physical Science Basis. Contribution of Working Group I to the Fourth Assessment Report of the Intergovernmental Panel on Climate Change [Solomon, S., D. Qin, M. Manning, Z. Chen, M. Marquis, K.B. Averyt, M. Tignor and H.L. Miller (eds.)]. Cambridge University Press, Cambridge, United Kingdom and New York, NY, USA."
- GLOBALVIEW-CH<sub>4</sub> (2009). "Cooperative Atmospheric Data Integration Project - Methane. CD-ROM, NOAA ESRL, Boulder, Colorado [Also available on Internet via anonymous FTP to ftp.cmdl.noaa.gov, Path: ccg/CH<sub>4</sub>/GLOBALVIEW]."
- GLOBALVIEW-CO<sub>2</sub> (2009). "Cooperative Atmospheric Data Integration Project - Carbon Dioxide. CD-ROM, NOAA ESRL, Boulder, Colorado [Also available on Internet via anonymous FTP to ftp.cmdl.noaa.gov, Path: ccg/cO<sub>2</sub>/GLOBALVIEW]."
- Gurney, K. R., R. M. Law, A. S. Denning, P. J. Rayner, D. Baker, P. Bousquet, L. Bruhwiler, Y. H. Chen, P. Ciais, S. Fan, I. Y. Fung, M. Gloor, M. Heimann, K. Higuchi, J. John, T. Maki, S. Maksyutov, K. Masarie, P. Peylin, M. Prather, B. C. Pak, J. Randerson, J. Sarmiento, S. Taguchi, T. Takahashi and C. W. Yuen (2002). "Towards robust regional estimates of CO<sub>2</sub> sources and sinks using atmospheric transport models." Nature **415**(6872): 626-630.
- Heimann, M. (2009). "Searching out the sinks." Nature Geoscience **2**(1): 3-4.
- Houghton, R. A. (2003). "Revised estimates of the annual net flux of carbon to the atmosphere from changes in land use and land management 1850-2000." Tellus Series B-Chemical and Physical Meteorology **55**(2): 378-390.
- Keeling, C. D., T. B. Harris and E. M. Wilkins (1968). "Concentration of Atmospheric Carbon Dioxide at 500 and 700 Millibars." Journal of Geophysical Research **73**(14): 4511-&.



- Le Quere, C., M. R. Raupach, J. G. Canadell, G. Marland, L. Bopp, P. Ciais, T. J. Conway, S. C. Doney, R. A. Feely, P. Foster, P. Friedlingstein, K. Gurney, R. A. Houghton, J. I. House, C. Huntingford, P. E. Levy, M. R. Lomas, J. Majkut, N. Metzler, J. P. Ometto, G. P. Peters, I. C. Prentice, J. T. Randerson, S. W. Running, J. L. Sarmiento, U. Schuster, S. Sitch, T. Takahashi, N. Viovy, G. R. van der Werf and F. I. Woodward (2009). "Trends in the sources and sinks of carbon dioxide." Nature Geoscience **2**(12): 831-836.
- Marenco, A., V. Thouret, P. Nedelec, H. Smit, M. Helten, D. Kley, F. Karcher, P. Simon, K. Law, J. Pyle, G. Poschmann, R. Von Wrede, C. Hume and T. Cook (1998). "Measurement of ozone and water vapor by Airbus in-service aircraft: The MOZAIC airborne program, An overview." Journal of Geophysical Research-Atmospheres **103**(D19): 25631-25642.
- Matsueda, H. and H. Y. Inoue (1996). "Measurements of atmospheric CO<sub>2</sub> and CH<sub>4</sub> using a commercial airliner from 1993 to 1994." Atmospheric Environment **30**(10-11): 1647-1655.
- Nedelec, P., J. P. Cammas, V. Thouret, G. Athier, J. M. Cousin, C. Legrand, C. Abonnel, F. Lecoer, G. Cayez and C. Marizy (2003). "An improved infrared carbon monoxide analyser for routine measurements aboard commercial Airbus aircraft: technical validation and first scientific results of the MOZAIC III programme." Atmospheric Chemistry and Physics **3**: 1551-1564.
- Pales, J. C. and C. D. Keeling (1965). "Concentration of Atmospheric Carbon Dioxide in Hawaii." Journal of Geophysical Research **70**(24): 6053-&.
- Peters, W., A. R. Jacobson, C. Sweeney, A. E. Andrews, T. J. Conway, K. Masarie, J. B. Miller, L. M. P. Bruhwiler, G. Petron, A. I. Hirsch, D. E. J. Worthy, G. R. van der Werf, J. T. Randerson, P. O. Wennberg, M. C. Krol and P. P. Tans (2007). "An atmospheric perspective on North American carbon dioxide exchange: CarbonTracker." Proceedings of the National Academy of Sciences of the United States of America **104**(48): 18925-18930.
- Petit, J. R., J. Jouzel, D. Raynaud, N. I. Barkov, J. M. Barnola, I. Basile, M. Bender, J. Chappellaz, M. Davis, G. Delaygue, M. Delmotte, V. M. Kotlyakov, M. Legrand, V. Y. Lipenkov, C. Lorius, L. Pepin, C. Ritz, E. Saltzman and M. Stievenard (1999). "Climate and atmospheric history of the past 420,000 years from the Vostok ice core, Antarctica." Nature **399**(6735): 429-436.
- Peylin, P., D. Baker, J. Sarmiento, P. Ciais and P. Bousquet (2002). "Influence of transport uncertainty on annual mean and seasonal inversions of atmospheric CO<sub>2</sub> data." Journal of Geophysical Research-Atmospheres **107**(D19).
- Pratt, R. and P. Falconer (1979). "Circumpolar Measurements of Ozone, Particles, and Carbon-Monoxide from a Commercial Airliner." Journal of Geophysical Research-Oceans and Atmospheres **84**(NC12): 7876-7882.

- Raupach, M. R., J. G. Canadell and C. Le Quere (2008). "Anthropogenic and biophysical contributions to increasing atmospheric CO<sub>2</sub> growth rate and airborne fraction." Biogeosciences **5**(6): 1601-1613.
- Rayner, P. J., I. G. Enting, R. J. Francey and R. Langenfelds (1999). "Reconstructing the recent carbon cycle from atmospheric CO<sub>2</sub>, delta C-13 and O-2/N-2 observations." Tellus Series B-Chemical and Physical Meteorology **51**(2): 213-232.
- Roedenbeck, C., S. Houweling, M. Gloor and M. Heimann (2003). "CO<sub>2</sub> flux history 1982-2001 inferred from atmospheric data using a global inversion of atmospheric transport." Atmospheric Chemistry and Physics **3**: 1919-1964.
- Siegenthaler, U., T. F. Stocker, E. Monnin, D. Luthi, J. Schwander, B. Stauffer, D. Raynaud, J. M. Barnola, H. Fischer, V. Masson-Delmotte and J. Jouzel (2005). "Stable carbon cycle-climate relationship during the late Pleistocene." Science **310**(5752): 1313-1317.
- Spahni, R., J. Chappellaz, T. F. Stocker, L. Loulergue, G. Hausammann, K. Kawamura, J. Fluckiger, J. Schwander, D. Raynaud, V. Masson-Delmotte and J. Jouzel (2005). "Atmospheric methane and nitrous oxide of the late Pleistocene from Antarctic ice cores." Science **310**(5752): 1317-1321.
- Stephens, B. B., K. R. Gurney, P. P. Tans, C. Sweeney, W. Peters, L. Bruhwiler, P. Ciais, M. Ramonet, P. Bousquet, T. Nakazawa, S. Aoki, T. Machida, G. Inoue, N. Vinnichenko, J. Lloyd, A. Jordan, M. Heimann, O. Shibistova, R. L. Langenfelds, L. P. Steele, R. J. Francey and A. S. Denning (2007). "Weak northern and strong tropical land carbon uptake from vertical profiles of atmospheric CO<sub>2</sub>." Science **316**(5832): 1732-1735.
- Stevenson, D. S., F. J. Dentener, M. G. Schultz, K. Ellingsen, T. P. C. van Noije, O. Wild, G. Zeng, M. Amann, C. S. Atherton, N. Bell, D. J. Bergmann, I. Bey, T. Butler, J. Cofala, W. J. Collins, R. G. Derwent, R. M. Doherty, J. Drevet, H. J. Eskes, A. M. Fiore, M. Gauss, D. A. Hauglustaine, L. W. Horowitz, I. S. A. Isaksen, M. C. Krol, J. F. Lamarque, M. G. Lawrence, V. Montanaro, J. F. Muller, G. Pitari, M. J. Prather, J. A. Pyle, S. Rast, J. M. Rodriguez, M. G. Sanderson, N. H. Savage, D. T. Shindell, S. E. Strahan, K. Sudo and S. Szopa (2006). "Multimodel ensemble simulations of present-day and near-future tropospheric ozone." Journal of Geophysical Research-Atmospheres **111**(D8).
- Tans, P. P., P. S. Bakwin and D. W. Guenther (1996). "A feasible global carbon cycle observing system: A plan to decipher today's carbon cycle based on observations." Global Change Biology **2**(3): 309-318.
- Volz-Thomas, A., M. Berg, T. Heil, N. Houben, A. Lerner, W. Petrick, D. Raak and H. W. Patz (2005). "Measurements of total odd nitrogen (NO<sub>y</sub>) aboard MOZAIC in-service aircraft: instrument design, operation and performance." Atmospheric Chemistry and Physics **5**: 583-595.

WMO (2003). "Report of the 11th WMO/IAEA Meeting of Experts on Carbon Dioxide Concentration and Related Tracer Measurement Techniques, Tokyo, Japan, 25–28 September 2001, Tech. Rep. 148, World Meteorological Organisation – Global Atmospheric Watch, Geneva, Switzerland."

# **Chapter 2 Advancing the techniques for high-accuracy continuous measurements of CO<sub>2</sub>/CH<sub>4</sub>/H<sub>2</sub>O on board a commercial airliner**

## **2.1 Introduction**

Concentrations of carbon dioxide (CO<sub>2</sub>) in the atmosphere have been measured as early as the 19th century using chemical methods (Callendar 1940; Fonselius et al., 1955); however, those early discrete observations of CO<sub>2</sub> in the atmosphere lacked high accuracy and were likely disturbed by local influencing factors. Nevertheless, analyses of “accurate” measurements of CO<sub>2</sub> of unpolluted air since the late 19th century showed that the concentration of CO<sub>2</sub> tended to increase (Callendar 1938). In the 1950s, there was a heated discussion on whether a significant trend existed in the mixing ratio of CO<sub>2</sub> in the atmosphere (Revelle et al., 1957; Callendar 1958; Bray 1959). In 1958 accurate continuous measurements of CO<sub>2</sub> were implemented using analyzers based on the non-dispersive infrared (NDIR) technique in Antarctica and at Mauna Loa Observatory (Pales et al., 1965). Those accurate continuous measurements confirmed the trend in the increase of CO<sub>2</sub> in the atmosphere. The instrument, described by Smith (1953), detects absorptions of infrared radiation by CO<sub>2</sub> and has the ability to provide accurate CO<sub>2</sub> measurements with calibrations by air standards. Since then measurements of CO<sub>2</sub> using the NDIR technique have been widely employed to monitor atmospheric CO<sub>2</sub> concentrations (Keeling et al., 1976). Also in 1958, air samples were collected in glass

flasks above the North Pacific Ocean during flights by the United States Air Force. The analysis results of flasks taken during flights revealed that the variability of CO<sub>2</sub> in the free atmosphere was smaller than at the surface. Early investigation on vertical distribution of atmospheric CO<sub>2</sub> had also been made from 1957 to 1961 by collecting air samples in 250 and 500 ml gas burettes with an airplane (Bischof 1962).

Among the wide variety of platforms (from ground-based stations, towers, ships, aircraft and balloons to satellites) on which CO<sub>2</sub> measurements can be acquired, aircraft measurements are essential for observations in the free troposphere and lower stratosphere covering regional to continental scales. However, obtaining measurements on board aircraft is challenging due to the difficulty of ensuring high accuracy under severe conditions of changing pressure and temperature as well as mechanical stress due to shock and vibration. Therefore, initially the primary method of acquiring airborne CO<sub>2</sub> measurements was to collect air samples in flasks or other containers during a flight and analyze the air later in the laboratory (Keeling et al., 1968). Flask samples taken from mid day aircraft profiles for atmospheric CO<sub>2</sub> and other trace gas analysis have been collected for several decades (Tanaka et al 1983, Francey et al 1999).

Nowadays, flask measurements are still a reliable way for airborne measurements to determine concentrations of species of interest in the atmosphere. Although very reliable, flask measurements have limitations in terms of their ability to capture temporal and spatial variability information, especially for observations within the boundary layer. Therefore, in situ measurements are desired to study high frequency variability and to quantify boundary layer mixing process (Tans et al, 1996). This is due to the fact that

representation of vertical distribution of atmospheric CO<sub>2</sub> is challenging for models, and is responsible for large cross-model variations (Gerbig et al, 2008, Stephens 2007, Denning et al, 2008). In addition, in situ column average measurements are better than those determined by only flask profiles (Bakwin et al, 2003), which is useful and necessary for validating FTS and satellite column measurements.

During the last 30 years, high-accuracy in situ airborne CO<sub>2</sub> measurements (mainly using the NDIR technique) have been carried out both in aircraft campaigns and in routine flights (Boering et al., 1994; Anderson et al., 1996; Daube et al., 2002; Machida et al., 2002; Shashkov et al., 2007; Machida et al., 2008). Methane (CH<sub>4</sub>) has received increasing attention as the second most important greenhouse gas after CO<sub>2</sub> because of the high uncertainty of its sinks and sources (Houweling et al., 2006; Keppler et al., 2006; Miller et al., 2007; Frankenberg et al., 2008). However, only in recent years has high-accuracy in situ CH<sub>4</sub> instrumentation become available for fast response airborne measurements (Jimenez et al., 2005).

The increasing need and high accuracy requirements for in situ observations of CO<sub>2</sub>, CH<sub>4</sub> and H<sub>2</sub>O on board aircraft demand improvement of the measurement techniques. Generally, the advancements can be categorized as: 1) Improving time resolution while maintaining similar precision and accuracy; 2) reducing the instrument size and weight; 3) reducing the maintenance. In this chapter, we present the results of investigation and improvement on different techniques for aircraft measurements, based on the requirements presented in Chapter 1.3. The rest of the chapter is organized as follows. In Chapter 2.2, comparisons of different techniques for airborne measurements of CO<sub>2</sub> and

CH<sub>4</sub> are presented. Experiments and advancements for analyzers based two different techniques are described in detail in Chapters 2.3 and 2.4, respectively. Chapter 2.5 summarizes the chapter and gives an outlook for future development.

## 2.2 Measurement techniques

There are a number of analytical methods capable of measuring CO<sub>2</sub> concentrations (such as chemical, gas chromatography and mass spectrometry) with high precision; however, considering the strict restrictions of weight and size (see Chapter 1.3.2.2) for deployment on board a commercial aircraft, the light absorption spectroscopy is the most appropriate technique. The basic principle of determining gas concentrations by the light absorption spectroscopy technique is described by the Beer-Lambert law.

### 2.2.1 The Beer-Lambert law

The Beer-Lambert law states that the logarithm of transmission (or transmissivity),  $T$ , of light through a substance (for the case of gases) is proportional to the product of the concentration of the absorbers,  $C$ , and the distance the light travels through the sample gas (see Eq. 1.1)

$$T = \frac{I}{I_0} = e^{-\sigma l C} \quad (2.1)$$

Here  $I_0$  and  $I$  are the intensity of the incident light and the transmitted light, respectively.  $\sigma$  is the absorption cross section of the absorber, which is dependent on the frequency of incident light and has a unit of  $\text{cm}^{-1}$  when the concentration of  $C$  is given in mole fraction. The absorption cross section ( $\sigma$ ) can be expressed by a line-strength and a line-shape

function. In spectroscopy, a closely-related term that is often used is optical density (OD), which is defined as follows:

$$OD = -\ln\left(\frac{I}{I_0}\right) = \sigma lC \quad (2.2)$$

The OD can be directly measured by a photo detector and is proportional to the concentration of absorbers. In spectrometry, the signal to noise ratio of a measurement is determined by the OD value and the detection sensitivity of the photo detector. Given the performance of a photo detector, the larger the OD is, the better the signal to noise will be. On the other hand, it is also important to make sure that no saturation of absorption is reached, which limits the OD value to a relatively small value so that a large dynamic range of concentration of absorbers can be obtained.

Given a concentration of an absorber, the OD value can be increased either by increasing the distance that light travels through the sample gas or selecting a proper frequency (range) to obtain a large absorption cross section, or by increasing the sample pressure. Use of multi-pass cell will effectively increase the length of the light path (White 1942; Briesmeister et al., 1984) while the HITRAN (**h**igh resolution **t**ransmission) database (Rothman et al., 2005; Rothman et al., 2009) provides a good reference for selecting appropriate absorption lines. Although increasing the sample pressure is able to increase the absorption, it may cause pressure-broadening effects (detailed descriptions are given in Chapter 3.4.1.2). Several spectroscopy techniques have been successfully implemented to perform high-precision measurements of atmospheric CO<sub>2</sub>, and possibly CH<sub>4</sub> and H<sub>2</sub>O. Theoretically, the absolute concentrations can be determined from spectroscopic parameters, i.e. the distance that the light travels through the sample gas and the strength



of absorption cross section; however, the error is significantly larger than the required measurement accuracy due to the uncertainties associated with these parameters (McManus et al., 2008). Therefore, calibrations are required in order to achieve high accuracy measurements of ambient trace gases.

### **2.2.2 The NDIR technique**

The NDIR technique determines mixing ratios of CO<sub>2</sub> and H<sub>2</sub>O by measuring strong broadband absorptions of CO<sub>2</sub> at around 4.26 μm and H<sub>2</sub>O at around 2.59 μm. Optical filters are normally employed to select the range of spectra for the absorption measurements. The typical spectral ranges are from 4.185 μm to 4.335 μm for CO<sub>2</sub> and from 2.565 μm to 2.615 μm for H<sub>2</sub>O. Within the spectral range for measuring CO<sub>2</sub> absorptions, there are also H<sub>2</sub>O absorption lines (Rothman et al., 2009). Therefore, the presence of H<sub>2</sub>O interferes with measurements of CO<sub>2</sub> concentration by direct absorptions and causing absorption line broadening of CO<sub>2</sub>. Due to this interference effect, H<sub>2</sub>O is usually removed for high-precision CO<sub>2</sub> concentration measurements. For measuring CO<sub>2</sub> in dry air, the NDIR technique is also sensitive to isotopic ratios of CO<sub>2</sub>, which may cause a measurement error of ~ 0.1 ppm for measuring CO<sub>2</sub> in synthetic air (Tohjima et al., 2005) when referenced to ambient air standards.

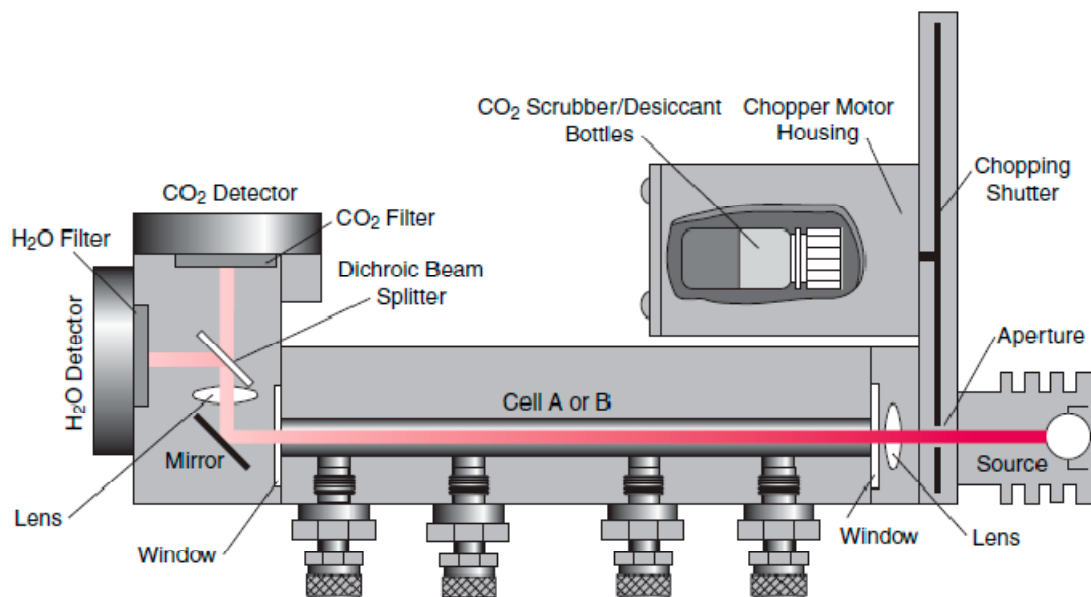


*Figure 2.1 Schematic of the LI-7000 analyzer. The infrared light from the light source passes through a single cell at once and is split by a splitter before arriving at the CO<sub>2</sub> and H<sub>2</sub>O detectors (this figure is from the data sheet of the LI-7000)*

An NDIR analyzer normally consists of near infrared light emitters, optical absorption cells, and photodetectors (see Fig. 2.1). A representative commercially available NDIR analyzer is LI-7000 (Li-Cor, Inc., Lincoln, NE, USA). The LI-7000 analyzer employs two cells to perform differential measurements. The temperature of the light source is controlled at 1250 K to eliminate the potential drift of the light intensity. A chopping shutter is introduced to select the light source through one of the two absorption cells. The detector and chopper housings are free of CO<sub>2</sub> and H<sub>2</sub>O. Solid state PbSe detectors are used in this analyzer. The detectivity (i.e. the signal-to-noise ratio S/N) of PbSe detectors increases when temperature decreases. Therefore, cooling the detectors will improve the S/N ratio and thus improve the precision of measurements of CO<sub>2</sub> or H<sub>2</sub>O by the NDIR technique. The response of an NDIR analyzer is not linear, but can be fitted

with a quadratic curve for high-accuracy CO<sub>2</sub> concentration measurements (Zhao et al., 2006).

### 2.2.3 The CRDS technique

In the cavity ring-down spectroscopy (CRDS) technique, the gas sample is analyzed in a high-finesse optical cavity; the optical absorbance of the sample is determined by the light dissipation rate (or ring-down time) in the optical cavity, thus typically providing parts-per-billion mixing ratio or isotopic ratio measurements of a particular gas species of interest which are, to a good approximation, independent of the intensity fluctuations of the excitation light source. The advantage of this technique is that it allows one to obtain high sensitivity through long path light absorption and measurements of the light dissipation rate instead of the directly absorbed signal strength. This technique was first implemented by (Okeefe et al., 1988) using a pulsed laser source.

#### 2.2.3.1 Theoretical background

In a typical CRDS system, the cavity is comprised of a set of mirrors, with the reflectivity,  $R$ , larger than 99.99%. With the approximation of  $\ln(1 - R) \cong 1 - R$  when  $R$  is close to 1 and according to the Beer-Lambert law, the intensity of the light reaching the detector at time  $t$ ,  $I(t)$ , can be determined as an exponential function of time (Romanini et al., 1993):

$$I(t) = I_0 e^{-\frac{t}{\tau}} = I_0 e^{-\frac{c(1-R+\alpha l)t}{l}} \quad (2.3)$$

where  $I_0$  is the initial light intensity that reaches the detector after the pulse laser light is injected into the cavity,  $l$  is the cavity length,  $c$  is the speed of light when it travels

through the sample gas, and  $\alpha$  is the frequency-dependent absorption coefficient that is equal to  $\sigma C$ .  $\sigma$  is the absorption cross section and  $C$  is the concentration of the absorber in the sample gas. The ring-down time (RDT) is

$$\tau = \frac{l}{c(1 - R + \alpha l)} \quad (2.4)$$

When there is no sample gas in the cavity, the RDT becomes

$$\tau_0 = \frac{l}{c(1 - R)} \quad (2.5)$$

From Eqs. 2.4 and 2.5, we can derive

$$C = \frac{1}{\sigma c} \left( \frac{1}{\tau} - \frac{1}{\tau_0} \right) \quad (2.6)$$

Using Eq. 2.6 and experimentally-determined  $\tau$  and  $\tau_0$ , the mixing ratio of an absorber in the gas sample could be calculated if the absorption cross section  $\sigma$  at a certain frequency is also known. Note that the determination of  $\tau$  and  $\tau_0$  does not depend on the intensity of the light source and thus it is not affected by possible intensity fluctuations.

### 2.2.3.2 Sensitivity

From Eq. 2.6, we can derive the sensitivity of a CRDS instrument

$$\Delta C = \frac{1}{\sigma c} \left( \frac{\Delta \tau}{\tau^2} \right) \quad (2.7)$$

Several measures could be taken in order to increase the sensitivity of the CRDS instrument: 1) A proper frequency to obtain a larger absorption cross section should be selected; 2) improving the reflectivity of the mirrors ( $R$ ) or increasing the length of the cavity ( $l$ ) to improve the RDT; 3) improving the detection limits for changes in RDT.

Practically, there are other issues that may influence the measures to increase the sensitivity. For example, frequency selection is limited by the adjusted frequency range of the laser and needs to take into account potential interference with absorption lines from other species; increasing the length of the cavity also means increasing the size of the cavity, thus the total size of the CRDS instrument. Besides this, the cavity mode is another aspect that needs to be taken into consideration when designing a resonator for a CRDS instrument (Mazurenka et al., 2005).

## **2.2.4 Other techniques**

### 2.2.4.1 Cavity enhanced absorption spectroscopy

Cavity enhanced absorption spectroscopy (CEAS) employs a cavity that is similar to those used in the CRDS technique; however, the time-integrated transmitted light strength instead of the cavity ring-down time is detected. The CEAS technique, also known as integrated cavity output spectroscopy (ICOS), is able to achieve a high detection sensitivity that is comparable to the CRDS technique but with a simpler experimental setup (O'Keefe 1998). The schematic of an experimental setup employing the CEAS technique is shown in Fig. 2.2.

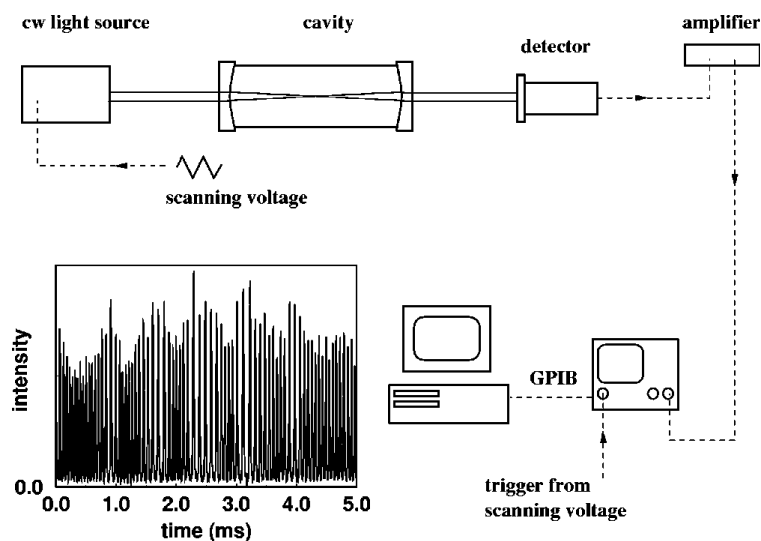


Figure 2.2 Schematic of an instrument using the CEAS or ICOS technique. The light source from a continuous wave laser is injected into the cavity; the integrated signal is detected by a photodiode and the signal is amplified and output into an oscilloscope and a PC for further analyses (Engeln et al., 1998).

The CEAS technique could be coupled with broad band light sources and thus provide the ability to detect extremely weak absorptions.

#### 2.2.4.2 Quantum cascade laser

Quantum cascade lasers (QCLs) are semiconductor lasers that emit lights within the mid- to far-infrared range. This laser could be integrated with any spectroscopic techniques; however, this kind of laser has been widely employed in a series of instruments developed by Aerodyne Research, Inc. so that QCL has been used to denote the technique (Nelson et al., 2004; McManus et al., 2008; Tuzson et al., 2008). A typical QCL optical module is illustrated in Fig. 2.3. The light from a QC laser is focused at a pinhole for alignment, and then directed into a multi-pass sample cell; after a fixed number of passes in the cell, i.e. known optical path length (typically 55.6 m or 76.5 m), the light reaches a

thermally cooled photodetector. There are also two other reference beams produced by a beamsplitter. One is used for locking the laser wavelength and the other is used to normalize laser output fluctuations, as pulsed laser usually outputs light with an amplitude noise of  $\sim 1\%$ .

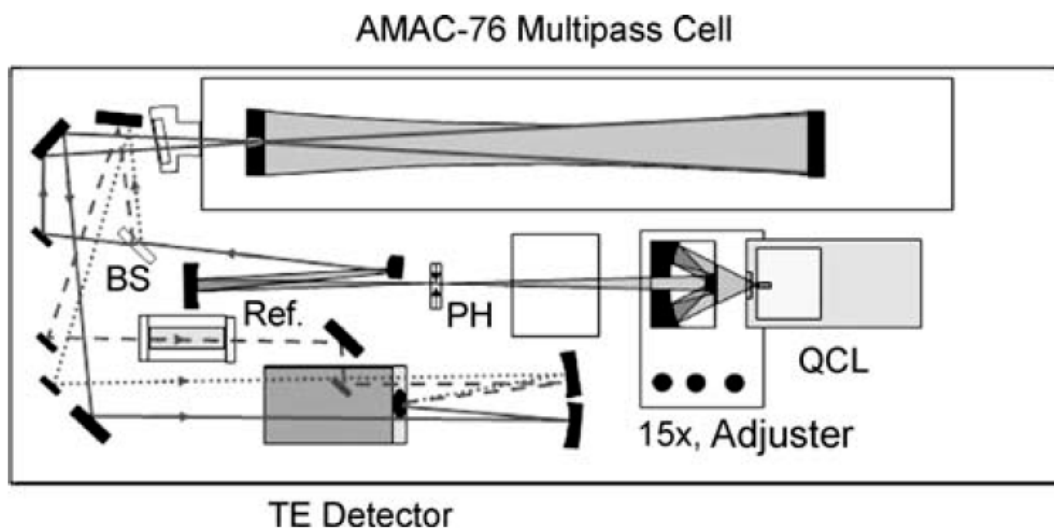


Figure 2.3 Diagram of the optical module for the QCL instrument. QCL is the quantum cascade laser on a Peltier cooler, in a sealed enclosure; 15 $\times$  is the 15 power reflecting objective; Adjuster is the 3-axis position adjuster for objective; PH is the 200  $\mu\text{m}$  pinhole; BS is the BaF2 beamsplitter (McManus et al., 2008).

The concentrations of a particular trace gas are derived from the spectroscopic retrieval of the integrated area of the obtained absorption spectrum, pressure, temperature, absorption path length and the laser spectral line width. The QCL technique has the advantage of detecting strong absorption lines in the mid-infrared region of many species of trace gases and thus is able to provide sub-ppb-level detection of these gases. However, the method of directly detecting light absorption intensity is sensitive to fluctuations of light intensity from the laser and the detector non-linearity. Measures taken to compensate these drawbacks add complexity to the system. Besides, a powerful

pump is required to obtain measurements of fast response due to the relatively large volume of the sample cell (0.5 L). These made the system relatively expensive compared to other techniques.

## 2.3 Characterization and advancement of an NDIR analyzer

### 2.3.1 The NDIR analyzer

A commercially available flight analyzer (AOS Inc., Boulder, CO, USA) based on the NDIR technique has been tested with the aim of deployment on board a commercial airliner within the IAGOS project. This analyzer consists of two infra-red light emitters, two gas cells and two detectors (see Fig. 2.4). The pressure in a 2 l buffer located downstream of the reference and sample cells is stabilized at  $\sim 1100$  mbar, a level that is higher than the possibly maximum possible ambient pressure. The pressure drop between the gas cells and the pressure buffer is kept small by shortening the length of the tubing with the diameter of 1/4".

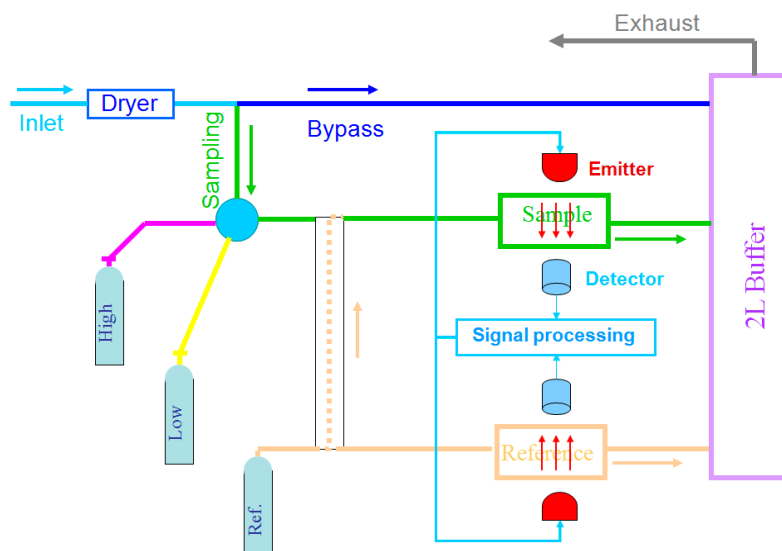


Figure 2.4. Schematic diagram of the NDIR CO<sub>2</sub> analyzer system



Three CO<sub>2</sub>-in-air standards are employed in the analyzer, which are denoted as Ref., Low and High. The reference gas has a CO<sub>2</sub> mixing ratio of ~ 380 ppm, a level that is around the ambient mean value. The low and high gases have CO<sub>2</sub> mixing ratios of ~ 360 ppm and ~ 400 ppm, respectively. The method for using the three gases corresponds to three operation modes: Measurement, Zero calibration, and Span calibration. During the measurement mode, the ambient air flows through the sample cell and the reference gas flows through the reference cell. During the Zero calibration, the reference gas flows through the sample cell while no gas flows through the reference cell; thus both cells contain the reference gas, providing a background (zero) signal. The Zero calibration is short enough to prevent diffusion of air from the pressure buffer back to the reference cell. During the Span calibration, Low or High gas flows through the sample cell while reference gas flows through the reference cell, resulting in a sensitivity measurement of the analyzer.

The flows through the sample and reference cells are 180 sccm (standard cubic centimeters per minute, i.e., equivalent to the volume flow rate at 273.15 K and 1013.25 hPa) and 10 sccm. The flow of ambient air is bypassed through an additional path at the same rate of 180 sccm when a Zero or Span calibration takes place, so that the sample inlet remains constantly flushed. The water vapor in the sample air is removed by a chemical dryer tube filled with magnesium perchlorate (Mg(ClO<sub>4</sub>)<sub>2</sub>) in order to measure the dry mole fraction of CO<sub>2</sub> in air. The chemicals in the dryer are consumed and need replacement every two or three 3 h flights.

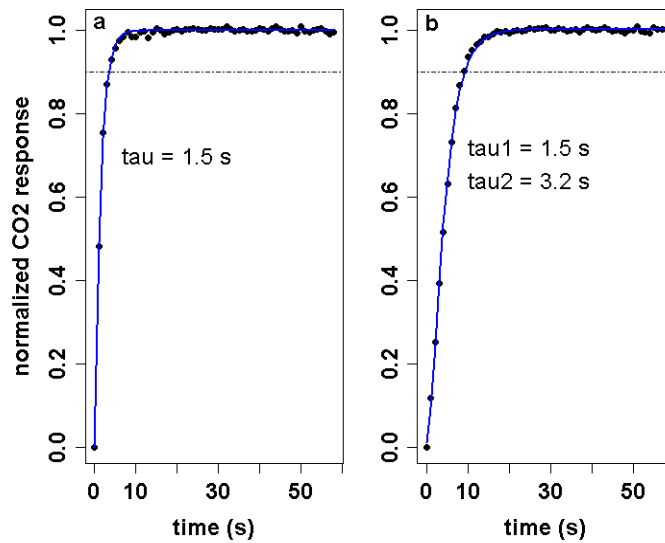


Figure 2.5 (a) One exponential curve fit for the response time from calibration to sampling gas, 90% response time ~3.5 seconds, (b) sum of two exponential curve fit for the response time from one sample gas to another, 90% response time ~9 seconds.

The cell volume is approximately 5 cc. With a 180 scfm flow rate, the 90% response time is about 3.5 seconds, which agrees well with the number calculated from laboratory tests alternating between calibration and sampling gases. The time response can be fitted into one exponential curve. However, the 90% response time of switching from one sample gas to another sample gas with a different CO<sub>2</sub> concentration is about 9 seconds. The increase in the response time is due to the mixing of air in the chemical dryer tube. The response can then be fitted to the sum of two exponential curves (see Fig. 2.5).

### 2.3.2 System stability and linearity

#### 2.3.2.1 System stability

To assess the stability of the NDIR analyzer, CO<sub>2</sub> concentrations of the gas from a synthetic air standard tank have been continuously measured for 1.5 hours. For this test,

the analyzer is operated in either Measurement or Calibration mode, with 20 seconds for Calibration and 120 second for Measurement. In the first step, the measurements are processed with only an initial calibration at the beginning. The sensitivity is obtained using the difference of known CO<sub>2</sub> concentrations of the sample and reference gases divided by the difference of the raw signal of Measurement and Calibration. The time series of the measurements are shown in Fig. 2.6 a.

In order to assess the stability of the CO<sub>2</sub> concentration measurements, the Allan deviation is here introduced. The Allan deviation is also called two-sample deviation and is defined as (Barnes et al., 1971)

$$\sigma_y(\tau) = \sqrt{\frac{1}{2} \langle (\Delta \overline{y^\tau})^2 \rangle} = \sqrt{\frac{1}{2(N-1)} \sum_{i=1}^{N-1} (y_{i+1} - y_i)^2} \quad (2.8)$$

Here  $\tau$  is the sampling time interval and  $N$  is length of the dataset. Note that the variance is computed using the difference of two adjacent values in the Allan deviation, rather than the difference between values and the mean in the standard deviation. The Allan deviation is convergent, whereas the standard deviation of a series of measurements is divergent and is a function of the data length (Barnes et al., 1971). Eq. 2.8 has been extended to calculate Allan deviations with different sampling time intervals by averaging  $m$  adjacent measurement values (Allan 1987)

$$\sigma_y(\tau) = \sqrt{\frac{1}{2(N-2m+1)} \sum_{k=1}^{N-2m+1} (\overline{y_{k+m}^\tau} - \overline{y_k^\tau})^2} \quad (2.9)$$

Here  $\overline{y_{k+m}^\tau}$  and  $\overline{y_k^\tau}$  are still adjacent measurement values. With Eq. 2.9, Allan deviations can be calculated with different averaging times, which are useful to

characterize the noise or drift in the measurement. Allan deviations are computed to evaluate the maximum averaging time for the measurements of CO<sub>2</sub> concentrations by the NDIR analyzer (Fig. 2.6 c, d).

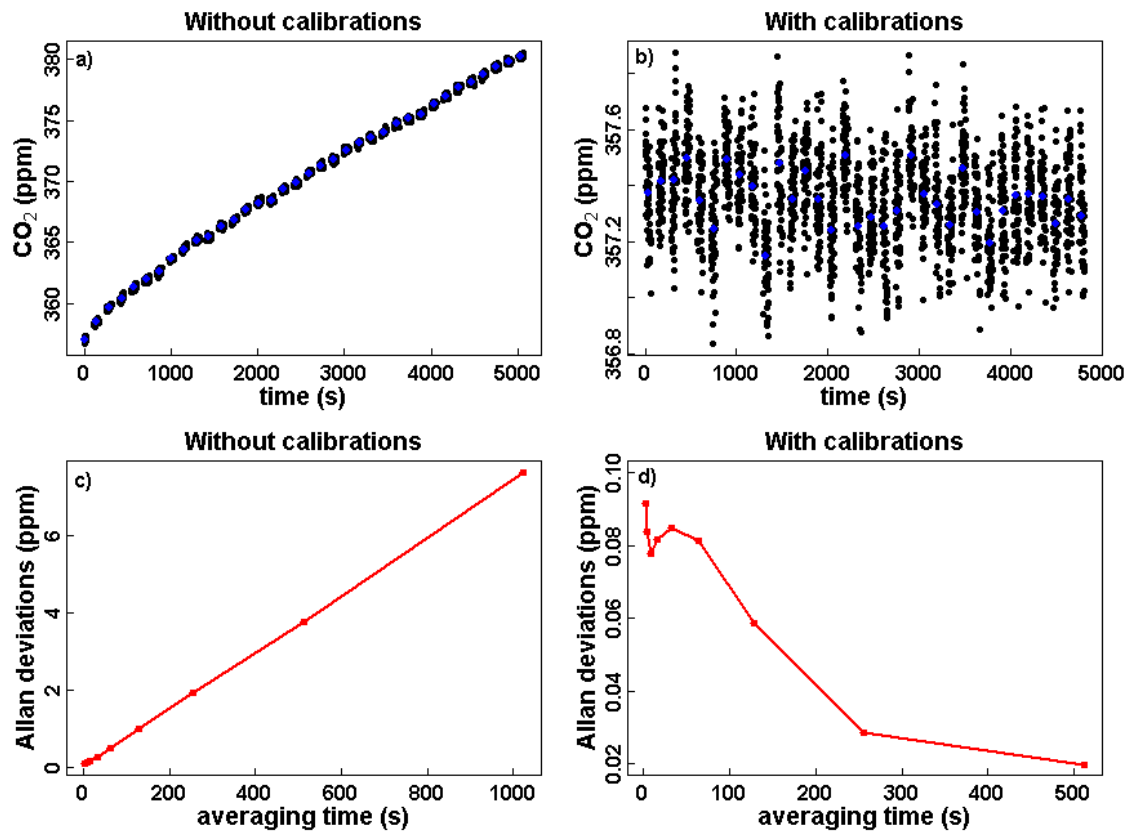


Figure 2.6. Measurements of CO<sub>2</sub> concentrations of a standard gas by the NDIR for 1.5 hours. a) The measurement data are processed with only an initial calibration; b) the measurement data are processed with calibrations every 120 seconds; c) and d) the Allan deviation plots of the CO<sub>2</sub> concentration measurements in figs. a and b;

In the second step, the measurements are first detrended by the background signals obtained from linearly interpolating calibrations and the CO<sub>2</sub> concentrations with calibrations are shown in Fig. 2.6b. The corresponding Allan deviations (see Fig. 2.6 d) indicate that the deviations at all scales are smaller than 0.1 ppm; however, the standard deviation of these measurements is ~ 0.2 ppm. The reason is that the CO<sub>2</sub> concentrations

within a measurement cycle are more correlated than between the cycles, which makes the Allan deviation smaller. With frequent calibrations, i.e. every 2 minutes, the accuracy of the measurements by the analyzer could be better than 0.2 ppm. Note that the stability of the CO<sub>2</sub> concentration measurements by the NDIR analyzer is subject to the pattern of the drift of calibration signals. When the drift is far from linear, the actual accuracy is reduced.

Temperature variation around the housing of the detectors and the light emitters has significant influence on the raw signals of the analyzer despite the fact that the two detectors of the analyzer are thermally controlled at constant temperature. To characterize the influence of temperature variation, localized heating was applied via heat-dissipating resistors to the sensitive components of the NDIR analyzer, e.g. detectors and light emitters. The temperatures of the housings of these components were logged by platinum resistance thermometer (RTD) sensors. The experiments reveal that CO<sub>2</sub> readings derived from the raw signals change ~ 8.3 ppm for every degree change of the housing temperature of light emitters and ~ 1.8 ppm for every degree change of the housing temperature of detectors.

In order to minimize impact of changing heat dissipation from valve switching between measurement and calibration, and to utilize the fast response performance, a calibration period of 12 seconds is used. This short calibration period also has the advantage of maximizing the duty cycle (fraction of time the instrument measures sample gas). Nevertheless, drifts in the measurements due to the valve switching thermal effect were found for the period of 13 seconds to 30 seconds after calibrations, ranging from 0.7 ppm

to 0.1 ppm. Corrections based on an exponential time response curve were applied to remove this impact on the measurements.

In addition, the response of the NDIR analyzer is sensitive to vibrations and shocks. In the laboratory, shaking of the rack of the analyzer could cause signal jumps with a magnitude of  $\sim 100$  ppm. The reason was found to be vibration-sensitive the connectors on an electronic circuit board of the analyzer. These connectors were removed and the wires were soldered onto the electronic circuit board directly.

#### 2.3.2.2 Linearity

Four external air standards were measured by the NDIR analyzer, and the sensitivity was determined from the internal Ref. and Low gas. Both linear and quadratic curves were used to fit the four CO<sub>2</sub> concentrations determined by the NDIR analyzer (see Fig. 2.7). Judging from the residuals of the fits, the response of the NDIR analyzer was not linear; a quadratic fit would be able to compensate for the nonlinearity and result in accuracy better than 0.1 ppm. This means that at least 3 calibration gases are required during flight. The CO<sub>2</sub> concentrations were calibrated against WMO standard gases using a LoFlo system (Da Costa et al., 1999) and a GC system, while the CH<sub>4</sub> concentrations were calibrated using only the GC system. The uncertainties for the working standards are estimated to be less than 0.1 ppm for CO<sub>2</sub> on absolute scales.

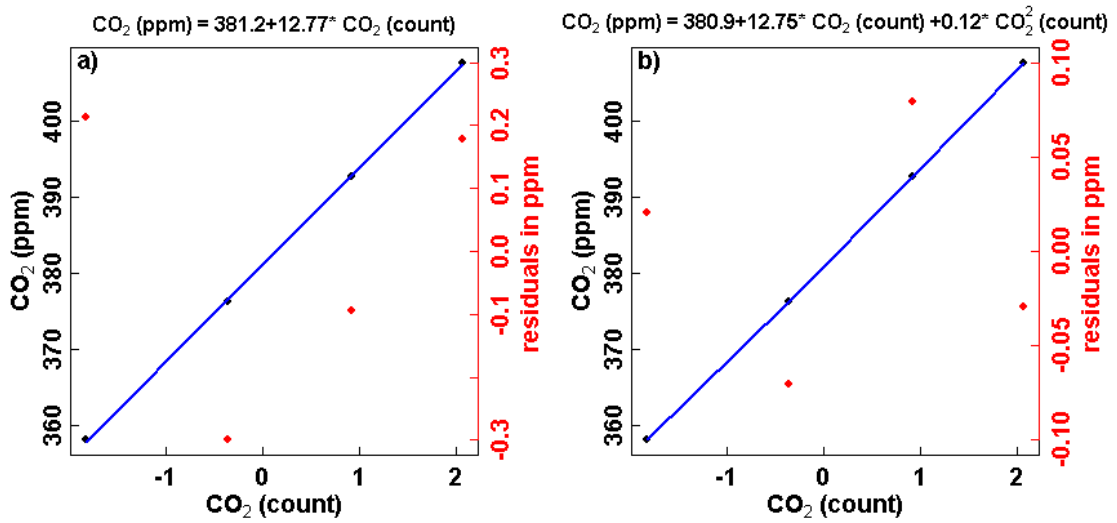


Figure 2.7. Linearity of the measurements of CO<sub>2</sub> concentrations by the NDIR analyzer. A linear curve is used to fit the data (a); A quadratic fit is used to fit the data (b). The residuals of the fits are shown as red dots in the plots and read on the right axis. CO<sub>2</sub> (count) is the raw signal output of the NDIR analyzer.

### 2.3.3 Flow modifications

As discussed in section 2.3.2, the NDIR analyzer requires frequent calibrations and thus demands a significant amount of gases. A brief calculation is given below to explore the total volume of gases required for a continuous operation of 90 days, presumably on board a commercial aircraft. The reference gas flows through the reference cell at  $f_r=10$  sccm during the Measurement or Sensitivity mode, while it flows through the sample cell at  $f_s=200$  sccm during the Calibration mode. The fraction of time with 10 sccm is  $20/(120+20)$  and the fraction of time with 200 sccm is  $120/(120+20)$ . The total volume can be estimated using Eq. 2.10:

$$V = \left( \frac{120}{120 + 20} \times f_r + \frac{20}{120 + 20} \times f_s \right) \times 60 \times 24 \times 90 \quad (2.10)$$

The total volume of gases is estimated to be ~ 4800 l, with ~1100 l consumed during the Measurement mode and ~3700 l during the Calibration mode. To provide such amount of gases, a 30 l cylinder is needed, which exceeds the space capacity of the IAGOS instrumentation. Therefore, the gas consumption has to be reduced if this NDIR analyzer were to be deployed on board a commercial airliner. The flow of reference gas through the reference cell could be reduced from 10 sccm to 1 sccm, thus the gas consumption would reduce from ~ 1100 l to ~ 110 l. However, a reduction of the flow of zero gas has to compromise with the response time of the NDIR analyzer, as this flow rate should be the same as the sampling flow rate so that the calibrations are not biased by a different flow. Within IAGOS, the capacity of usable calibration gases is ~ 1100 l. Therefore, the flow rate of reference gas during the Calibration mode would have to be reduced by a factor of  $3700/1100 = 3.4$ . Note that reduction of the flow implies increases of the response time of the analyzer. Alternatively, the volumes of the gas cells could be reduced with the expense of the precision of the NDIR analyzer.

The volume of each gas cell is 5 cc. Two pairs of gas cells were built: one with a half of and the other with a quarter of the size of the original gas cells, i.e. with the volume of 2.5 cc and 1.25 cc. Experiments were carried out with all three versions of the gas cells to evaluate the response time of the analyzer as well as the corresponding precisions (see Fig. 2.8).



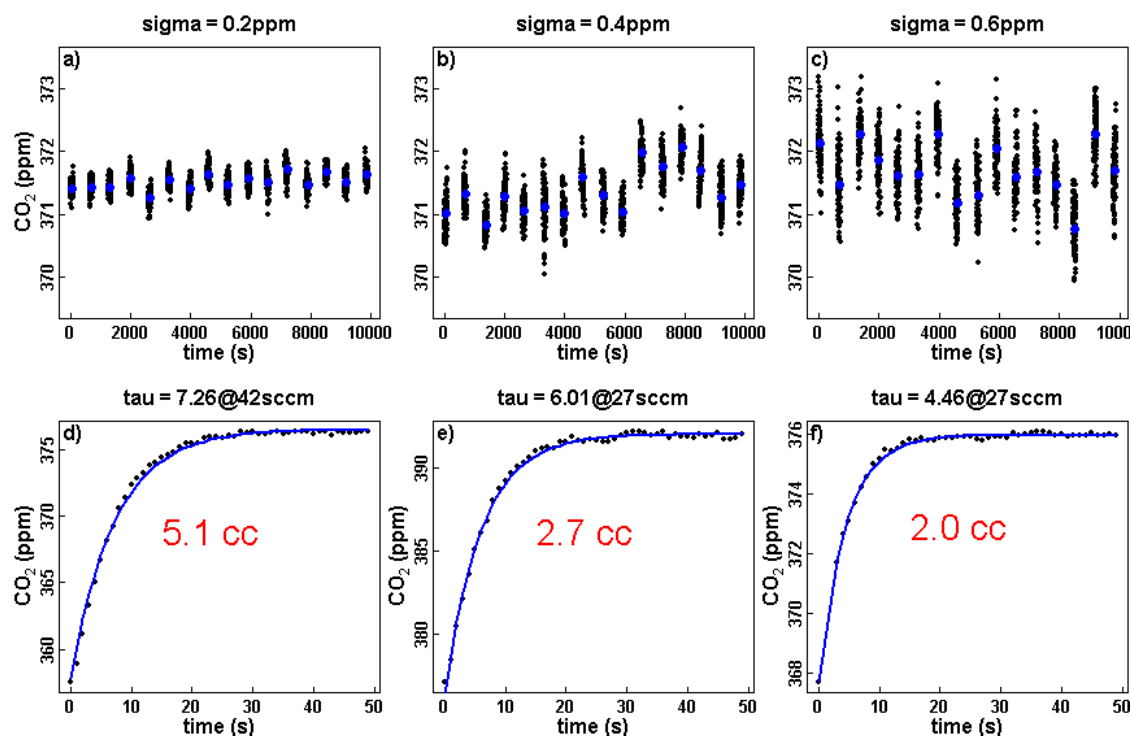


Figure 2.8. Precision and response time of  $\text{CO}_2$  concentration measurements by the NDIR analyzer with different sizes of gas cells: Figs. a, b, and c show the  $\text{CO}_2$  concentration measurement series with 5 cc, 2.5 cc and 1.25 cc cells, the standard deviations are shown in the title, and the blue dots give the average values of  $\text{CO}_2$  concentrations in a measurement cycle; figs. d, e, f show the flushing volumes ( $\sim 63\%$  gas exchange) of the different cell versions, i.e. 5 cc, 2.5 cc and 1.25 cc cells. The ideal volumes of the cells are determined and shown in red in Figs. d, e, and f. Note that the flow rates used are different during testing of the three different versions.

The results reveal that the noise level increases from 0.2 ppm to 0.6 ppm when the cell volumes change from 5 cc to 1.25 cc; however the flushing volumes decrease from 5.1 cc to 2.0 cc. Theoretically, the flushing volume should be around 1.25 cc when the 1.25 cc cells are used, and the reason might be that the volume of the associated tubing becomes significant when the cell volume is small enough. These experiments indicate that employment of the 1.25 cc cells implies that the precision is 3 times worse while the flow rate could be cut by a factor of 2.5.

### **2.3.4 The calibration system**

A calibration system is essential for the NDIR analyzer because of its instability and nonlinearity. Three CO<sub>2</sub>-in-air standards are used for in-flight calibrations and the calibration gases are contained in one 3.5 L fiber-wrapped aluminum cylinder (for the Ref. gas) and two 1.2 L aluminum cylinders (for Low and High gases). The measurement accuracy of the analyzer with a calibration system is dependent on the CO<sub>2</sub> concentration stability of calibration gases delivered into the sample and reference cells of the analyzer, especially in the case of long-term deployment in the field.

In order to investigate the long-term CO<sub>2</sub> concentration stability of the calibration system, 120-day laboratory tests have been carried out (Winderlich 2007). During these tests, the cylinders are attached with pressure regulators, followed by high pressure stop valves that block the flow when no experimental measurement is being carried out, while the valves of small cylinders are open all the time. These tests have characterized the influences of the diffusive and surface processes on the CO<sub>2</sub> concentrations of gases in small cylinders and pressure regulators. On one hand, the CO<sub>2</sub> molecular is adhesive to the wall of aluminum cylinders causing surface effect, and this effect is pressure dependent (Langenfels et al., 2005). The CO<sub>2</sub> concentration of the gas in the small cylinders immediately after filling is lower than that of the gas in the filling tank due to adsorption of CO<sub>2</sub> molecules on the walls of the small cylinders, while the CO<sub>2</sub> concentration of the gas in the small cylinders increases significantly when the pressure drops to a relatively low level of ~ 30 bar, due to the desorption of CO<sub>2</sub> molecules from the walls of these cylinders.

On the other hand, diffusion exists in the pressure regulators (e.g. 2-stage pressure regulators from Scott Specialty Gases), which has an impact on the CO<sub>2</sub> concentration of the gases in the high pressure side of the pressure regulator and eventually in the cylinders in the long run. The 1<sup>st</sup> stage of the Scott regulator is a Viton sealed piston. Because CO<sub>2</sub> preferably diffuses through the polymer in comparison to the other air components (Sturm et al., 2004), the air at the high pressure side gets depleted, at the low pressure side the CO<sub>2</sub> accumulates and then diffuses when it is higher than the ambient CO<sub>2</sub> concentration. Therefore, for a long term operation, the CO<sub>2</sub> concentration of gases in the cylinders decreases with time, while on each measurement, after more than 4 h storage, the CO<sub>2</sub> concentration increases with time in the beginning until the CO<sub>2</sub> depleted air in the pressure regulator is flushed. Tests show that a TESCOM regulator has smaller diffusive effect; however, the size is too large to be employed in an analyzer for airborne measurements.

These laboratory tests lead to a use strategy of the calibration system for the NDIR analyzer during flight: 1) Calibrating the CO<sub>2</sub> concentrations of gases in the small cylinders after filling instead of taking the values of the filling tanks to correct potential desorption effect; 2) using the cylinders only when the pressure is above 30 bars, a conservative value below which CO<sub>2</sub> concentration may have significant increases due to desorption of CO<sub>2</sub> molecules from the walls of the cylinders; 3) flushing the dead volume in the pressure regulators before measurements start during a flight; 4) calibrating the CO<sub>2</sub> concentrations of gases in small cylinders before and after deployment in the field to characterize long term drift in CO<sub>2</sub> concentration due to the diffusive effect. Keeping to

these rules, it can be guaranteed that the calibration system supplies the measurement system with a stable CO<sub>2</sub> concentration within an accuracy of 0.2 ppm.

In addition, the CO<sub>2</sub> mixing ratios of the calibration gases used for computing CO<sub>2</sub> concentration measurements should be derived from measurements of external standard gases by the analyzer. This is due to the fact that the responses of the NDIR analyzer are affected by the heat flow caused by valve switching, providing a biased calibration signal during calibrations. By applying the CO<sub>2</sub> concentration values derived from measuring external standard gases, this effect could be cancelled out.

### **2.3.5 Performance under simulated flight conditions**

A direct way to evaluate the performance of a flight analyzer is to perform a test flight with the analyzer onboard; however, a test flight is expensive and involves significant efforts associated with integration and logistic issues. Therefore, a more feasible alternative is to assess the performance of a flight analyzer under simulated conditions in the laboratory. For this test the NDIR analyzer was operated within an environmental chamber (Siemens AG, Chemnitz, Germany, type CH3030). The pressure inside the chamber was controlled according to the nominal pressure values that will be seen on board the rental aircraft, while the sample gas provided to the analyzer was from a calibration gas cylinder with 371.92 ppm.

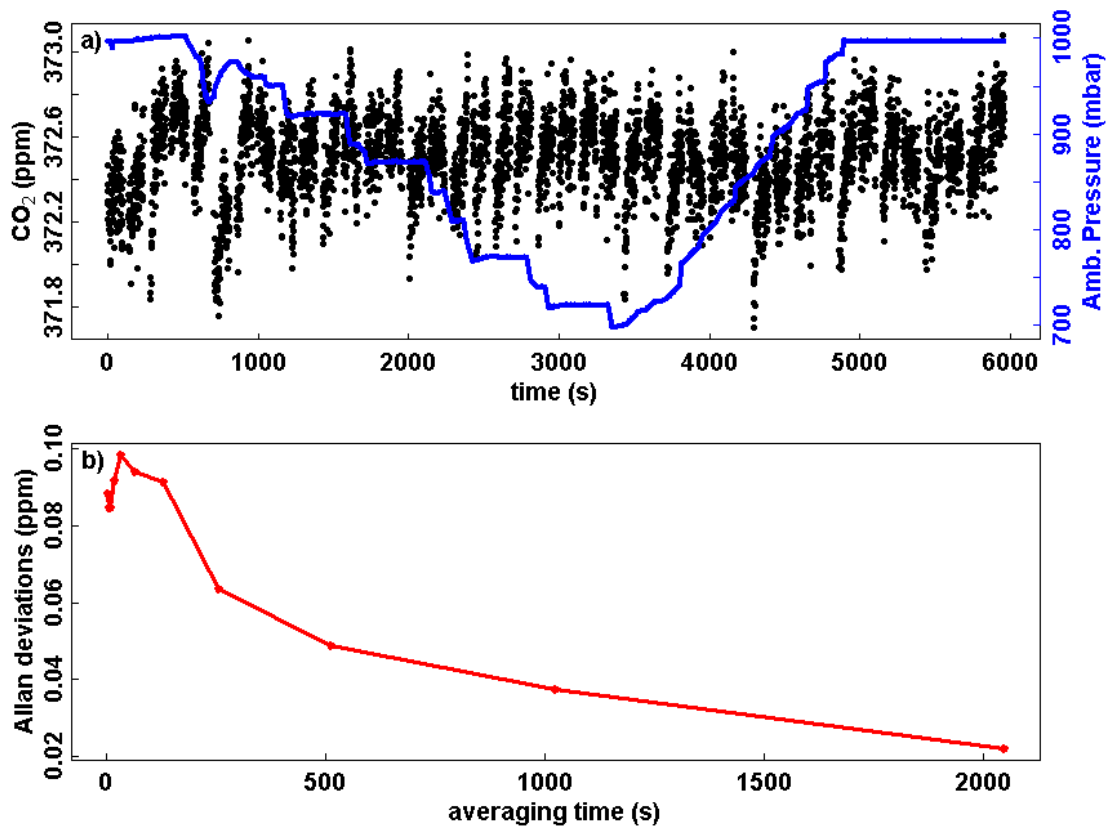


Figure 2.9  $CO_2$  mixing ratio measurements of a standard gas by the NDIR analyzer under changing pressure in an environmental chamber: a)  $CO_2$  mixing ratios measured by the NDIR analyzer, with the pressure values on the right axis; b) the Allan deviations of the measurements at different averaging intervals.

The test results are shown in Fig. 2.9. Note that larger variations are seen between 700 - 750 s, this is due to a rapid pressure change causing a false determination of the zero signal. Since the pressure change during real flights is limited to  $\pm 2$  mbar/sec, such a rapid pressure change will not occur; this period was therefore excluded from following analysis. The Allan deviations at all scales are smaller than 0.1 ppm. Above all the accuracy of the NDIR analyzer under the changing pressure conditions will be better than 0.2 ppm.

To summarize the laboratory test results of the NDIR analyzer: 1) The analyzer requires frequent calibrations; 2) a limitation of the capacity of calibration gases demands reductions in flow rates, which resulted in lower precision and increasing response time; 3) accuracy of the analyzer is subject to the pattern of the drift in the calibrations that is unpredictable; 4) three calibration gases are required to compensate for the nonlinearity of the analyzer, but not enough space is available for the IAGOS CO<sub>2</sub> instrumentation;

In addition, a low-maintenance non-chemical dryer is required for deployment on a commercial airliner. Considering all these factors, the NDIR analyzer is not a good candidate for the IAGOS CO<sub>2</sub> instrumentation. As a spin-off, this analyzer has been downgraded to be deployed on board a rental aircraft (Wilga PZL-104) for regular profiling in eastern Poland (Observations are presented in Chapter 3.3).

## **2.4 Characterization and advancement of a CRDS analyzer**

As the NDIR technique has been ruled out of the options for deployment on board a commercial airliner, there are a number of alternatives: the QCL technique, the CRDS technique and the CEAS technique. Considering the performance of these techniques with regard to the high requirements for precision, accuracy, and the ability of long term unattended operations, the CRDS technique was chosen as the next candidate for assessment. In this section, the characterization a CRDS analyzer will be presented, followed by improvement of the techniques with the aim to achieve the design of a CO<sub>2</sub> analyzer for IAGOS.

### 2.4.1 The CRDS analyzer

A flight analyzer based on the technique of wavelength-scanned cavity ring-down spectroscopy (WS-CRDS, subsequently referred to as CRDS) has been investigated. This technique has been successfully implemented in a ground-based greenhouse gas analyzer (Crosson 2008). The analyzer (Picarro Inc., CA, USA, model G1301) employs two lasers, a high-precision wavelength monitor, a high finesse optical cavity with three high-reflectivity mirrors (> 99.995 %), a photodetector and a computer (see Fig. 2.10). During the measurements, light at a specific wavelength from a laser is injected into the cavity through a partially reflecting mirror. The light intensity then builds up over time and is monitored through a second partially reflecting mirror using a photodetector located outside the cavity. The “ring-down” measurement is made by rapidly turning off the laser and measuring the time constant of the light intensity as it exponentially decays. The lasers are tuned to scan over the individual spectral lines of  $^{12}\text{C}^{16}\text{O}_2$  at a wavelength of 1603 nm, and  $^{12}\text{CH}_4$  and  $\text{H}_2\text{O}^{16}\text{O}$  at a wavelength of 1651 nm producing a high resolution spectrum of each. Fits to each of these high-resolution absorption spectra are then obtained, from which the constituent quantities of the gas sample are determined. The temperature and pressure of the gas sample are tightly controlled at 45 °C and 140 Torr in the G1301 (variations of less than 20 mK and 0.1 Torr, respectively), leading to highly stable spectroscopic features. The measurement speed is around 5 seconds (0.2 Hz).

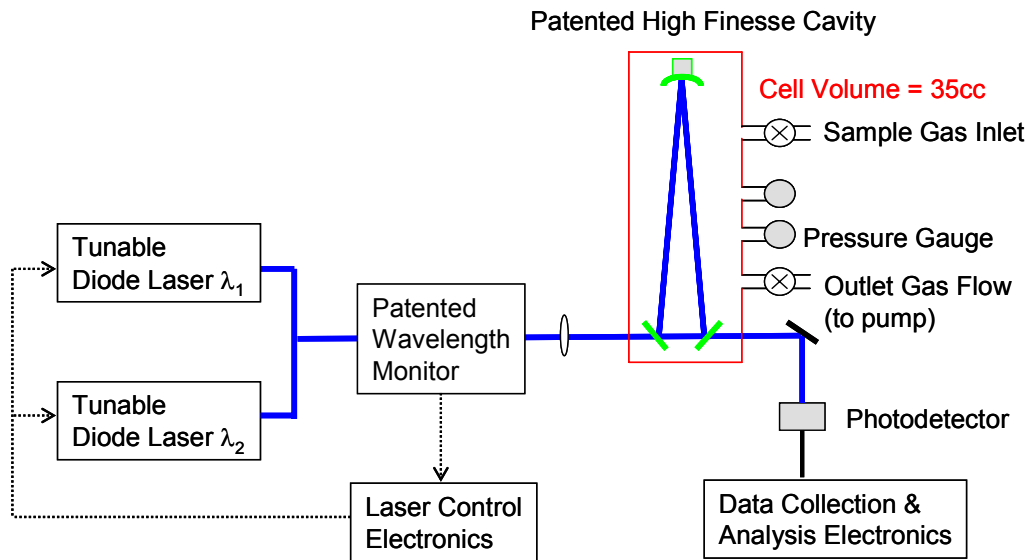


Figure 2.10 A block diagram of the CRDS analyzer: the wavelength monitor measures the wavelength of the light from a laser and gives a feedback to the laser control module, which in turn tunes the laser to output light with the exact wavelength (Crosson 2008).

The flight analyzer (Picarro Inc., CA, USA, model G1301-m) was developed on the basis of the previous model, G1301. Because the performance requirements of the flight analyzer and environmental conditions seen in flight are considerably more difficult to meet than those for the standard G1301 product, significant modifications were undertaken which resulted in new hardware, electronics, and software. These changes included a) adding an ambient pressure sensor and applying an ambient pressure correction to the high-precision wavelength monitor to ensure wavelength targets are met correctly under quickly changing ambient pressure; b) introducing three additional temperature sensors strategically located on the CRDS cavity and new firmware to enable correct operation of the analyzer's sample, pressure and temperature control systems; c) replacing the computer hard drive with solid-state drive; d) increasing the data acquisition rate of the analyzer from 0.2 Hz to 0.5 Hz.



## 2.4.2 System stability and linearity

### 2.4.2.1 System stability

To assess the stability of the measurements of the CRDS analyzer, CO<sub>2</sub> and CH<sub>4</sub> concentrations of the gas from an ambient standard tank have been continuously measured for about 24 hours. The time series are shown in Fig. 2.11, with the red curve showing the 5-minute average values. It can be easily observed that there is a slight drift in the CO<sub>2</sub> measurements for the first 10 hours, and the magnitude is estimated to be ~ 0.05 ppm, while no drift has been observed for CH<sub>4</sub> measurements. This small drift is probably due to the depletion of CO<sub>2</sub> in the pressure regulator, as is not seen in the CH<sub>4</sub> measurements.

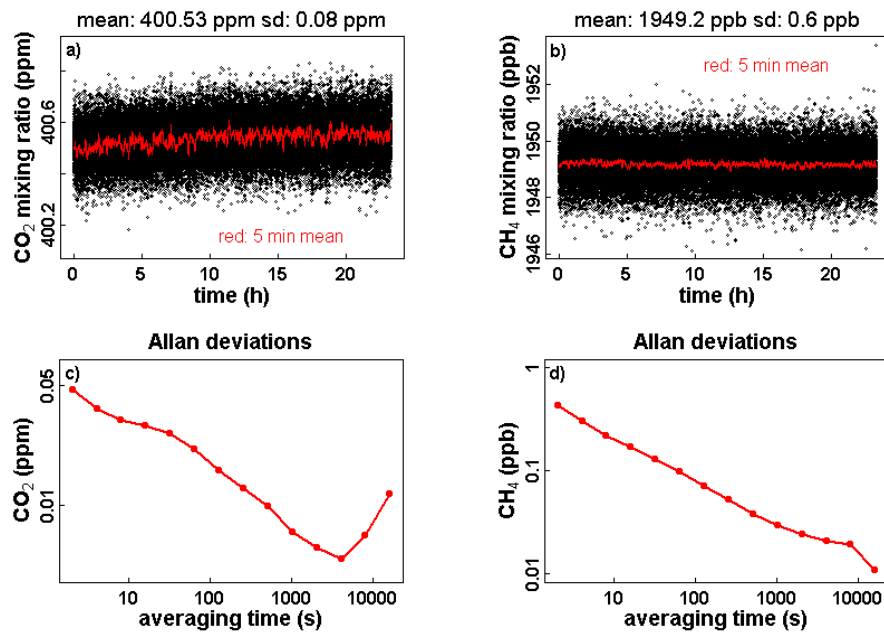


Figure 2.11. CO<sub>2</sub> and CH<sub>4</sub> concentration measurements of the gas from an ambient air standard by the CRDS analyzer in the laboratory: a) Time series of CO<sub>2</sub> concentrations; b) time series of CH<sub>4</sub> concentrations (red curves show the 5-minute average values); c) the Allan deviations of CO<sub>2</sub> measurements shown in a); d) the Allan deviations of CH<sub>4</sub> shown in b). Note that the Allan deviation plots are on log scales.

Allan deviations are computed to evaluate the ability of the CO<sub>2</sub> and CH<sub>4</sub> measurements for averaging, i.e. the maximum averaging time to remove random noise (see Fig. 2.11). The CO<sub>2</sub> measurement has a one sigma standard deviation of about 0.08 ppm for 2 second integration time, decreasing to 0.005 ppm when the averaging time is about two hours, while the CH<sub>4</sub> measurements has a one sigma standard deviation of about 0.6 ppb for a 2 second integration time, decreasing to 0.01 ppb for a four hour averaging time.

#### 2.4.2.2 Linearity

The CRDS analyzer was calibrated against four ambient air standards, which were prepared at the Max Planck Institute for Biogeochemistry in Jena (MPI-BGC), Germany, using dried and compressed air from outside the building. The calibration data have been linearly fitted for both CO<sub>2</sub> and CH<sub>4</sub> and are shown in Fig. 2.12, with the residuals shown on the right axes. The residuals from the CO<sub>2</sub> fit are much smaller than the uncertainties in the air standards, giving evidence that the CRDS analyzer is fully linear.

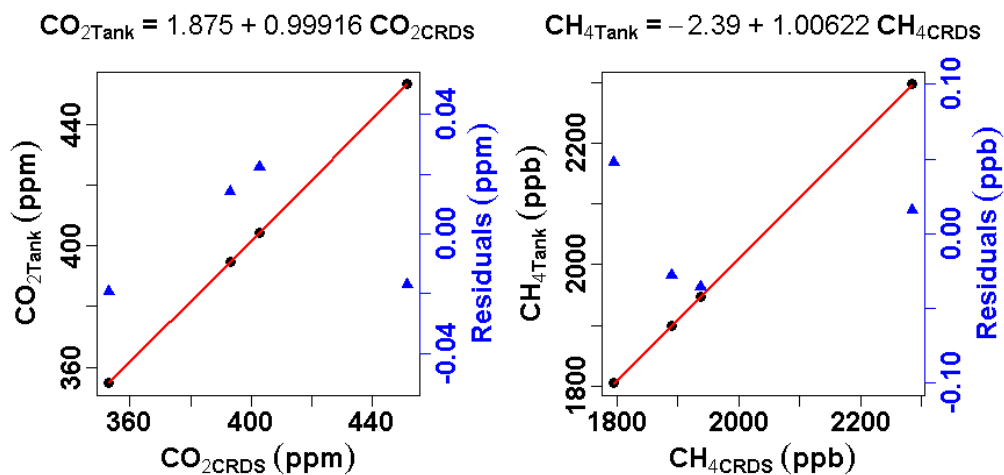


Figure 2.12 Calibrations of the measurements of CO<sub>2</sub> and CH<sub>4</sub> concentrations by the CRDS analyzer using four ambient air standards in the laboratory. The residuals are shown on the right axes of the two plots.

The excellent linearity implies that the CRDS analyzer can be calibrated with only two air standards: within the range of the calibrations, i.e. between the CO<sub>2</sub> concentrations of the two air standards, the uncertainties are smaller than 0.1 ppm; however, the uncertainties outside the range could be larger than 0.1 ppm.

### **2.4.3 Water corrections**

Atmospheric water vapor varies over small temporal and spatial scales on the magnitude of a few ppm in the stratosphere to a few percent in the troposphere. Mixing ratios of CO<sub>2</sub> and CH<sub>4</sub> are significantly affected by variations of water vapor, when using wet air mixing ratios (number of moles of the species divided by the number of moles of wet air). This impact of water vapor variations on the mixing ratios of CO<sub>2</sub> and CH<sub>4</sub> is called the dilution effect. To avoid this dilution effect, CO<sub>2</sub> and CH<sub>4</sub> mixing ratios are always reported as dry mole fractions. In order to ensure that the accuracy of measurements of CO<sub>2</sub> mixing ratios in dry air is better than 0.1 μmol/mol (ppm) according to the WMO recommendation (WMO, 2003) at the ambient level of ~ 400 ppm, the mixing ratio of water vapor in the sample air is either required to be removed to a level below 250 ppm or simultaneously measured at a precision of below 250 ppm to correct the water vapor dilution effect. The dilution effect for CH<sub>4</sub> is less significant than for CO<sub>2</sub>: to achieve the WMO recommended accuracy target of 2 ppb for CH<sub>4</sub> mixing ratio measurements at the ambient level of ~ 2000 ppb, the corresponding requirement for water vapor mixing ratios is only below 1000 ppm.

Furthermore, measurements using spectroscopy techniques are sensitive to water vapor variability via changes in the degree of pressure broadening of the spectroscopic lines

used to measure the mixing ratios of CO<sub>2</sub> and CH<sub>4</sub>. Here, the term ‘pressure broadening’ includes two effects: the Lorentzian line broadening caused by collisions between the analyte molecules, and Dicke line-narrowing of the Gaussian distribution of kinetic energy caused by energy-exchanging collisions. Both of these effects are proportional to pressure, but occur with different magnitudes depending on both the choice of the rovibrational absorption line of the analyte molecule as well as the composition of the background gas matrix; i.e., different background gas mixtures will lead to different broadening coefficients. In ambient air, the concentration of water vapor varies enough to cause measurable changes in the line-broadening parameters of the target analyte absorption lines. Other gases in the ambient atmosphere, like oxygen, nitrogen, argon, carbon dioxide, methane, and other trace constituents, do not vary enough (<~100 ppm) to cause measurable line broadening effects (though, in synthetic gas standards, the inert gases can present a problem, as discussed below).

These line-broadening effects do not affect the total area of the absorption line, but they do affect the peak height. The CRDS analyzer uses the absorption peak heights to calculate concentration; the peak height is used because of the higher noise present in the peak area measurement, due to systematic noise in the absorption baseline as well as noise in the measurement of the wavelength. Because the peak height is not constant for a given mixing ratio, variability in the line broadening thus leads to systematic errors in the reported mixing ratios. For the carbon dioxide and methane lines employed in the CRDS analyzer, the line-broadening effects, if not corrected, would lead to systematic errors of about 40% of the dilution effects.

In addition, the measurement of the water vapor mixing ratio by the CRDS analyzer is also subject to these line-broadening effects. In this case, it is self-broadening of the water vapor absorption line by water vapor itself, which leads to variations in the absorption line shape and thus a nonlinearity of the reported water vapor concentration as a function of the true water vapor concentration.

Finally, the absolute calibration of the water vapor reading is subject to significant (~1%) uncertainty, due to the difficulty in generating and delivering a known water vapor sample with high accuracy to the instrument.

If considered on an individual basis, each of these uncertainties (dilution, line-broadening, water vapor nonlinearity, and absolute water vapor calibration) could result in a substantial overall uncertainty in the dry gas mixing ratios for carbon dioxide and methane. However, we can take advantage of the fact that the CRDS analyzer provides highly *precise* readings of all three gases. By performing careful experiments, we can derive empirical expressions that directly relate the actual dry gas mixing ratios for carbon dioxide and methane to the *measured* water vapor readings. All the effects discussed above are then combined into a single expression which does not rely on careful understanding of each effect considered individually. In the section below, we assess whether, by using such an expression, the water vapor measurements provided on the CRDS analyzer are adequate for correcting the dilution and the pressure-broadening effects for carbon dioxide and methane.

#### 2.4.3.1 Experiments

In order to derive water correction functions for CO<sub>2</sub> and CH<sub>4</sub>, a series of experiments were carried out using the setup given in Fig. 2.13. Gas from a high-pressure tank containing ambient air was supplied to a humidifier or dew point generator (Li-Cor, Inc., Lincoln, NE, USA, model LI-610) after the air pressure was reduced to a level slightly above the ambient pressure using a combination of a high pressure regulator (Scott Specialty Gases, Plumsteadville, PA, USA, model 51-14D) and a needle valve. The ambient air tank was prepared at the Max Planck Institute for Biogeochemistry in Jena (MPI-BGC), Germany, using dried and compressed air from outside the building with CO<sub>2</sub> mixing ratios of ~ 400 ppm. The LI-610 humidifier could generate a moist air stream with a known set dew point ranging from 0 to 50 °C. After the gas was humidified, it was split into two paths, one with and the other without a chemical dryer (magnesium perchlorate). Carefully balancing of the flow and pressure ensures that there was no change in pressure in the chemical dryer while switching. This avoided the influence of magnesium perchlorate under conditions of changing pressure on CO<sub>2</sub> mixing ratios (Levin et al., 2002). A crossover valve that was made of two 3-way valves was located downstream of the dryer and was controlled by a data logger (Campbell Scientific, Inc., Logan, UT, USA, model CR23X) that selected dry or wet air to flow through the CRDS analyzer.

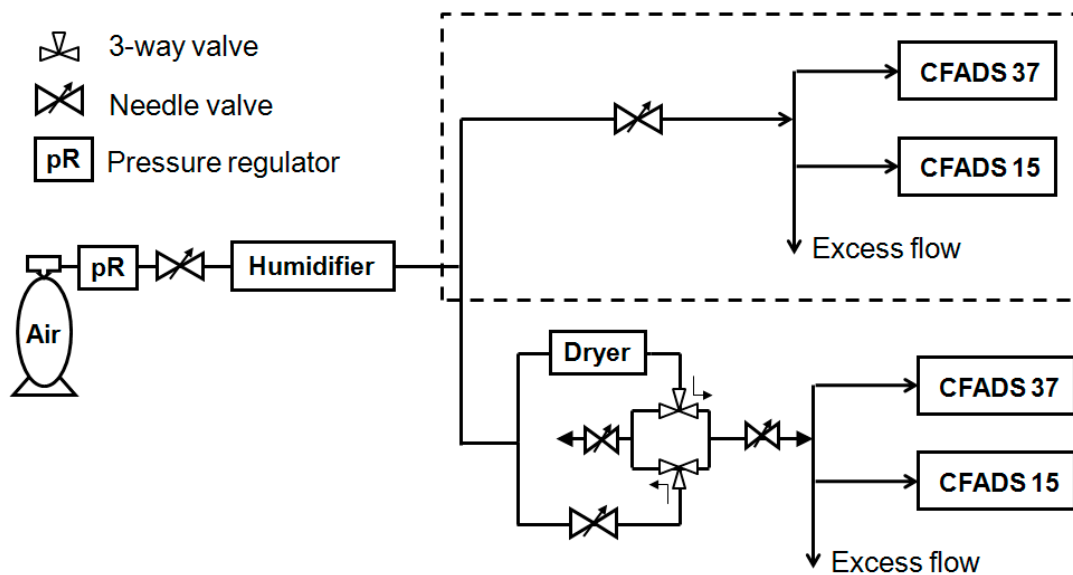


Figure 2.13 Schematic of the setup for experiments to derive water vapor correction functions (experiments were done separately to the two CRDS analyzers, i.e. CFADS 37 and CFADS 15 although they could be tested at one time) and correlate water vapor measurements of two individual CRDS analyzers (see inside the dashed lines)

Two CRDS analyzers were tested using this setup. The experiments for the flight version G1301-m were performed in a temperature-controlled room ( $\sim 38\text{ }^{\circ}\text{C}$ ) to prevent water vapor from condensing on the walls of tubing before flowing into the analyzer. The humidifier was sequentially set by the above described data logger to dew points  $0\text{ }^{\circ}\text{C}$ ,  $5\text{ }^{\circ}\text{C}$ ,  $10\text{ }^{\circ}\text{C}$ ,  $15\text{ }^{\circ}\text{C}$ ,  $20\text{ }^{\circ}\text{C}$ ,  $25\text{ }^{\circ}\text{C}$ ,  $30\text{ }^{\circ}\text{C}$  and  $35\text{ }^{\circ}\text{C}$ , corresponding to reported water vapor mixing ratios from 0.6 % to 6 %. The experiments were interrupted several times when the chemical dryer had to be changed.

The  $\text{CO}_2$  mixing ratio of the gas downstream of the humidifier often drifted linearly or exponentially due to solubility of  $\text{CO}_2$  in water in the humidifier. The drifts were removed before calculating the mixing ratio for both dry and wet cycles. The magnitude of the

drift for CO<sub>2</sub> is about several tenths of a ppm within an hour period. The CH<sub>4</sub> mixing ratio was calculated in the same way as the CO<sub>2</sub> mixing ratio, however, the drift of CH<sub>4</sub> concentration was insignificant since solubility of CH<sub>4</sub> in water is poor (see Fig. 2.14 a-b). The precision of the measurement of the water vapor mixing ratio of the CRDS analyzer is 23 ppm (1σ) at 4 % H<sub>2</sub>O level as measured by the CRDS analyzer. This corresponds to the maximum water vapor level expected in field experiments, excluding the cases of flying through cloud or rain. This is precise enough for correcting the dilution effect. In fact, both the dilution and the pressure-broadening effects can be compensated by the reported H<sub>2</sub>O mixing ratios. The effects of water vapor dilution as well as of pressure broadening for CO<sub>2</sub> and CH<sub>4</sub> can be represented by quadratic fits,

$$\frac{CO_{2wet}}{CO_{2dry}} = 1 + a \times H_2O + b \times H_2O^2 \quad (2.11)$$

$$\frac{CH_{4wet}}{CH_{4dry}} = 1 + c \times H_2O + d \times H_2O^2 \quad (2.12)$$

$a = -0.012000 / \%$ ,  $b = -0.000267 / \%^2$ ,  $c = -0.009823 / \%$ ,  $d = -0.000239 / \%^2$  (see Fig. 2.14 c-d). The residual errors of the fits were below 0.05 ppm for CO<sub>2</sub> and below 0.8 ppb for CH<sub>4</sub>.



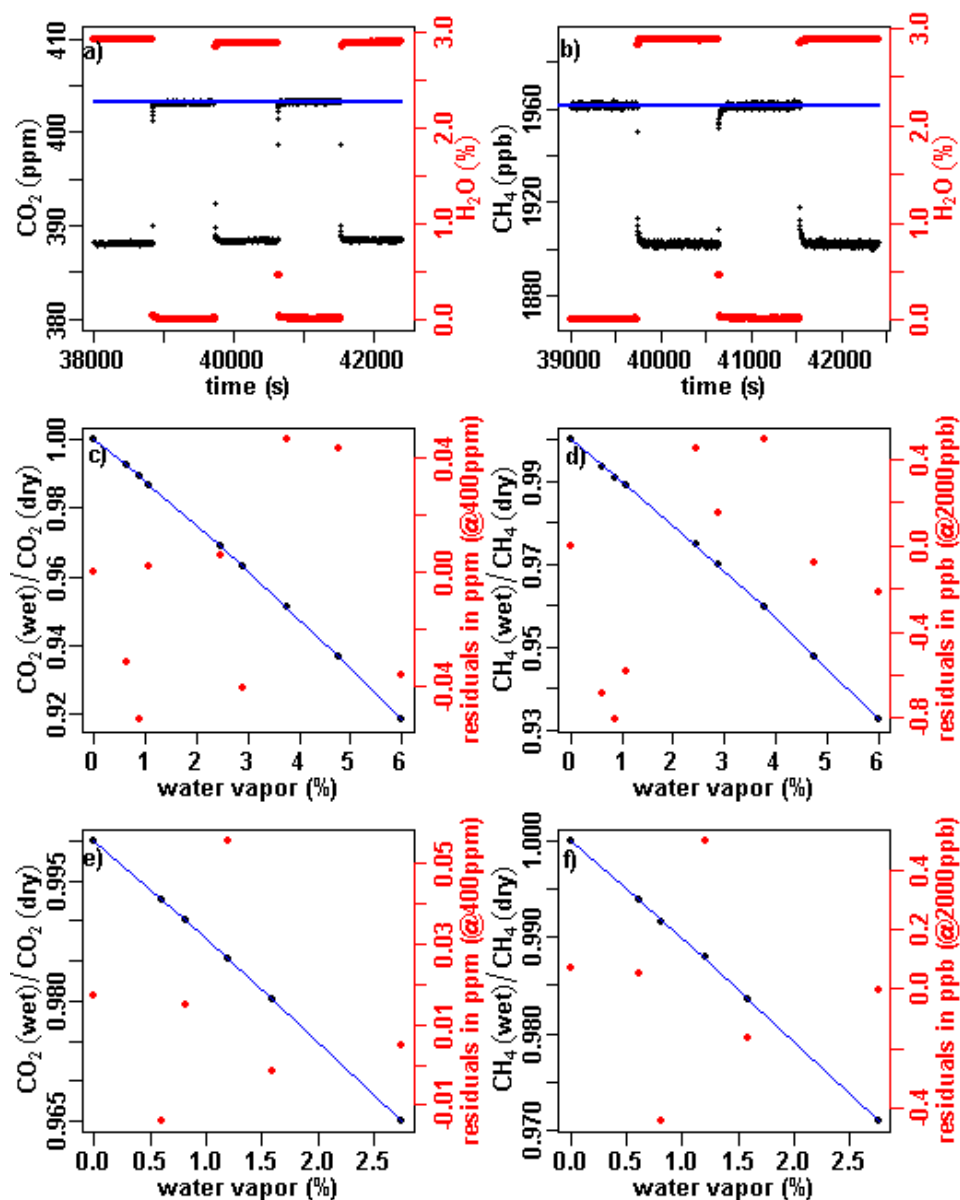


Figure 2.14. a) - b) Examples of the responses of CO<sub>2</sub> and CH<sub>4</sub> while switching between wet and dry air (see H<sub>2</sub>O on the right axis), and linear drift corrections (blue lines). On the time axis, the values are the seconds that have lapsed since the beginning of the day when the experiment was carried out c) - d) Quadratic fits of CO<sub>2</sub>wet/CO<sub>2</sub>dry and CH<sub>4</sub>wet/CH<sub>4</sub>dry vs. H<sub>2</sub>O mixing ratios. e)-f) Results from similar experiments performed with CFADS 15, with the curve showing the fit from experiments using CFADS 37. The red dots in a)-d) are residuals of corresponding fits and are read on the axis to the right. Note that a)-d) are results from experiments performed with CFADS 37 and e)-f) with CFADS 15.

#### 2.4.3.2 Transferability of the water correction functions

It is important to assess if the coefficients of the water correction functions derived from the laboratory experiment can be regarded as constants or whether a recalibration of these parameters via laboratory experiment is required. Rather than repeating the experiments at different times, e.g. after a year, we decided to repeat the experiment with a different analyzer.

We compared water correction functions of the flight CRDS analyzer (model G1301-m, serial designation CFADS 37) with those of one ground-based CRDS analyzer (model G1301, serial designation CFADS 15). We use CFADS 37 and CFADS 15 throughout the subsequent text to differentiate the two CRDS analyzers.

Experiments were performed for CFADS 15 using the same setup as for CFADS 37 (see Fig. 2.13); however, the reported water vapor mixing ratios ranged from 0.61 % to 2.76 %. To correlate the water vapor measurement of CFADS 15 with CFADS 37, step-changing wet air (from 1.09 % to 2.11 %) from the humidifier described above was provided to the two analyzers simultaneously. The water vapor measurements of the two analyzers are linearly correlated, with differences of reported water vapor mixing ratios from 36 ppm to 103 ppm for the range of reported water vapor mixing ratios from 1.09% to 2.11%. After correcting the water vapor measurements of CFADS 15 based on the water vapor measurements of CFADS 37, the water vapor correction functions from the experiments for CFADS 37 were applied to the experimental results of CFADS 15 (see Fig. 2.14 e-f). Comparable residual errors (below 0.05 ppm for CO<sub>2</sub> and below 0.5 ppb

for CH<sub>4</sub>) obtained from applying the same water correction functions to both experimental results for CFADS 37 and CFADS 15 proved that these correction functions are transferable from one instrument to another if the water vapor measurements are corrected to the same scale. The transferability between two individual analyzers suggests stability. However, the statistics from testing the two analyzers is still weak. Further water tests are ongoing with various analyzers.

Because the water vapor measurement by the analyzer is based on a single stable H<sub>2</sub>O spectroscopic feature which is spectrally close to the CH<sub>4</sub> spectral feature, we expect the measurement of the water vapor to exhibit the same highly stable performance over time that has been demonstrated on both CO<sub>2</sub> and CH<sub>4</sub>. Due to the difficulties in providing a known amount of water vapor, we cannot directly estimate the drift of water vapor accurately. However, we can use other stable gas measurements from the same analyzer (i.e. CO<sub>2</sub> and CH<sub>4</sub>) to estimate the drifts we might expect to see in H<sub>2</sub>O since the spectroscopy shares the same components (only the spectral lines are different). For CO<sub>2</sub> measurements, the observed peak-to-peak drift in an analyzer of the same type was 0.25 ppm over 170 days at a tall tower in Mead, Nebraska, USA (Crosson 2008), which corresponds to a drift of 1 part in 1600 of the 400 ppm CO<sub>2</sub> concentration. That would indicate that a 4 % water vapor concentration should drift by no more than 1 part in 1600 of 4 %, or 25 ppm. A drift of 25 ppm in the water vapor concentration translates to a drift of only ~0.01 ppm or ~0.05 ppb in the final reported CO<sub>2</sub> and CH<sub>4</sub> mixing ratios, respectively.

#### 2.4.4 Water calibrations

Although the CRDS analyzer offers highly precise readings of water vapor, it does not necessarily provide highly accurate measurements of water vapor concentrations. Actually, any measurements of relative humidity in the atmosphere are not sufficiently accurate to obtain results with uncertainties less than 0.1 %, and most commonly used expressions for the vapor pressure of ice are within 1 % of each other for measurements between -103 °C and 0 °C (Murphy et al., 2005).

An identical CRDS flight analyzer (model G1301-m, serial designation CFADS 30) has been calibrated using the basic components of the setup shown in Fig. 2.13. The dew point was measured by a dew point mirror (Dewmet, Michell instruments Ltd., UK) using a Swagelok T-junction that was located close to the inlet of the analyzer. The pressure of the gas, i.e. ambient pressure, was monitored by a high-precision pressure indicator (DPI 740, Druck limited, Leicester, UK). Gas from tank air was humidified using the Li-Cor 610 humidifier. The dew point was set from 0 to 24 °C at 2 °C intervals, corresponding to the CRDS-reported water vapor mixing ratios from 0.77 % to 3.55 %. The vapor pressure was derived from the dew point values based on Wexler's formulation that has been converted from the temperature scale of ITS-68 to ITS-90 (Wexler 1976; Hardy 1998):

$$\ln e_s = \sum_{i=0}^6 g_i T^{i-2} + g_7 \ln T \quad (2.13)$$

where  $e_s$  is the saturation vapor pressure in Pa and T is the temperature in Kelvin and the coefficients for the ITS-90 scale are

$$g_0 = -2.8365744 \times 10^3$$

$$g_1 = -6.028076559 \times 10^3$$

$$g_2 = 1.954263612 \times 10^1$$

$$g_3 = -2.737830188 \times 10^{-2}$$

$$g_4 = 1.6261698 \times 10^{-5}$$

$$g_5 = 7.0229056 \times 10^{-10}$$

$$g_6 = -1.8680009 \times 10^{-13}$$

$$g_7 = 2.7150305$$

A quadratic curve was employed to fit the reported water vapor values (%) from the dew point mirror against the values (%) from the CRDS analyzer (see Fig. 2.15). The corresponding equation is

$$H_2O_{Dewmet} = 0.0292 + 0.7719 \times H_2O_{CRDS} + 0.0197 \times H_2O_{CRDS}^2 \quad (2.14)$$

The residuals of the fit are shown on the right axis of the plot in Fig. 2.15. Although these residuals are all smaller than 15 ppm, the actual uncertainties for the calibration could be larger due to the uncertainty of the dew point values provided by the dew point mirror. The accuracy of the dew point temperature measurements is  $\pm 0.2$  °C, which corresponds to uncertainties of water vapor mixing ratios from 93 ppm to 365 ppm, i.e. 1.3% of the values, for the tested water vapor range. Note that Eq. 2.14 is only valid for the range from 0.77 % to 3.55 % of the CRDS-reported water vapor mixing ratios.

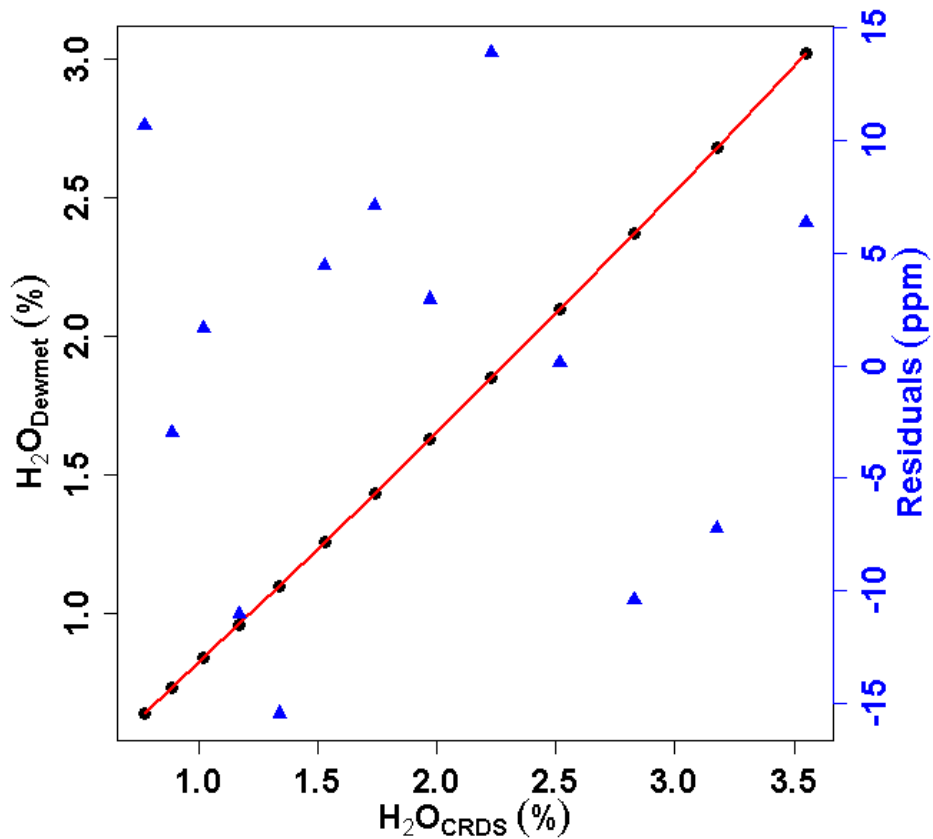


Figure 2.15 Calibration of a CRDS analyzer against a dew point mirror for the range from 0.77 % to 3.55 % (reported water vapor mixing ratios from the CRDS analyzer). The red curve is a quadratic fit of the data. The residuals of the fit are shown on the right axis. Note that the actual uncertainties may be larger than these residuals due to the uncertainties in the dew point temperature measurements from the dew point mirror.

#### 2.4.5 Performance under simulated flight conditions

Several laboratory tests are foreseen: 1) Changing the instrument ambient temperature and pressure to determine their influences; 2) changing the inlet pressure to discover the range of operating inlet pressures; 3) Adding mechanical vibrations to see the impact. The first test has been made in the laboratory and is presented below in this section, while

the second and third tests have been performed in the company where the analyzer is manufactured.

A flight analyzer needs to be able to deal with the environmental temperature and pressure variations on board aircraft. As part of the work necessary to verify CRDS analyzer performance before deployment in the field, temperature and pressure variations that typically occurred during flight were applied. To this end the CRDS analyzer was placed in an environmental chamber (Siemens AG, Chemnitz, Germany, type CH3030) in an attempt to replicate the conditions found aboard a research aircraft (Bandeirante EMB 110) with a non-pressurized cabin flying over the Amazon rain forest in Brazil, or aboard a commercial airliner (Airbus A340) as envisioned for the IAGOS operation. The inlet pressure is made identical to the chamber pressure by the introduction of an excess flow by a Swagelok Union Tee. The analyzer measured mixing ratios of CO<sub>2</sub> and CH<sub>4</sub> standard gases during the whole test period. The test results are shown in Fig. 2.16. The instrument ambient pressure ranged from 1000 mbar down to 640 mbar and temperature ranged from 44 °C down to 26 °C covering the expected range of cabin conditions typically found on board both aircraft. Note that the instrument aboard the Airbus A340 usually experiences ambient pressure down to 250 mbar, which was not tested during this experiment.

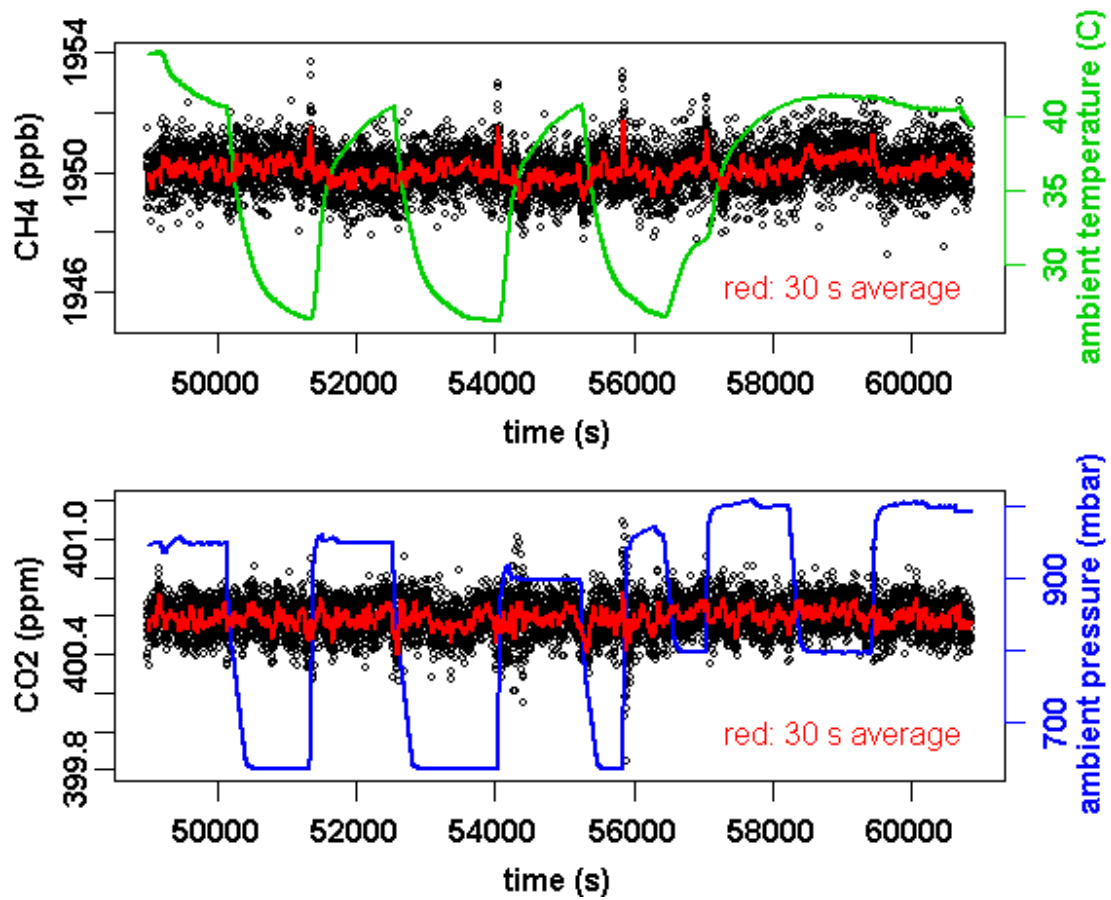


Figure 2.16 CO<sub>2</sub> and CH<sub>4</sub> measurements under simulated flight conditions

The measurements during laboratory pressure and temperature tests showed insignificant difference in the mean values and slightly larger noise under simulated flight conditions ( $400.59 \pm 0.09$  ppm for CO<sub>2</sub> and  $1950.07 \pm 0.68$  ppb for CH<sub>4</sub>) compared to normal ambient conditions ( $400.59 \pm 0.07$  ppm for CO<sub>2</sub> and  $1950.15 \pm 0.64$  ppb for CH<sub>4</sub>). The maximum pressure change rate was actually 5 times larger than what was expected to happen aboard a research aircraft or aboard a commercial aircraft due to the operational constraints of the environmental chamber. A few spikes at around 51500, 54000, 55900, 57000 s for CH<sub>4</sub> and at around 54200 and 55900 s for CO<sub>2</sub> have been observed. Note that these happened when the pressure values were increasing. The reason was that the



pressure change rates during the pressure increasing period were much larger than expected pressure change rates during flight. Therefore, these spikes will not emerge during a real flight. The performance of the CRDS analyzer under simulated flight conditions implies high stability during later flight measurements.

## **2.5 Summary and outlook**

This chapter first provided an overview of the techniques for measuring atmospheric CO<sub>2</sub> and CH<sub>4</sub> concentrations. Within the IAGOS project, two analyzers that are based on the NDIR technique and the CRDS technique respectively have been investigated. Laboratory tests characterizing the NDIR analyzer show that it lacks stability and requires considerable maintenance during flight and thus is not a feasible option for deployment on board a commercial airliner. After assessment of the associated calibration system as well as system performance under changing pressures in an environmental chamber, this NDIR analyzer has been modified and deployed on a rental aircraft to perform regular profiling in eastern Poland.

The second analyzer, based on CRDS, has been chosen as the candidate for deployment on a commercial airliner within IAGOS because of its high stability and potentials for low maintenance that have been revealed from laboratory stability tests under normal and controlled conditions of changing environmental temperature and pressure. Quadratic water corrections for the CRDS analyzer have been derived from laboratory experiments and proved to be adequate in correcting the dilution and pressure-broadening effects for both CO<sub>2</sub> and CH<sub>4</sub> during a BARCA (Balanço Atmosférico Regional de Carbono na Amazônia) campaign (details will be described in Chapter 3). Furthermore, the water

vapor measurements by the CRDS analyzer have been calibrated against a dew point mirror, providing the ability to monitor water vapor at the same time.

The CRDS technique is fully adequate to provide measurements of CO<sub>2</sub> and CH<sub>4</sub> at precisions that meet the corresponding WMO recommendations. It also has the ability to provide high precision measurements of other trace gases or isotope ratios (Brand et al., 2009; Zare et al., 2009). However, this technique is preferably implemented to detect weak absorptions of trace gases or isotopes with low concentrations in the atmosphere in the mid-infrared region, where many trace gases have their strongest ro-vibrational transitions. Further, broadband cavity-enhanced spectroscopy techniques have the potential to obtain higher sensitivities and thus be able to detect extremely weak absorptions of trace gases in the atmosphere (Gohle et al., 2007; Thorpe et al., 2008; Bernhardt et al., 2009).

## 2.6 References

- Allan, D. W. (1987). "Time and Frequency (Time-Domain) Characterization, Estimation, and Prediction of Precision Clocks and Oscillators." Ieee Transactions on Ultrasonics Ferroelectrics and Frequency Control **34**(6): 647-654.
- Anderson, B. E., G. L. Gregory, J. E. Collins, G. W. Sachse, T. J. Conway and G. P. Whiting (1996). "Airborne observations of spatial and temporal variability of tropospheric carbon dioxide." Journal of Geophysical Research-Atmospheres **101**(D1): 1985-1997.
- Barnes, J. A., A. R. Chi, L. S. Cutler, D. J. Healey, D. B. Leeson, T. E. McGunigal, J. A. Mullen, W. L. Smith, R. L. Sydnor, R. F. C. Vessot and G. M. R. Winkler (1971). "Characterization of Frequency Stability." IEEE Transactions on Instrumentation and Measurement **IM-20**(No. 2): 105-120.

- Bernhardt, B., A. Ozawa, P. Jacquet, M. Jacquy, Y. Kobayashi, T. Udem, R. Holzwarth, G. Guelachvili, T. W. Hansch and N. Picque (2009). "Cavity-enhanced dual-comb spectroscopy." Nature Photonics **4**(1): 55-57.
- Bischof, W. (1962). "Variations in Concentration of Carbon Dioxide in the Free Atmosphere." Tellus **14**(1): 87-90.
- Boering, K. A., B. C. Daube, S. C. Wofsy, M. Loewenstein, J. R. Podolske and E. R. Keim (1994). "Tracer-Tracer Relationships and Lower Stratospheric Dynamics - CO<sub>2</sub> and N<sub>2</sub>O Correlations During Spade." Geophysical Research Letters **21**(23): 2567-2570.
- Brand, W. A., H. Geilmann, E. R. Crosson and C. W. Rella (2009). "Cavity ring-down spectroscopy versus high-temperature conversion isotope ratio mass spectrometry; a case study on delta H-2 and delta O-18 of pure water samples and alcohol/water mixtures." Rapid Communications in Mass Spectrometry **23**(12): 1879-1884.
- Bray, J. R. (1959). "An Analysis of the Possible Recent Change in Atmospheric Carbon Dioxide Concentration." Tellus **11**(2): 220-230.
- Briesmeister, R. A., G. W. Read, K. C. Kim and J. R. Fitzpatrick (1984). "Long Path-Length Temperature-Controlled Absorption Cell for Spectroscopic Studies of Radioactive Compounds." Applied Spectroscopy **38**(1): 35-38.
- Callendar, G. S. (1938). "The artificial production of carbon dioxide and its influence on temperature." Quarterly Journal of the Royal Meteorological Society **64**: 223-240.
- Callendar, G. S. (1940). "Variations of the amount of carbon dioxide in different air currents." Quarterly Journal of the Royal Meteorological Society **66**: 395-400.
- Callendar, G. S. (1958). "On the Amount of Carbon Dioxide in the Atmosphere." Tellus **10**(2): 243-248.
- Crosson, E. R. (2008). "A cavity ring-down analyzer for measuring atmospheric levels of methane, carbon dioxide, and water vapor." Applied Physics B-Lasers and Optics **92**(3): 403-408.
- Da Costa, G. and L. P. Steele (1999). "Cape Grim's new low flow, high precision, in situ CO<sub>2</sub> analyser system - Development status and results from four month's operation at Aspendale." WMO 10. Meeting of Experts on CO<sub>2</sub> Measurements. Stockholm, Sweden.
- Daube, B. C., K. A. Boering, A. E. Andrews and S. C. Wofsy (2002). "A high-precision fast-response airborne CO<sub>2</sub> analyzer for in situ sampling from the surface to the middle stratosphere." Journal of Atmospheric and Oceanic Technology **19**(10): 1532-1543.

- Engeln, R., G. Berden, R. Peeters and G. Meijer (1998). "Cavity enhanced absorption and cavity enhanced magnetic rotation spectroscopy." Review of Scientific Instruments **69**(11): 3763-3769.
- Fonselius, S., F. Koroleff and K. Buch (1955). "Microdetermination of CO<sub>2</sub> in the Air, with Current Data for Scandinavia." Tellus **7**(2): 258-271.
- Frankenberg, C., P. Bergamaschi, A. Butz, S. Houweling, J. F. Meirink, J. Notholt, A. K. Petersen, H. Schrijver, T. Warneke and I. Aben (2008). "Tropical methane emissions: A revised view from SCIAMACHY onboard ENVISAT." Geophysical Research Letters **35**(15).
- Gohle, C., B. Stein, A. Schliesser, T. Udem and T. W. Hansch (2007). "Frequency comb Vernier spectroscopy for broadband, high-resolution, high-sensitivity absorption and dispersion spectra." Phys Rev Lett **99**(26): 263902.
- Hardy, B. (1998). "ITS-90 FORMULATIONS FOR VAPOR PRESSURE, FROSTPOINT TEMPERATURE, DEWPOINT TEMPERATURE, AND ENHANCEMENT FACTORS IN THE RANGE -100 TO +100 C." The Proceedings of the Third International Symposium on Humidity & Moisture, Tedington, London, England.
- Houweling, S., T. Rockmann, I. Aben, F. Keppler, M. Krol, J. F. Meirink, E. J. Dlugokencky and C. Frankenberg (2006). "Atmospheric constraints on global emissions of methane from plants." Geophysical Research Letters **33**(15).
- Jimenez, R., S. Herndon, J. H. Shorter, D. D. Nelson, J. B. McManus and M. S. Zahniser (2005). "Atmospheric trace gas measurements using a dual quantum-cascade laser n-dd-infrared absorption spectrometer." Novel In-Plane Semiconductor Lasers IV **5738**: 318-331.
- Keeling, C. D., R. B. Bacastow, A. E. Bainbridge, C. A. Ekdahl, P. R. Guenther, L. S. Waterman and J. F. S. Chin (1976). "Atmospheric Carbon-Dioxide Variations at Mauna-Loa Observatory, Hawaii." Tellus **28**(6): 538-551.
- Keeling, C. D., T. B. Harris and E. M. Wilkins (1968). "Concentration of Atmospheric Carbon Dioxide at 500 and 700 Millibars." Journal of Geophysical Research **73**(14): 4511-&.
- Keppler, F., J. T. G. Hamilton, M. Brass and T. Rockmann (2006). "Methane emissions from terrestrial plants under aerobic conditions." Nature **439**(7073): 187-191.
- Langenfelds, R. L., M. V. van der Schoot, R. J. Francey, L. P. Steele, M. Schmidt and H. Mukai (2005). "Modification of air standard composition by diffusive and surface processes." Journal of Geophysical Research-Atmospheres **110**(D13).

- Levin, I., P. Ciais, R. Langenfelds, M. Schmidt, M. Ramonet, K. Sidorov, N. Tchebakova, M. Gloor, M. Heimann, E. D. Schulze, N. N. Vygodskaya, O. Shibistova and J. Lloyd (2002). "Three years of trace gas observations over the EuroSiberian domain derived from aircraft sampling - a concerted action." Tellus Series B-Chemical and Physical Meteorology **54**(5): 696-712.
- Machida, T., K. Kita, Y. Kondo, D. Blake, S. Kawakami, G. Inoue and T. Ogawa (2002). "Vertical and meridional distributions of the atmospheric CO<sub>2</sub> mixing ratio between northern midlatitudes and southern subtropics." Journal of Geophysical Research-Atmospheres **108**(D3).
- Machida, T., H. Matsueda, Y. Sawa, Y. Nakagawa, K. Hirotani, N. Kondo, K. Goto, T. Nakazawa, K. Ishikawa and T. Ogawa (2008). "Worldwide Measurements of Atmospheric CO<sub>2</sub> and Other Trace Gas Species Using Commercial Airlines." Journal of Atmospheric and Oceanic Technology **25**(10): 1744-1754.
- Mazurenka, M., A. J. Orr-Ewing, R. Peverall and G. A. D. Ritchie (2005). Cavity ring-down and cavity enhanced spectroscopy using diode lasers. Annual Reports on the Progress of Chemistry, Vol 101, Section C, Physical Chemistry. Cambridge, Royal Soc Chemistry. **101**: 100-142.
- McManus, J. B., J. H. Shorter, D. D. Nelson, M. S. Zahniser, D. E. Glenn and R. M. McGovern (2008). "Pulsed quantum cascade laser instrument with compact design for rapid, high sensitivity measurements of trace gases in air." Applied Physics B-Lasers and Optics **92**(3): 387-392.
- Miller, J. B., L. V. Gatti, M. T. S. d'Amelio, A. M. Crotwell, E. J. Dlugokencky, P. Bakwin, P. Artaxo and P. P. Tans (2007). "Airborne measurements indicate large methane emissions from the eastern Amazon basin." Geophysical Research Letters **34**(10).
- Murphy, D. M. and T. Koop (2005). "Review of the vapour pressures of ice and supercooled water for atmospheric applications." Quarterly Journal of the Royal Meteorological Society **131**(608): 1539-1565.
- Nelson, D. D., B. McManus, S. Urbanski, S. Herndon and M. S. Zahniser (2004). "High precision measurements of atmospheric nitrous oxide and methane using thermoelectrically cooled mid-infrared quantum cascade lasers and detectors." Spectrochimica Acta Part a-Molecular and Biomolecular Spectroscopy **60**(14): 3325-3335.
- O'Keefe, A. (1998). "Integrated cavity output analysis of ultra-weak absorption." Chemical Physics Letters **293**(5-6): 331-336.

- Okeefe, A. and D. A. G. Deacon (1988). "Cavity Ring-Down Optical Spectrometer for Absorption-Measurements Using Pulsed Laser Sources." Review of Scientific Instruments **59**(12): 2544-2551.
- Pales, J. C. and C. D. Keeling (1965). "Concentration of Atmospheric Carbon Dioxide in Hawaii." Journal of Geophysical Research **70**(24): 6053-&.
- Revelle, R. and H. E. Suess (1957). "Carbon Dioxide Exchange between Atmosphere and Ocean and the Question of an Increase of Atmospheric CO<sub>2</sub> During the Past Decades." Tellus **9**(1): 18-27.
- Romanini, D. and K. K. Lehmann (1993). "Ring-Down Cavity Absorption-Spectroscopy of the Very Weak Hcn Overtone Bands with 6, 7, and 8 Stretching Quanta." Journal of Chemical Physics **99**(9): 6287-6301.
- Rothman, L. S., I. E. Gordon, A. Barbe, D. C. Benner, P. E. Bernath, M. Birk, V. Boudon, L. R. Brown, A. Campargue, J. P. Champion, K. Chance, L. H. Coudert, V. Dana, V. M. Devi, S. Fally, J. M. Flaud, R. R. Gamache, A. Goldman, D. Jacquemart, I. Kleiner, N. Lacome, W. J. Lafferty, J. Y. Mandin, S. T. Massie, S. N. Mikhailenko, C. E. Miller, N. Moazzen-Ahmadi, O. V. Naumenko, A. V. Nikitin, J. Orphal, V. I. Perevalov, A. Perrin, A. Predoi-Cross, C. P. Rinsland, M. Rotger, M. Simeckova, M. A. H. Smith, K. Sung, S. A. Tashkun, J. Tennyson, R. A. Toth, A. C. Vandaele and J. Vander Auwera (2009). "The HITRAN 2008 molecular spectroscopic database." Journal of Quantitative Spectroscopy & Radiative Transfer **110**(9-10): 533-572.
- Rothman, L. S., D. Jacquemart, A. Barbe, D. C. Benner, M. Birk, L. R. Brown, M. R. Carleer, C. Chackerian, K. Chance, L. H. Coudert, V. Dana, V. M. Devi, J. M. Flaud, R. R. Gamache, A. Goldman, J. M. Hartmann, K. W. Jucks, A. G. Maki, J. Y. Mandin, S. T. Massie, J. Orphal, A. Perrin, C. P. Rinsland, M. A. H. Smith, J. Tennyson, R. N. Tolchenov, R. A. Toth, J. Vander Auwera, P. Varanasi and G. Wagner (2005). "The HITRAN 2004 molecular spectroscopic database." Journal of Quantitative Spectroscopy & Radiative Transfer **96**(2): 139-204.
- Shashkov, A., K. Higuchi and D. Chan (2007). "Aircraft vertical profiling of variation of CO<sub>2</sub> over a Canadian Boreal Forest Site: a role of advection in the changes in the atmospheric boundary layer CO<sub>2</sub> content." Tellus Series B-Chemical and Physical Meteorology **59**(2): 234-243.
- Sturm, P., M. Leuenberger, C. Sirignano, R. E. M. Neubert, H. A. J. Meijer, R. Langenfelds, W. A. Brand and Y. Tohjima (2004). "Permeation of atmospheric gases through polymer O-rings used in flasks for air sampling." Journal of Geophysical Research-Atmospheres **109**(D4).

- Thorpe, M. J. and J. Ye (2008). "Cavity-enhanced direct frequency comb spectroscopy." Applied Physics B-Lasers and Optics **91**(3-4): 397-414.
- Tohjima, Y., H. Mukai, T. Machida, Y. Nojiri and M. Gloor (2005). "First measurements of the latitudinal atmospheric O-2 and CO<sub>2</sub> distributions across the western Pacific." Geophysical Research Letters **32**(17).
- Tuzson, B., J. Mohn, M. J. Zeeman, R. A. Werner, W. Eugster, M. S. Zahniser, D. D. Nelson, J. B. McManus and L. Emmenegger (2008). "High precision and continuous field measurements of delta C-13 and delta O-18 in carbon dioxide with a cryogen-free QCLAS." Applied Physics B-Lasers and Optics **92**(3): 451-458.
- Wexler, A. (1976). "Vapor Pressure Formulation for Water in Range 0 to 100°C." Journal of Research of the National Bureau of Standards - A. Physics and Chemistry **80A**: 755-785.
- White, J. U. (1942). "Long optical paths of large aperture." Journal of the Optical Society of America **32**(5): 285-288.
- Winderlich, J. (2007). "Entwicklung und Test eines Probenahme- und Kalibriersystems für einen kontinuierlich messenden Hochpräzisions-CO<sub>2</sub>-Analysator zum Einsatz in kommerziellen Flugzeugen." Diploma thesis.
- Zare, R. N., D. S. Kuramoto, C. Haase, S. M. Tan, E. R. Crosson and N. M. R. Saad (2009). "High-precision optical measurements of C-13/C-12 isotope ratios in organic compounds at natural abundance." Proceedings of the National Academy of Sciences of the United States of America **106**(27): 10928-10932.
- Zhao, C. L. and P. P. Tans (2006). "Estimating uncertainty of the WMO mole fraction scale for carbon dioxide in air." Journal of Geophysical Research-Atmospheres **111**(D8).

## **Chapter 3 Validation of in situ airborne CO<sub>2</sub>/CH<sub>4</sub> measurements**

### **3.1 Introduction**

Improvement of the precision and accuracy of CO<sub>2</sub> concentration measurements played an important role in confirming the long term increasing trend of atmospheric CO<sub>2</sub> concentrations (Callendar 1938; Pales et al., 1965). Furthermore, atmospheric CO<sub>2</sub> and CH<sub>4</sub> need to be measured precisely and accurately in order to obtain full confidence in the data quality and comparability between measurements made by different laboratories, resolve regional carbon budgets, and for surveillance of the mitigation of CO<sub>2</sub> emissions in the future (Gurney et al., 2002; WMO 2003). Since variability of CO<sub>2</sub> and CH<sub>4</sub> concentrations at high altitude, e.g., in the free troposphere and stratosphere, are rather small compared to those in the planetary boundary layer (PBL) (Bischof 1962; Machida et al., 2008), even higher precision and accuracy are required to be accomplished so that changes in the concentrations could be observed.

According to the definition of International Vocabulary of Metrology (VIM3 2007), the measurement precision describes the closeness of agreement of replicate measurements on the same or similar objects under specified conditions, while the measurement accuracy, on the other hand, represents the closeness of agreement of measurements with their true values. The precision provides an assessment of how well a measurement could be repeated or reproduced over a relatively short period, which, in the case of airborne measurements, can be affected by several factors: detector noise, impacts of temperature



and pressure variations, mechanical vibrations or shocks. Regarding the accuracy, the true values could be determined by absolute measurement techniques, such as the manometric method for determining the mole fraction scale for CO<sub>2</sub> in air (Zhao et al., 2006) and the gravimetric technique to define the mole fraction scale for CH<sub>4</sub> in dry air (Dlugokencky et al., 2005). The accuracy of measurements by an instrument suffers from the instability of the response of the instrument, and is usually secured by calibrations using air standards for the case of CO<sub>2</sub> or CH<sub>4</sub> concentration measurements. Besides, the gas handling could have a significant impact on the accuracy of measurements in an analyzer system, particularly for CO<sub>2</sub> (Langenfelds et al., 2005). Note that the precision and accuracy of measurements should be given along with a time scale since they might be improved by averaging individual measurements over a period of time to remove random noise.

Although the accuracy of measurements can be monitored or adjusted by calibrations, uncertainties may remain in the measurements due to the instability of the analyzer between calibration points as well as the potential uncertainties in the calibration system. Therefore, comparisons between independent measurements are commonly employed to confirm the accuracy. The argument is that if two independent measurements agree to a high degree, the chances of both instruments giving wrong measurements are low. Measurements of the same species of gases by two different instruments could be too expensive for most of the cases and thus are not always practically implemented. Flask analyses of air samples that are collected simultaneously with in situ measurements are able to provide data for multiple species and are suggested to be widely implemented

(Tans et al., 1996). Comparison of in situ with flask measurements is then an important method to confirm the accuracy of measurements.

Comparison of aircraft in situ measurements with ground based station or tower measurements provides some sense of confidence with respect to the accuracy of the measurements (Gurk et al., 2008; Martins et al., 2009); however, the comparison may be influenced by the spatial or temporal variations, i.e., the representativeness of the measurements (to be discussed in Chapter 4), and thus can usually not be regarded as strict quality control for high-accuracy measurements.

This chapter focuses on validation of routine airborne CO<sub>2</sub> measurements near a monitoring site and airborne CO<sub>2</sub>/CH<sub>4</sub> measurements made by a CRDS analyzer that has been chosen for future deployment on board a commercial airliner (Chen et al., 2010). The rest of the chapter is organized as follows: Chapter 3.2 describes the method for comparison of in situ with flask measurements; validation of airborne CO<sub>2</sub> measurements using the NDIR technique and airborne CO<sub>2</sub>/CH<sub>4</sub> measurements using the CRDS technique are presented in Chapter 3.3 and 3.4; Chapter 3.5 concludes the chapter.

### **3.2 Methodology for comparison of in situ with flask measurements**

Laboratory analyses of flask samples collected in the field allow for measurement of a large number of trace gases and isotopes, but also provide an important quality check for in situ measurements made at ground-based stations or aboard aircraft. In situ measurements are normally reported at a relatively high frequency, e.g., 1 s, while the flask samples are usually taken over a short period of time, e.g., 30 ~ 60 s. The analysis

results of the flask samples provide one value for each species of gas from each air sample. Therefore, in order to compare in situ measurements with the discrete flask measurements that are integrated over a short period of time, a weighting function is required for integrating the in situ measurements. In this section, the flask sampler is introduced at first and then development of weighting functions for comparisons between in situ continuous and flask measurements is presented for single and paired flasks.

### 3.2.1 Flask sampler

A flask sampler, which was developed by the Max Planck Institute for Biogeochemistry in Jena (MPI-BGC), Germany, has been used in flight to collect air samples during several aircraft campaigns as well as regular profiling in northeastern Poland since 2002. The flask sampler was designed to take paired flasks that are in serial connection (see Fig. 3.1). It can be easily configured to take a single flask by replacing the second flask with a simple decobon (or decoron/synflex) tube.

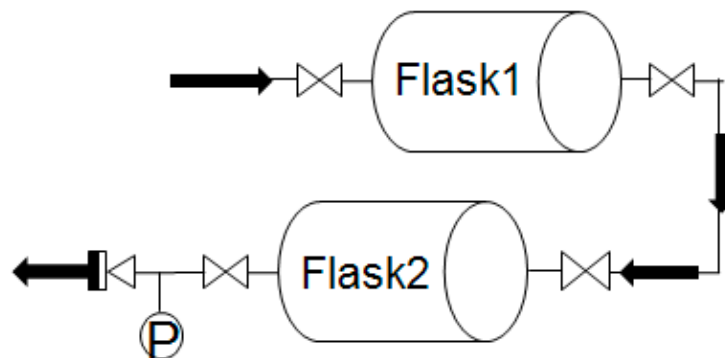


Figure 3.1. The flow diagram of the flask sampler. The capital letter of P in a circle indicates a flask pressure sensor.

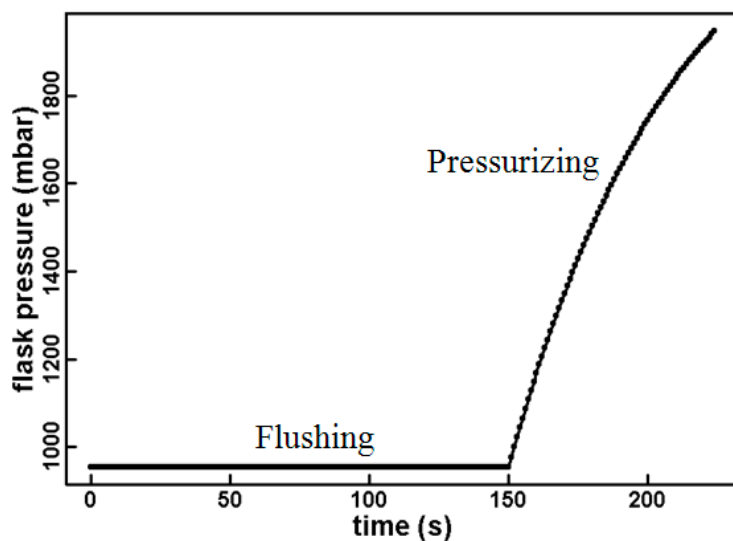


Figure 3.2. The logged flask pressure during a flask sampling process, which consists of two processes: flushing and pressurizing. The time scale is relative to the time when the flushing starts.

In order to synchronize the flask sampling time with the in situ measurements and obtain additional information for flask comparison, a pressure sensor has been implemented downstream of the second flask (see Fig. 3.2) to measure the flask pressure during flask sampling.

During flight, an operator collects air samples with the flask sampler. The flasks contain conditioning air (dried ambient air from outside the building of MPI-BGC) before air samples are taken. The sample air is dried with a chemical dryer (magnesium perchlorate) before entering the flasks. The flask sampling consists of two steps: flushing and pressurizing. During flushing, ambient air is pumped through the flasks at a flow rate of  $\sim 3.5$  L/min. Assuming that the difference of  $\text{CO}_2$  mixing ratios of conditioning air and ambient air is less than 100 ppm and that the final pressure in the flask is one bar above ambient, the required flushing time for a single flask and paired flasks (specifically the

downstream one) according to Eqs. A.4 and A.22 (see Appendix A for the details) is  $\sim 2$  and  $\sim 2.5$  minutes so that 99.9 % of the conditioning air has been exchanged; this corresponds to a potential bias of  $< 0.05$  ppm on the  $\text{CO}_2$  concentrations of the air samples. The pressurizing process starts when a shut-off valve located downstream the flask(s) is closed and then air accumulates in the flask(s) with a decreasing flow rate. The flask sampling is stopped when a 3-way valve is switched to bypass the air flow. After closing the flask(s), the flask sampling is completed.

The flasks are analyzed by an automated gas chromatographic system in the GasLab at MPI-BGC, Germany. The measurement of  $\text{CO}_2$  and  $\text{CH}_4$  mixing ratios is traceable to WMO  $\text{CO}_2$  and  $\text{CH}_4$  scales (Dlugokencky et al., 2005; Zhao et al., 2006). Therefore, comparisons of in situ data with flask  $\text{CO}_2$  and  $\text{CH}_4$  measurements allow for one approach to assess the accuracy of the in situ measurements.

### **3.2.2 Method for comparison of in situ with single flask measurements**

Briefly, the weighting function is derived based on the assumption that the air entering a flask mixes instantaneously with the existing air in the flask. This perfect mixing has been shown in laboratory tests, which provide a step change in  $\text{CO}_2$  mixing ratio to the flask and measure the air leaving the flask with a continuous measurement system (Licor 6262). For the case of one single flask, the flask sampling process consists of two steps: flushing and pressurizing (see Fig. 3.3). During the flushing process, air flows into and out of the flask at the same flow rate,  $f_0$ ; at the time when the pressurizing period starts, the fraction of the air (entering the flask at time  $t$ ) remaining in the flask, is  $c(t)$ . During

the pressurizing process, air flows into the flask at a decreasing flow rate of  $f(t)$ , and the flask is pressurized until the flask sampling is completed.

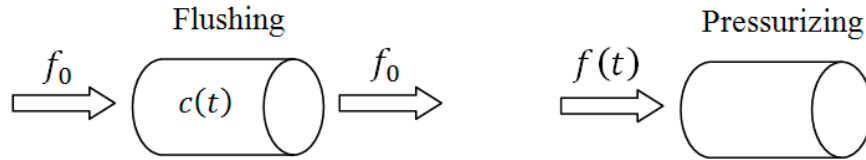


Figure 3.3. The schematic of the flask sampling for a single flask, which consists of two processes: flushing, air flowing into the flask is instantaneously mixed and then flows out of the flask at the same flow rate  $f_0$ ; pressurizing, air flows into the flask with decreasing flow rate  $f(t)$  until the flask sampling is completed.

The weighting function for integrating in situ measurements to compare with the analysis result of one single flask can be described as (see Appendix A1):

$$W(t) = \begin{cases} W_1(t) = \frac{p_s}{p_e} \cdot \frac{1}{\tau} e^{-(t_s-t)/\tau} / (1 - e^{-t_s/\tau}), \tau = \frac{p_s}{\frac{dp(t_s)}{dt}} & 0 < t < t_s \\ W_2(t) = \frac{1}{p_e} \cdot \frac{dp(t)}{dt} & t_s \leq t < t_e \end{cases} \quad (3.1)$$

Here  $p_s$  and  $p_e$  are the flask pressures when the flask pressurizing process starts ( $t = t_s$ ) and ends ( $t = t_e$ );  $p(t)$  is the flask pressure at time  $t$ . The weighting function for integrating in situ measurements to compare with the analysis result of one single flask is shown in Fig. 3.4. The weighting function is normalized to 1 and has its maximum value at the time when the pressurizing starts  $t = t_s$ .

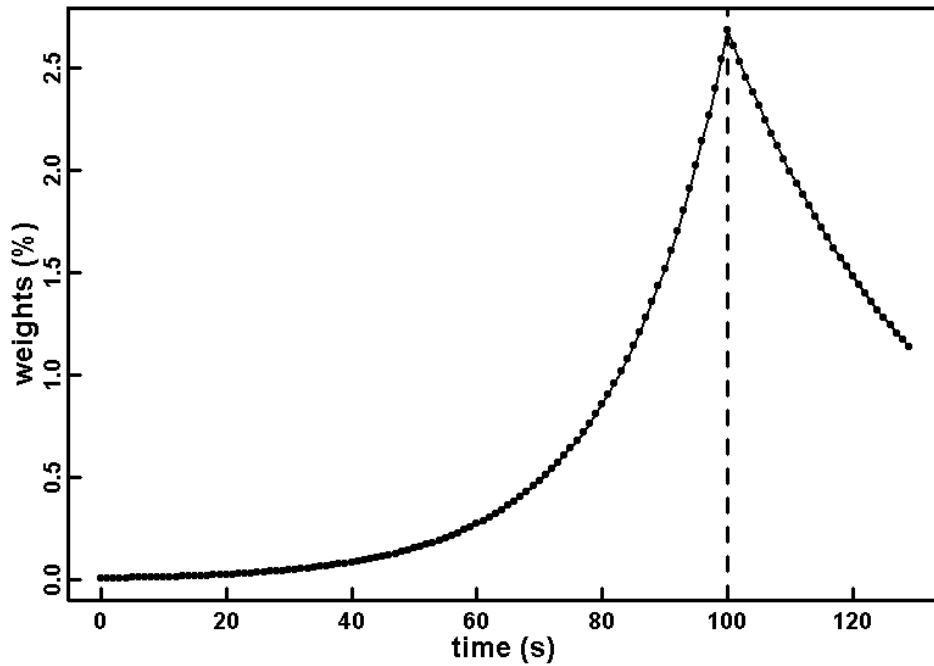


Figure 3.4. The weighting function for integrating in situ measurements to compare with the analysis result of one single flask, plotted as a function of time. The time scale is relative to the starting time of flask flushing and the weights are given in percent. The dashed line denotes the time when the pressurizing period starts. The weighting function is calculated based on the recorded and smoothed flask pressure during flight.

### 3.2.3 Method for comparison of in situ with paired flask measurements

For the case of paired flasks, the flask sampling process consists of two processes as well: flushing and pressurizing (see Fig. 3.5). During flushing, air flows into and out of the upstream and then the downstream flask at a flow rate of  $f_0$ ; at the time when the pressurizing period starts, the fraction of the air (entering the upstream flask at the time  $t$ ) remaining in the upstream flask is  $c_1(t)$ , while the fraction of the air remaining in the downstream flask is  $c_2(t)$ . During the pressurizing period, air flows into the upstream flask at a decreasing flow rate of  $f(t)$ , but out of the flask at the flow rate of  $f(t)/2$ ; at the time when the pressurizing period ends, the fraction of the pressurizing air (entering

the upstream flask at the time  $t$ ) remaining in the upstream flask is  $c'_1(t)$ , while the fraction of the air coming into the downstream flask is  $c'_2(t)$ . It is important to note that a fraction of flushing air flows from the upstream flask into the downstream flask during the pressurizing period.

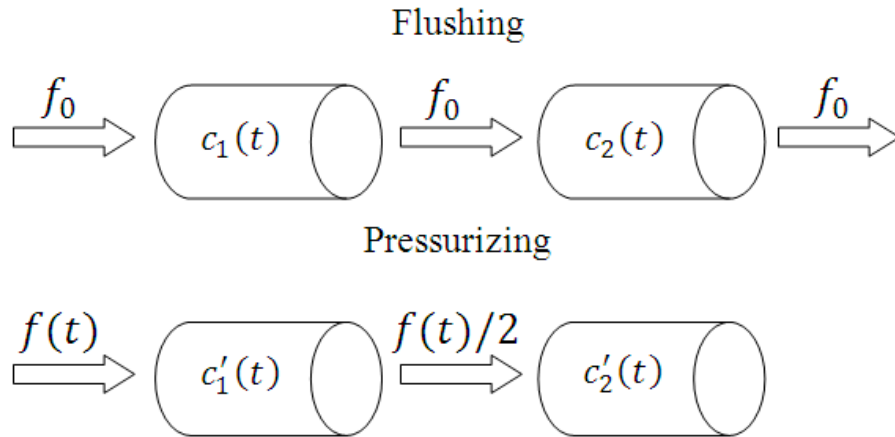


Figure 3.5. The schematic of flask sampling process for the case of pair flasks, which consists of two steps: flushing and pressurizing. During the flushing, air flows into and out of the first flask at a flow rate of  $f_0$  (the air is fully mixed inside the first flask) and then flows into and out of the second flask at the same flow rate of  $f_0$ . During the pressurizing process, air flows into the first flask at a varying flow rate of  $f(t)$ , but out of the first flask at the flow rate of  $f(t)/2$ ; air with the flow rate of  $f(t)/2$  pressurizes the second flask.

The weighting function for integrating in situ measurements to compare with the analysis result of the upstream flask of a pair can be described as (see Appendix A2):

$$W_1(t) = \begin{cases} W_{1f}(t) = \left(\frac{p_s}{p_e}\right)^2 \cdot \frac{1}{\tau} e^{-(t_s-t)/\tau} / (1 - e^{-t_s/\tau}), \tau = \frac{p_s}{2 \cdot \frac{dp(t_s)}{dt}} & 0 < t < t_s \\ W_{1p}(t) = \frac{2 \cdot p(t)}{p_e^2} \cdot \frac{dp(t)}{dt} & t_s \leq t < t_e \end{cases} \quad (3.2)$$

The weighting function for integrating in situ measurements to compare with the analysis result of the downstream flask of a pair can be described as (see Appendix A2):



$$W_2(t) = \begin{cases} W_{2f}(t) = \left(2 \cdot \frac{p_s}{p_e} - \left(\frac{p_s}{p_e}\right)^2\right) \cdot \frac{\left(\frac{t_s-t}{\tau} \cdot e^{-(t_s-t)/\tau} + \left(1 - \frac{p_s}{p_e}\right) \cdot e^{-(t_s-t)/\tau}\right)}{\left(2 - \frac{p_s}{p_e}\right) \cdot \tau \cdot (1 - e^{-t_s/\tau}) - t_s \cdot e^{-t_s/\tau}}, \tau = \frac{p_s}{2 \cdot \frac{dp(t_s)}{dt}} & 0 < t < t_s \\ W_{2p}(t) = \frac{2}{p_e} \cdot \frac{dp(t)}{dt} \cdot \left(1 - \frac{p(t)}{p_e}\right) & t_s \leq t < t_e \end{cases} \quad (3.3)$$

where  $p_s$  and  $p_e$  are the flask pressures (both flask have the same pressure) when the flask pressurizing process starts and ends;  $p(t)$  is the flask pressure at time  $t$ . The weighting functions for integrating in situ measurements to compare with pair-flask analysis results are shown in Fig. 3.6.

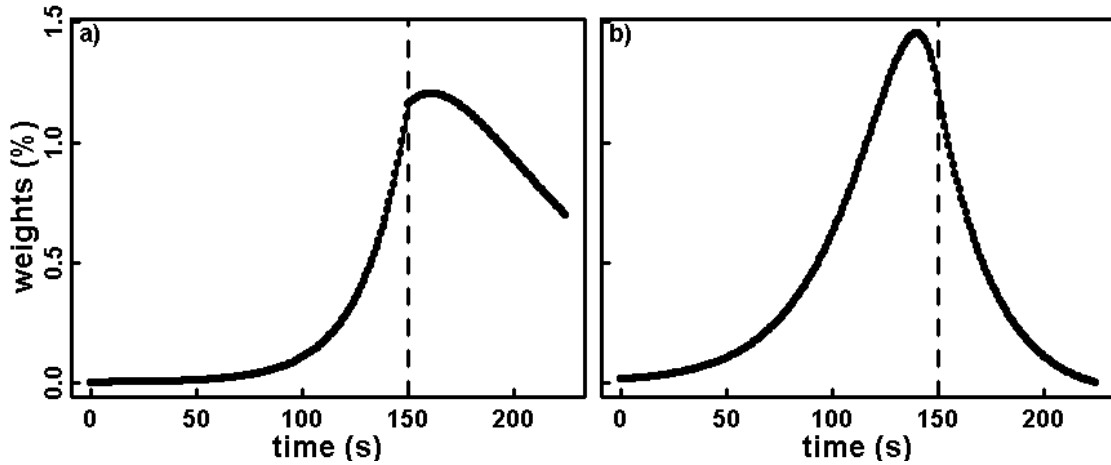


Figure 3.6. Weighting functions for integrating in situ measurements to compare with pair-flask measurements, plotted as a function of time: a. for the upstream flask and b. for the downstream flask, respectively. The time scale is relative to the starting time of flask flushing and the weights are given in percent. The dashed lines denote the time when the pressurizing period starts. The weighting functions are calculated based on the recorded and smoothed flask pressure.

Here an example of using the weighting functions for integrating in situ measurements of CO<sub>2</sub> concentrations and then comparing with flask measurements is given. The measurements of CO<sub>2</sub> concentrations made by the NDIR analyzer and from analyses of flask samples from a flight on August 20, 2008 in Bialystok, Poland, are shown in Fig.

3.7. The flask CO<sub>2</sub> measurements are shown as blue (upstream) and green (downstream) dots. At the time of about 49300 s, CO<sub>2</sub> flask values from the paired flasks vary by a few ppm, even though they were taken simultaneously.

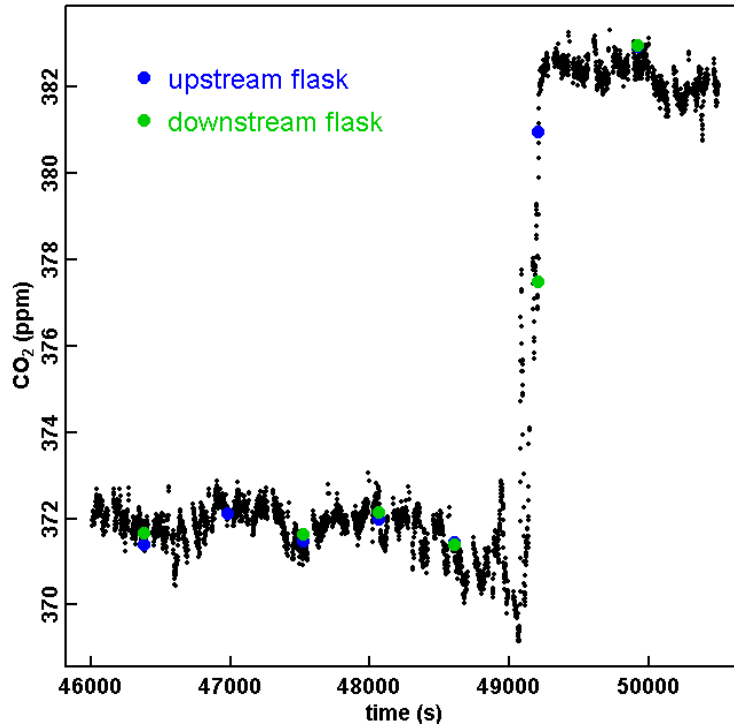


Figure 3.7. An example of in situ measurements of CO<sub>2</sub> concentrations, plotted as a function of time, with flask CO<sub>2</sub> concentrations shown in blue (upstream) and green (downstream). The values on the x-axis are seconds since midnight of the day when the measurements were made.

The differences of integrated in situ and flask CO<sub>2</sub> concentrations using constant (1/120 over a 120 seconds window) and the above-described weighting coefficients are shown in Fig. 3.8. The improved agreements between averaged in situ and flask CO<sub>2</sub> concentrations when using the weighting functions show that the atmospheric CO<sub>2</sub> variability can be accounted for when using the proper weighting functions for integrating in situ CO<sub>2</sub> values.

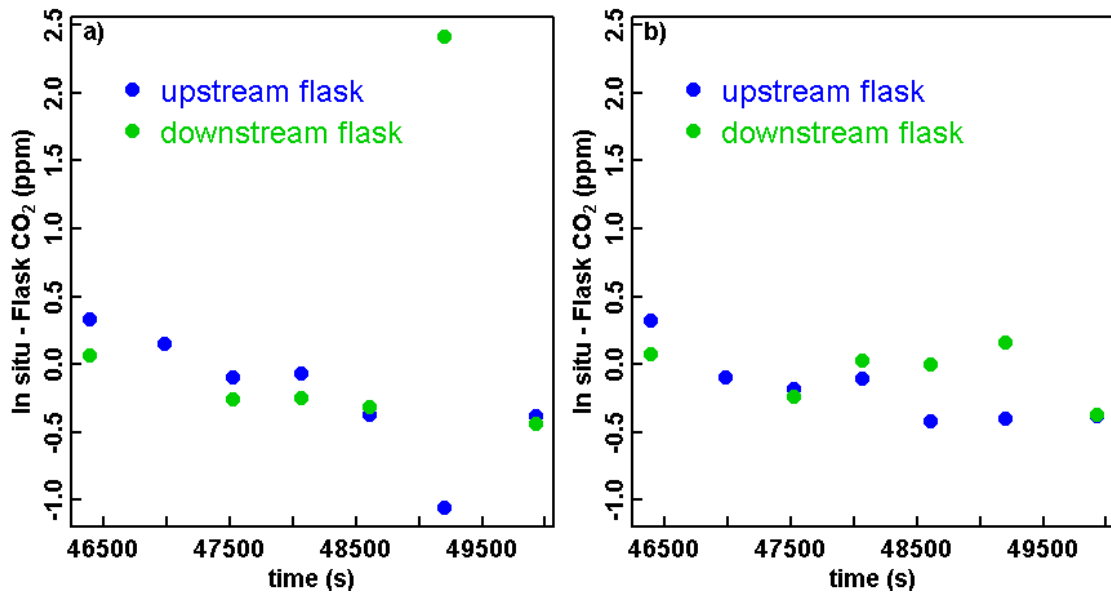


Figure 3.8. Comparison of in situ with flask CO<sub>2</sub> measurements for the flight on August 20, 2008. a. the in situ values are obtained from integrating in situ continuous CO<sub>2</sub> measurements with constant coefficients in a 120-s window; b. the in situ values from integrating in situ continuous CO<sub>2</sub> measurements with the weighting functions described above.

### 3.3 Validation of regular airborne in situ CO<sub>2</sub> profiles over Bialystok

#### Tall Tower

In situ measurements of CO<sub>2</sub> concentrations have been made regularly since 2002 by a modified Li-Cor-6251 system (Lloyd et al., 2002) on a rental aircraft (Wilga, type PZL-104) near the Bialystok tall tower (Lat 53°14'N, Long 23°01'E) in northeastern Poland (Katrynski 2006). In April, 2008, a test flight using the NDIR analyzer described in Chapter 2 was made on board the Wilga aircraft in Bialystok, and then since August, 2008, the Li-Cor system has been replaced by the NDIR analyzer with the aim of improving the measurement accuracy and obtaining an additional profile within the same amount of available flight hours for each flight. In the new flight protocol, each flight

consists of two profiles: one ascending profile near the BIK tower and another descending profile that is located on the other side of the city of Bialystok, and is 20 km away. During ascent, seven pairs of flasks are taken at altitudes of 100m, 300m, 500m, 1000m, 1500m, 2000m, and 2500m above ground level; during the period from August to December, 2008, only three pairs of flasks are taken at altitudes of 100m, 1500m, and 2500m for two flights out of every three flights in order to save use of flasks and flight hours. The flasks are later analyzed by the GasLab at MPI-BGC for CO<sub>2</sub>, CH<sub>4</sub>, CO, N<sub>2</sub>O, SF<sub>6</sub> and H<sub>2</sub> concentrations. The aircraft climbs at about 1.5 m/s and descends at about 5.5 m/s, corresponding to vertical resolutions of 7 m and 26 m, respectively. Figure 9 shows an example of a measurement flight on August 20, 2008.

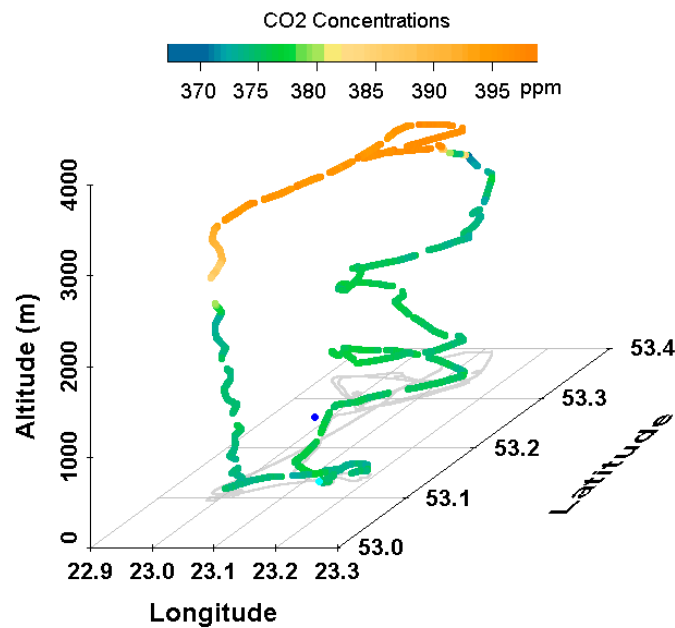


Figure 3.9. One example of CO<sub>2</sub> concentration measurements from a flight on August 20, 2008, shown in 3D, with the flight track colored by CO<sub>2</sub> concentrations. The grey lines show the projected flight track on the ground level and the blue dot indicates the location of the tower.

### **3.3.1 Comparison of in situ with flask CO<sub>2</sub> measurements**

From April 2008 to August 2009, 32 flights using the NDIR analyzer have been made, with 329 flasks taken during flights (a single flask was taken during the test flight on April 28, 2008). Comparison of in situ with flask CO<sub>2</sub> measurement using the above-described weighting functions has the ability to reveal potential problems in either of the two independent measurements. Among these flasks, analyses of 14 flasks failed, mainly due to low pressure in the flasks. In addition, 29 flasks from 3 flights were contaminated (28 flasks were most likely contaminated by a leak during flask sampling and one was contaminated during storage). Regarding the in situ CO<sub>2</sub> measurements, 4 flights suffer from significant leaks and another 4 flights are suspected to have been influenced by a small leak. Besides this, there are 10 flights during which the drying efficiency of the chemical dryer was insufficient. The quality assurance of both in situ and flask measurement of CO<sub>2</sub> concentrations has been listed in Table 1.

Table 1. Quality assurance of in situ and flask measurements of CO<sub>2</sub> concentrations during flights over BIK towers for the period from April 2008 to August 2009

Date (yyyymmdd)	In situ CO <sub>2</sub> *	Flask CO <sub>2</sub>	Date (yyyymmdd)	In situ CO <sub>2</sub>	Flask CO <sub>2</sub>
20080428	good	Good	20081107	leak	good
20080807	good	Good	20081111	leak	good
20080812	good	Good	20081116	leak	good
20080816	good	Good	20081122	leak	good
20080820	good	Good	20081201	leak	good
20080825	good	Good	20090102	good	good
20080830	water	Good	20090331	good	good
20080903	water	Good	20090408	good	good
20080909	water	Good	20090427	good	good
20080914	water	Good	20090515	good	good
20080925	water	Good	20090529	water	good
20080930	water	Good	20090615	water	good
20081012	good	Good	20090629	water	good
20081018	leak	Good	20090707	water	good
20081025	leak	Good	20090718	not clear	All contaminated
20081029	leak	One contaminated	20090810	not clear	All Contaminated

\*“good” means good agreement between in situ and flask measurements of CO<sub>2</sub> concentrations; “water” means the in situ measurements of CO<sub>2</sub> concentrations are corrected using the flask measurements and the water vapor measurements; “leak” means there is a leak in the CO<sub>2</sub> analyzer system; “not clear” because of no comparison due to the contamination of flasks

A direct comparison of integrated in situ CO<sub>2</sub> values with 216 flasks from 22 flights (excluding 8 flights with potential leak and 2 flights with contaminated flasks) is shown in Fig. 3.10a. The mean difference of in situ and flask CO<sub>2</sub> values is -0.43 ppm with a standard deviation of 0.89 ppm; however, clear drift can be observed during two periods: flask No. 60 ~ 90, and > 180, corresponding to 6 flights from 20080830 to 20080930, and 4 flights from 20090529 to 20090707. The discrepancy for these flights are caused by a

decrease in drying efficiency of the chemical dryer and could be compensated when the in situ measurements CO<sub>2</sub> concentrations are properly corrected using the flask values and water vapor measurements, see the next section.

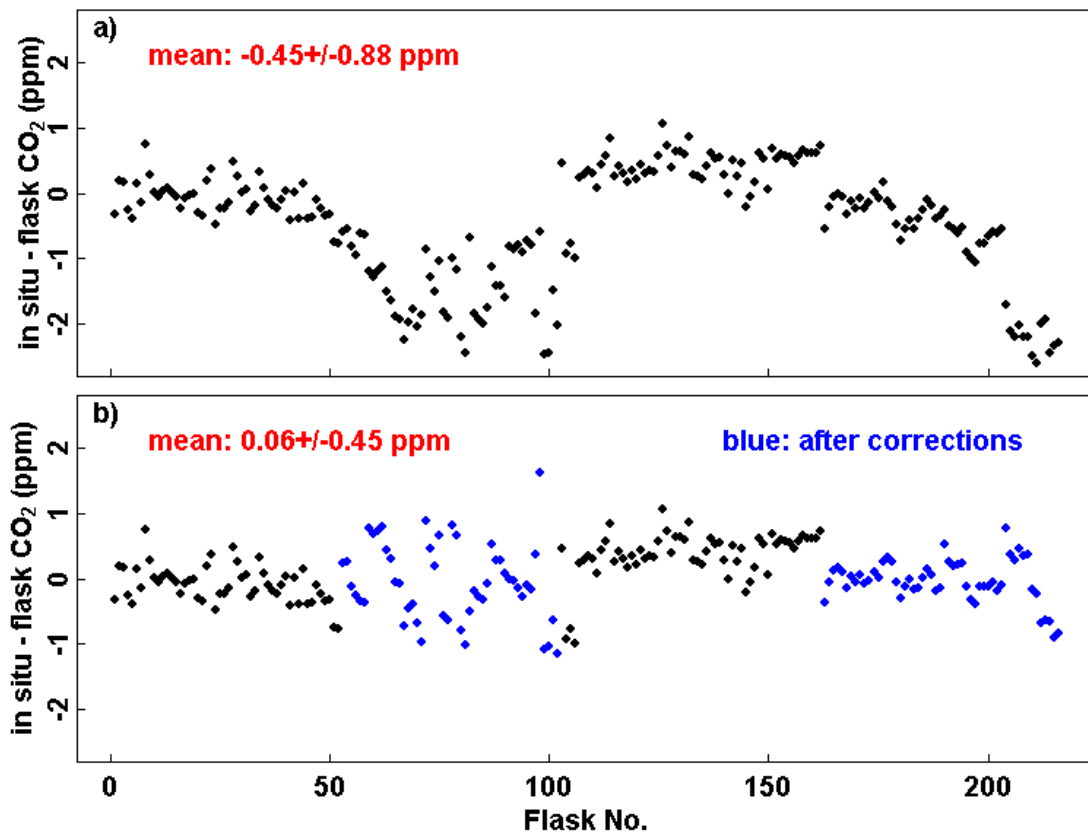


Figure 3.10. Comparison of in situ with flask CO<sub>2</sub> concentration measurements over Bialystok Tall Tower for 216 flasks from 22 flights between April 2008 and July 2009. The figure shows the differences between averaged in situ and flask CO<sub>2</sub> concentrations for a. blind comparison and for b. after correcting the insufficient drying effect for 104 flasks from 10 flights. The averaged values and standard deviations of the differences in a) and b) are shown in the plot in red.

### 3.3.2 Corrections for the bias due to insufficient drying

The biases in the differences of in situ and flask CO<sub>2</sub> during two periods in Fig. 3.10a are caused by residual water vapor in the air after the chemical dryer. This effect can be clearly seen when the differences are plotted per flight as a function of ambient water

vapor mixing ratios (see Fig. 3.11). The hypothesis is that the water vapor mixing ratios after the chemical dryer are proportional to the ambient values and the drying efficiency of the chemical dryer decreases with time (inter-flight). Linear regression models are fitted per flight using the least squares approach for the differences between in situ and flask CO<sub>2</sub> as a function of water vapor mixing ratios. One slope value is obtained from each linear regression, which is used to correct the in situ measurements of CO<sub>2</sub> concentrations based on the measured ambient water vapor mixing ratios. The comparison of integrated in situ and flask CO<sub>2</sub> after correcting the water vapor effects for the 10 flights is shown in Fig. 3.10b, with the corrected values shown in blue. The mean difference of in situ and flask CO<sub>2</sub> values reduces to 0.08 ppm with a standard deviation of 0.45 ppm.



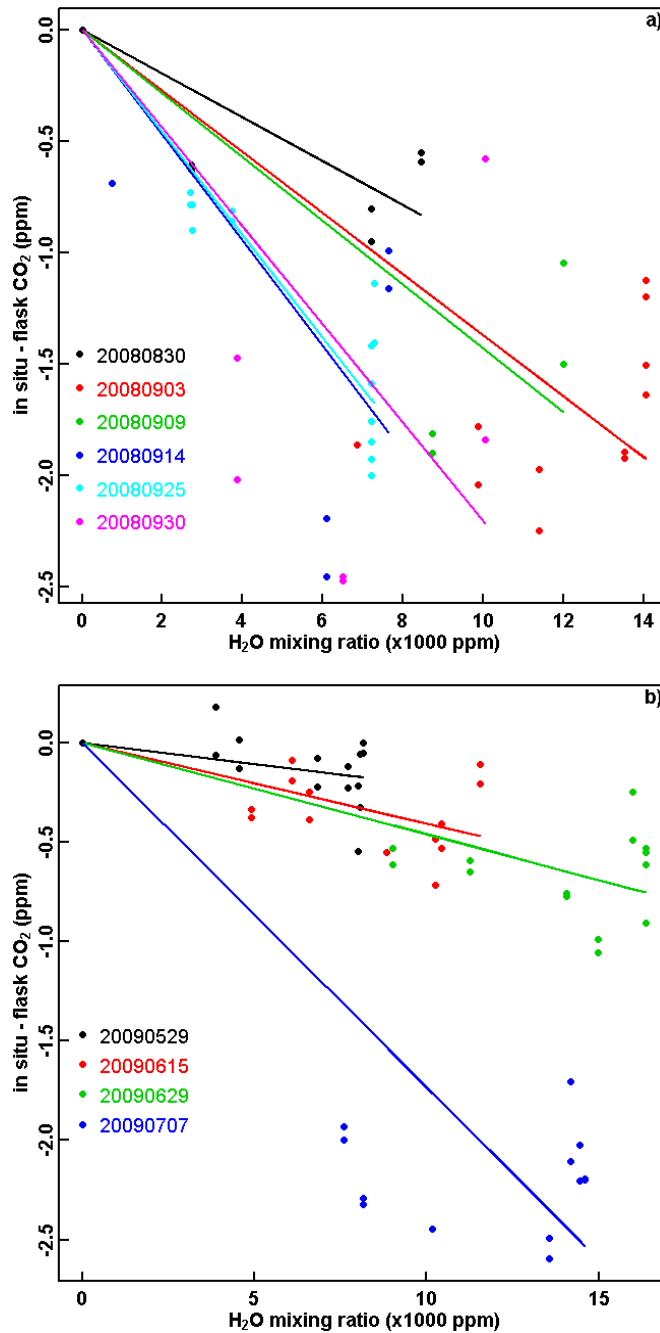


Figure 3.11. Linear regression models are fitted per flight using the least squares approach for the differences between in situ and flask CO<sub>2</sub> as a function of water vapor mixing ratios. The differences between in situ and flask CO<sub>2</sub> are denoted by different colors for each flight in the plots. Figures a and b show two periods during which the in situ measurements of CO<sub>2</sub> concentrations have been affected by residual water vapor after the chemical dryer.

### **3.4 Validation of airborne CO<sub>2</sub>/CH<sub>4</sub> measurements using the CRDS technique**

The BARCA project that took place over the Amazon rain forest in Brazil consisted of two phases. Phase A was done in November 2008 and Phase B took place in May 2009, covering the transitions from the wet season to the dry season and from the dry season to the wet season, respectively. During the Phase A campaign, an NDIR analyzer (Daube et al., 2002) was employed to measure CO<sub>2</sub> concentrations, while the flask sampler described in Chapter 3.2.1 was used to collect air samples for flask measurements of CO<sub>2</sub>, CH<sub>4</sub> and other species. The ambient relative humidity was monitored by a humidity and temperature probe (Vaisala, HMP45D). During Phase B, the CRDS flight analyzer discussed in Ch.2 was additionally deployed on board the same aircraft, resulting in three independent measurements of CO<sub>2</sub> concentrations and two independent measurements of CH<sub>4</sub> and H<sub>2</sub>O concentrations.

For the in situ CO<sub>2</sub> measurements made by the CRDS analyzer, various validations have been made: 1) assessment of the CO<sub>2</sub> measurement stability of the CRDS analyzer by comparison with an NDIR analyzer that was flown on board the same aircraft with frequent in-flight calibrations and a drying system; 2) calibration of the CRDS analyzer using synthetic air standards in the field; 3) comparison of in situ measurements of the CRDS analyzer with flask CO<sub>2</sub> measurements. A schematic diagram of these validations is shown in Fig. 3.12. For validation of CH<sub>4</sub> measurements, the only available method is to compare with flask CH<sub>4</sub> measurements.

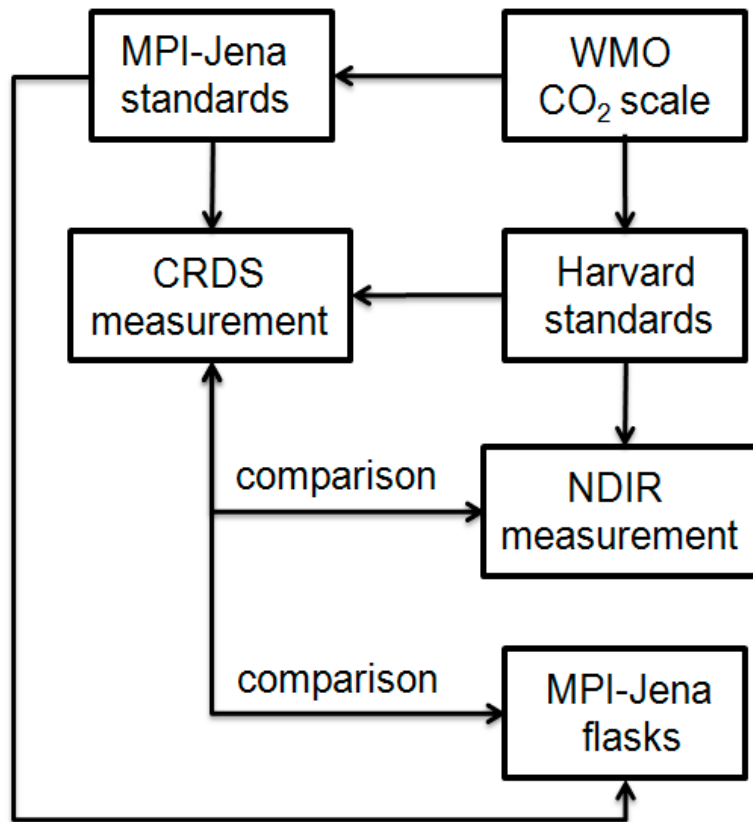


Figure 3.12. Schematic diagram for validation of CO<sub>2</sub> measurements by the CRDS analyzer during the BARCA campaign. The direct reference of CRDS measurement to MPI-BGC standards was done 4 months before the campaign.

### 3.4.1 Stability of measurements of CO<sub>2</sub> concentrations by the CRDS analyzer

In the first step, the in situ CO<sub>2</sub> measurements from both the CRDS and the NDIR analyzers are compared. Several issues need to be addressed regarding the comparison: the response time of the analyzers and the delay between the time air enters the inlet until it reaches the sample cell need to be estimated; CO<sub>2</sub> mixing ratio measurements from the NDIR analyzer requires on-line calibrations using in-flight calibration gases; inter-laboratory comparability of CO<sub>2</sub> standards and potential drift of the CRDS analyzer.

A detailed description of the NDIR CO<sub>2</sub> analyzer (modified Li-Cor, Inc. LI-6251) is given in Daube and Boering (2002); here only the points that are relevant to the comparison of CO<sub>2</sub> mixing ratio measurements from the two analyzers are described. The NDIR analyzer consists of a near infrared light source, gas cells and a solid-state detector. It uses the strong absorption band of CO<sub>2</sub> around 4.26 μm and is operated to perform differential measurements, with the sample air flowing through the sample cell at a flow rate of 200 sccm (standard cubic centimeters per minute) and one calibration gas flowing through the reference cell at a flow rate of 27 sccm. The cell volume is 11.9 cc and the pressure of the cell is controlled to ~450 mbar. Besides, a bypass flow is introduced when the system is doing calibrations. The response time of the NDIR analyzer (90 % response) is around 3.5 s. It employs a two-step drying system that is able to remove the water vapor in the sample air sufficiently and minimizes the effect on the instrument's response time. Four standard gases are used for in-flight CO<sub>2</sub> calibrations. Three were used as calibration gases and the other one was used as a target gas for long-term surveillance. The data from the NDIR analyzer were recorded at 4 Hz and were median-filtered within 2 seconds. A variable time delay correction was applied to the final data according to the inlet flow rate and estimated inlet volumes. The time delay during the BARCA phase B for the CO<sub>2</sub> mixing ratio measurements from the NDIR analyzer was between 3.2 s and 4.1 s.

The CRDS analyzer measured the three species of CO<sub>2</sub>, CH<sub>4</sub> and H<sub>2</sub>O sequentially. Mixing ratios of CO<sub>2</sub> were reported at time intervals of ~1.5 s, while mixing ratios of CH<sub>4</sub> and H<sub>2</sub>O were reported at time intervals of 3.0 s. The timestamp of each measurement made by the CRDS analyzer corresponded to the completion of the spectral

scan of each gas species, thus specifying the actual time when the sample was being measured to within a few hundred milliseconds. Laboratory tests showed that the sample flow rate ( $\sim 460$  sccm) of the CRDS analyzer was rather constant (less than 5 % change) over the range of the ambient pressure from 330 mbar to 1330 mbar. The volume of the cavity of the CRDS analyzer is  $35 \text{ cm}^3$  and the pressure of the cell is controlled at  $\sim 140$  Torr ( $\sim 186$  mbar). The response time (90 % response) of the CRDS analyzer was about 2 s. The time delay of between 6.3 s and 10 s was corrected based on the ambient pressure, the flow rate and estimated volumes of the inlet tube.

The time differences between the measurements of the two analyzers obtained by maximizing the correlation of the measurements in each individual flight are  $-0.2 \pm 1.2$  s, which is smaller than the time resolution of the CRDS analyzer (1.5 s) or of the reported NDIR results (2 s).

During flight, a slight increase in the variation of the cavity pressure of the CRDS analyzer for several short periods has been observed in the campaign. An imperfect control of the sampling gas flow may have been caused by mechanical vibrations, which leads to the variations in the cavity pressure. Two modifications have been made: one is to change the orientation of solenoid valves in the flow control unit from vertical to horizontal, because larger vertical vibrations are expected than horizontal vibrations during flight; the other is to modify the flow control frequency so that it is less influenced by the vibrations during flight. After these two modifications, the slightly larger variations in the cavity pressure for short periods have diminished to an insignificant level during later flights.

#### 3.4.1.1 Direct comparison results

During the BARCA phase B campaign, 16 flights were made, including one test flight in Sao Jose dos Campos and 15 flights over the Amazon rain forest. Table 2 shows the comparisons of the measurements of the two CO<sub>2</sub> analyzers. The missing values in the table are due to missing data for one of the analyzers or, in the worst case, both. The CRDS analyzer did not operate for two of the flights due to the failure of one temperature controller inside the analyzer for flights nos. 008 and 009, while the NDIR analyzer did not operate due to the failure of a pump in the case of flights nos. 009 and 010 and was not operated in the case of flight no. 014 to avoid catching rainwater.

With the test flight data removed (Flight No. 000), before which calibration gases had been sitting for almost half a year and during which the space inside the aircraft was severely overheated, the mean difference over all subsequent flights is  $0.22 \pm 0.09$  ppm, and the mean standard deviation of the difference is  $0.23 \pm 0.05$  ppm (see Table 2).

Table 2. Comparisons of CO<sub>2</sub> mixing ratio measurements from the CRDS analyzer and the NDIR analyzer on the Bandeirante EMB 110 aircraft during the BARCA phase B campaign in Brazil in 2009

Flight No.	Date (mmdd)	Difference (ppm)	Difference 1σ (ppm)	Difference after cross-calibration (ppm)	Difference after cross-calibration 1σ (ppm)
000	0511	1.39	0.87	*	*
001	0515	0.28	0.20	*	*
002	0517	0.20	0.23	0.06	0.25
003	0517	0.22	0.20	0.06	0.20
004	0519	0.34	0.32	0.19	0.32
005	0519	0.21	0.28	0.03	0.26
006	0521	0.12	0.22	-0.04	0.22
007	0521	0.11	0.26	-0.05	0.25
008	0522	**	**	**	**
009	0523	**	**	**	**
010	0523	**	**	**	**
011	0526	0.20	0.18	0.03	0.19
012	0526	0.18	0.15	0.01	0.16
013	0527	0.38	0.23	0.22	0.23
014	0527	**	**	**	**
015	0528	0.21	0.22	0.03	0.22
Average (not including flight nos. 000 and 001)		0.22	0.23	0.05	0.23

\* The calibration gases used in these two flights were not measured by the CRDS analyzer

\*\* Data missing from either of the two analyzers

#### 3.4.1.2 Cross-calibration during the BARCA campaign

In this section, the issues of inter-laboratory comparability of CO<sub>2</sub> standards from two different laboratories and the potential drifts in the calibration gases or in the CO<sub>2</sub> mixing ratio measurements of the CRDS analyzer are addressed, with the aim of explaining the mean difference of  $0.22 \pm 0.09$  ppm between the measurements of the two instruments.

As mentioned above, four in-flight calibration gases were used for the NDIR analyzer during the campaign. In addition, four filling tanks were employed to refill the internal small calibration cylinders in the NDIR analyzer whenever the pressure in these calibration cylinders dropped below  $\sim 3.4 \times 10^6$  Pa ( $\sim 34$  bar). Among the four filling tanks, three were calibrated at the Department of Earth and Planetary Sciences and the Division of Engineering and Applied Sciences at Harvard about one year prior to the campaign, and one reference gas tank was obtained in Brazil and calibrated by the flight NDIR analyzer in the field. All of the four filling tanks contained synthetic air.

The CRDS analyzer was calibrated using four ambient air standards in the laboratory of MPI-BGC, Germany, in January 2009, prior to shipment to Brazil. The CRDS analyzer response was linear, with residual errors for CO<sub>2</sub> below 0.02 ppm for the range from 354.71 ppm to 453.12 ppm and for CH<sub>4</sub> below 0.05 ppb for the range from 1804.73 ppb to 2296.69 ppb. No in-flight or ground calibrations for the CRDS analyzer were performed during the whole campaign; however, the four filling tanks used for refilling the in-flight calibration gas cylinders in the NDIR analyzer were measured by the CRDS analyzer immediately after the last flight of the campaign.

Both the Harvard and the MPI standard scales are traceable to the WMO CO<sub>2</sub> scales maintained in NOAA/ESRL (Zhao and Tans, 2006). However, there are potential causes for the mean difference of 0.22 ppm (see Table 2) between CO<sub>2</sub> concentration measurements from the NDIR and the CRDS analyzers: 1) CO<sub>2</sub> concentrations of Harvard standards might have drifted due to shipment and a one year storage period; 2) the CRDS analyzer might have drifted since the calibrations were made 4 months before



the campaign. For further comparison, the CRDS and the NDIR are placed on the same calibration scale. To achieve this, the measurements of the four filling tanks by the CRDS analyzer immediately after the last flight of the campaign are used and the CO<sub>2</sub> concentrations derived from the CRDS measurements are assigned to the concentrations of in-flight calibration gases used by the NDIR analyzer. Since the CRDS analyzer scans the spectrum of the absorption line of <sup>12</sup>C<sup>16</sup>O<sub>2</sub> and uses the peak height obtained from the fit of the spectral line to determine the mixing ratio of total CO<sub>2</sub> in air, the measurements are sensitive to variations of compositions (N<sub>2</sub>, O<sub>2</sub> and Ar) due to pressure broadening and to variations of carbon isotopologues. Therefore, the measurements of the four standard gases need to be corrected for the pressure-broadening and the isotope effects.

Unfortunately, the inert background gas fractions (N<sub>2</sub>, O<sub>2</sub>, and Ar) of the four filling tanks have not been measured. However, the Lorentzian broadening parameter was measured as part of the field campaign, and that data, along with a laboratory investigation of the dependence of the peak height of the absorption lines on Lorentzian broadening, were used to correct the calibration tank data reported by the CRDS analyzer.

#### 3.4.1.2.1 Corrections for the pressure-broadening effect

As noted above, any significant (> ~ 100 ppm) changes in the composition of the matrix gas in the calibration tanks can lead to variations in the line broadening parameters, which can in turn lead to variations in the reported concentrations of carbon dioxide and methane for a constant mixing ratio. For the inert gases N<sub>2</sub>, O<sub>2</sub>, and Ar, this is not typically of concern in the well-mixed atmosphere, but it can be of concern for synthetic gas standards, where the concentrations of these inert gases can vary widely.

Unfortunately, detailed measurements (or well-benchmarked calculations) of the Lorentzian and Galatry line shape parameters are not available for the optical transitions of carbon dioxide and methane in a background of varying N<sub>2</sub>, O<sub>2</sub>, and Ar. However, the direct measurements of the line broadening of the CO<sub>2</sub> absorption line can be used to correct for the line broadening effects of the inert gas composition.

The high-resolution spectral profile of <sup>12</sup>C<sup>16</sup>O<sub>2</sub> was recorded and was fitted using a Galatry profile model (Varghese and Hanson, 1984). In the Galatry model, pressure broadening consists of Lorentzian broadening (parameterized as the variable  $y$ , line width) and line narrowing (parameterized as the variable  $z$ ). Both  $y$  and  $z$  vary depending on the composition of the air. Ideally, changes in both  $y$  and  $z$  should be used to correct the pressure-broadening effect for measurements of synthetic air. However, the  $z$  parameter was not independently fitted during the measurements in Brazil, because the line-narrowing effect could not be clearly distinguished from noise in these data. This is due to the fact that the inert gas composition varied over a very small range of values in the filling tanks, and because the line-narrowing effect is of much smaller magnitude than the Lorentzian line broadening effect. Therefore, only the variation in the  $y$  parameter is used to correct the pressure-broadening effect, assuming that the  $z$  parameter is linearly correlated to the  $y$  parameter. For constant mixing ratios of CO<sub>2</sub> in air, the Galatry profiles vary according to  $y$  (with  $z$  proportional to  $y$ ), while the areas of the profiles are constant (see Fig. 3.13a). The correlation between the height and the width of the spectral profiles is shown in Fig. 3.13b. A simple Taylor expansion in the vicinity of the nominal  $y$ -value for ambient air predicts the following expression for the peak height as a function of  $y$ :

$$\frac{d[\text{peak}]}{dy} = B \times (y - y_{\text{nom}}) + A \quad (3.4)$$

Here [peak] represents the fractional change in the peak height, or  $\Delta\text{peak}/\text{peak}$ . For measurements of synthetic air standards, the  $y$  varies in such a very small range that  $\frac{d[\text{peak}]}{dy}$  can be regarded as a constant (i.e.,  $B = 0$ ). This constant value was determined from a laboratory experiment, in which three synthetic air standards were measured by a CRDS analyzer and a Gas Chromatograph (GC) to be  $0.34 \pm 0.05$  (see Table 3, the units here are expressed in fraction of the Doppler-broadened Gaussian width). Based on this correlation, the measured peak height can be corrected using the  $y$  parameters to compensate the pressure-broadening effect due to variations of compositions in air.

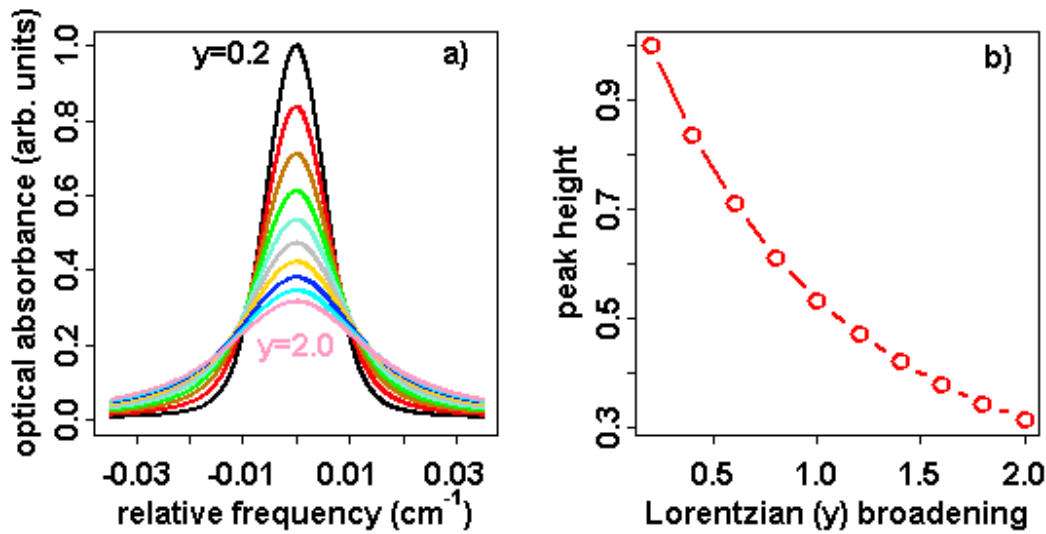


Figure 3.13. a) normalized absorption profiles for constant concentrations; b) correlation between peak height and Lorentzian ( $y$ ) broadening

The corrections for the pressure-broadening effect ranged from -0.22 ppm to 1.68 ppm for the four filling tanks. The uncertainty of this correction is mainly caused by the noise in the  $y$  parameter due to noise in the loss and wavelength values of the individual data points that make up the complete spectrogram. It is important to note that this noise is

the reason that the peak height rather than peak area is used to quantify the gas concentration. For 5-minute measurements of the filling tanks, the error of the mean of the pressure-broadening corrections is estimated to be 0.11 ppm.

*Table 3. Total CO<sub>2</sub> concentrations of the four filling tanks used during BARCA, derived from the laboratory experiments measuring synthetic air standards with known total CO<sub>2</sub> concentrations from GC*

Tanks	CRDS concentration readings (ppm)	$\Delta y^*$	d[peak]/dy	Total CO <sub>2</sub> concentrations from GC (ppm)	Total CO <sub>2</sub> concentration derived from the CRDS measurements (ppm)
Syn-1	406.71	0.0061 ± 0.0006	0.32 ± 0.03	407.59	–
Syn-2	392.36	0.0046 ± 0.0009	0.30 ± 0.06	392.84	–
Syn-3	372.47	0.0062 ± 0.0009	0.39 ± 0.06	373.11	–
Fill-1	363.13	-0.0018 ± 0.0011	0.34 ± 0.05 <sup>**</sup>	–	362.70
Fill-2	371.90	0.0001 ± 0.0012	0.34 ± 0.05 <sup>**</sup>	–	371.72
Fill-3	381.99	0.0130 ± 0.0011	0.34 ± 0.05 <sup>**</sup>	–	383.40
Fill-4	404.43	0.0069 ± 0.0010	0.34 ± 0.05 <sup>**</sup>	–	405.10

\*  $\Delta y$  was calculated as the difference between the mean values of  $y$ -parameters obtained from measuring a synthetic air standard and an ambient air standard, the values of  $y$  parameter range from 1.84 to 1.86

\*\* This value is the mean of d[peak]/dy values derived from the laboratory experiments of measuring three synthetic air standards, i.e., Syn-1, Syn-2 and Syn-3

### 3.4.1.2.2 Corrections for variations in carbon isotopologues

The CRDS analyzer measures the number of  $^{12}\text{C}^{16}\text{O}_2$  molecules, and determines total  $\text{CO}_2$  concentration by dividing the fractional abundance of  $^{12}\text{C}^{16}\text{O}_2$  in ambient air according to the calibration of the CRDS analyzer in the laboratory. The fractional abundance of isotopes in synthetic air can be different from that of ambient air since the  $\text{CO}_2$  in the synthetic air was from burned petroleum or natural gases. The isotopologues that could affect the measurements of total  $\text{CO}_2$  by more than 0.01 ppm are  $^{13}\text{C}^{16}\text{O}_2$  and  $^{12}\text{C}^{16}\text{O}^{18}\text{O}$  (Tohjima et al., 2009).

Practically, their fractional abundance can be derived from measurements of  $^{13}\text{C}/^{12}\text{C}$  and  $^{18}\text{O}/^{16}\text{O}$  isotope ratios. In the following, the impacts of variations in the two isotopologues on the  $\text{CO}_2$  mixing ratio measurements by the CRDS analyzer are discussed. The isotope ratios of  $^{13}\text{C}/^{12}\text{C}$  are normally expressed as  $\delta^{13}\text{C}$  values and are defined as follows:

$$\delta^{13}\text{C}(\text{‰}) = \left[ \frac{^{13}\text{R}_{\text{sample}}}{^{13}\text{R}_{\text{reference}}} - 1 \right] \times 10^3 \quad (3.5)$$

where  $^{13}\text{R}_{\text{sample}} = \left( \frac{^{13}\text{C}}{^{12}\text{C}} \right)_{\text{sample}}$ ,  $^{13}\text{R}_{\text{reference}} = \left( \frac{^{13}\text{C}}{^{12}\text{C}} \right)_{\text{reference}}$ . The  $\delta^{13}\text{C}$  values are expressed relative to the absolute  $^{13}\text{C}/^{12}\text{C}$  ratio of  $0.011180 \pm 0.000028$  for the reference materials of the Vienna Pee Dee Belemnite (VPDB) (Tohjima et al., 2009).

Similarly, the  $^{18}\text{O}/^{16}\text{O}$  isotopic ratios are expressed as  $\delta^{18}\text{O}$  values and are defined as

$$\delta^{18}\text{O}(\text{‰}) = \left[ \frac{^{18}\text{R}_{\text{sample}}}{^{18}\text{R}_{\text{reference}}} - 1 \right] \times 10^3 \quad (3.6)$$

where  $^{18}\text{R}_{\text{sample}} = \left(\frac{^{18}\text{O}}{^{16}\text{O}}\right)_{\text{sample}}$ ,  $^{18}\text{R}_{\text{reference}} = \left(\frac{^{18}\text{O}}{^{16}\text{O}}\right)_{\text{reference}}$ .

The  $\delta^{18}\text{O}$  values are expressed relative to the ratio of Vienna Standard Mean Ocean Water (VSMOW), an isotopic water standard. The  $^{18}\text{O}/^{16}\text{O}$  ratio of the VSMOW is  $2.00520 \times 10^{-3}$  (Baertschi, 1976). When measuring synthetic air, the CRDS analyzer calculated the  $\text{CO}_2$  mixing ratio by using the  $^{13}\text{C}/^{12}\text{C}$  and  $^{18}\text{O}/^{16}\text{O}$  ratios of ambient air. The readings of synthetic  $\text{CO}_2$  measurements can be expressed as:

$$\text{CO}_{2\text{meas}} = {}^{12}\text{C}^{16}\text{O}_2 \times (1 + {}^{13}\text{R}_{\text{amb}} + 2 \times {}^{18}\text{R}_{\text{amb}}) \quad (3.7)$$

However, the  $\text{CO}_2$  mixing ratio of the synthetic air should be calculated as:

$$\text{CO}_{2\text{syn}} = {}^{12}\text{C}^{16}\text{O}_2 \times (1 + {}^{13}\text{R}_{\text{syn}} + 2 \times {}^{18}\text{R}_{\text{syn}}) \quad (3.8)$$

Here,  $\text{CO}_2$  and  ${}^{12}\text{C}^{16}\text{O}_2$  denote the total  $\text{CO}_2$  mixing ratio and the mixing ratio of  ${}^{12}\text{C}^{16}\text{O}_2$ , respectively. From equations (2) - (5), the equation for calculating  $\text{CO}_2$  in the synthetic air can be derived

$$\text{CO}_{2\text{syn}} = \text{CO}_{2\text{syn}} \times \frac{1 + {}^{13}\text{R}_{\text{ref}} \times (1 + \delta^{13}\text{C}_{\text{syn}}) + 2 \times {}^{18}\text{R}_{\text{ref}} \times (1 + \delta^{18}\text{O}_{\text{syn}})}{1 + {}^{13}\text{R}_{\text{ref}} \times (1 + \delta^{13}\text{C}_{\text{amb}}) + 2 \times {}^{18}\text{R}_{\text{ref}} \times (1 + \delta^{18}\text{O}_{\text{amb}})} \quad (3.9)$$

The  $\delta^{13}\text{C}$  and  $\delta^{18}\text{O}$  values of ambient  $\text{CO}_2$  are around -8 ‰ on the VPDB scale (GLOBALVIEW-cO<sub>2</sub>c13, 2009) and around 42 ‰ on the VSMOW scale (Allison and Francey, 2007), respectively. Unfortunately, direct  $\delta^{13}\text{C}$  and  $\delta^{18}\text{O}$  measurements for the four filling tanks are not available and not easy to obtain due to logistical difficulties. An estimate for the  $\delta^{13}\text{C}$  and  $\delta^{18}\text{O}$  values of synthetic air, with  $\text{CO}_2$  from burned petroleum or natural gas added (as used in the four filling tanks), can be given based on isotope-abundance variations (Coplen et al., 2002), which results in values for  $\delta^{13}\text{C}$  of  $-37 \pm 11$  ‰ on the VPDB scale, and for  $\delta^{18}\text{O}$  of  $24 \pm 10$  ‰ on the VSMOW scale. The corrections due to variations of  $\delta^{13}\text{C}$  and  $\delta^{18}\text{O}$  values for the filling tanks using these values are

0.14 ~ 0.16 ± 0.06 ppm, which is a small correction range compared to the correction range for the above pressure-broadening effect.

After the above described corrections, the total CO<sub>2</sub> values of the filling tanks were finally determined (see Table 4). However, the assigned values to the NDIR in-flight calibrations need to incorporate the isotopic effect for the original calibrations as well, since they were performed against ambient air standards by an NDIR analyzer (modified Li-Cor, Inc. LI-6251). The isotope effect of an NDIR analyzer can be evaluated based on the relative molar response (RMR) value of the NDIR analyzer and the difference in the mole fraction of the isotopologues between the ambient and the synthetic air (Tohjima et al., 2009). The RMR values obtained by Tohjima et al. (2009) and the mole fraction differences described above were employed to estimate the isotopic effect; the results show that the original calibrations were 0.09 ± 0.02 ppm higher than corresponding total CO<sub>2</sub> mixing ratios. Notice that no correction was required when the NDIR analyzer was used to measure atmospheric air since the isotope effect was cancelled out. Therefore, the assigned value to the NDIR in-flight calibrations should be the determined total CO<sub>2</sub> values by the CRDS plus 0.09 ppm (see Table 4).

*Table 4. Assignment of CO<sub>2</sub> corrections to the calibration gases used by the NDIR analyzer derived from the CRDS analyzer*

Tanks	Total CO <sub>2</sub> concentrations derived from the CRDS measurements (ppm)	Assigned concentrations to the NDIR calibration gases (ppm) <sup>*</sup>	Harvard calibrations (ppm) <sup>**</sup>	Differences between the assigned and Harvard calibrations (ppm)
Low span	362.70	362.79	362.87	-0.08
Target	371.72	371.81	371.61	0.20
Reference	383.40	383.49	383.30 <sup>***</sup>	0.19
High span	405.10	405.19	405.41	-0.22

*\*The concentrations from the CRDS measurements plus isotope corrections due to the isotope effect in the mixing ratio measurements by the NDIR technique*

*\*\*Calibrations were done at Harvard University before shipment to Brazil in July, 2008*

*\*\*\*Not directly calibrated, but derived from the target calibration gas (due to logistic difficulties associated with exporting hazardous materials from Brazil)*

The differences between the values assigned to the NDIR and the Harvard calibration values are listed as well. The values assigned for the four tanks were applied as the standards to reprocess the NDIR data. The comparisons between the CRDS and the reprocessed NDIR data are shown in the last two columns in Table 2. The mean difference between the two analyzers is reduced to  $0.05 \pm 0.09$  ppm. The uncertainties related to the comparison between the two CO<sub>2</sub> analyzers are summed up in Table 5. The total uncertainty related to the comparison is estimated to be 0.14 ppm. The good agreement between the measurements of the CRDS and the NDIR analyzers after placing them on the same scale proved that 1) the CRDS analyzer during the BARCA phase B campaign was highly stable ( $\sim 0.05$  ppm); 2) water corrections for CO<sub>2</sub> and CH<sub>4</sub> using simultaneously measured water vapor were fully adequate.



*Table 5. Uncertainties related to comparison between the two CO<sub>2</sub> analyzers*

sources	Uncertainties (ppm)	Remarks
Water correction	0.05	Maximum residual error
Corrections for pressure broadening	0.11	The error of the mean of corrections for pressure broadening
Carbon isotope correction	0.06	Uncertainties in estimated $\delta^{13}\text{C}$ and $\delta^{18}\text{O}$ values
Carbon isotope effects on the NDIR analyzer	0.02	Variations of RMRs for different NDIR analyzers
Total uncertainty	0.14	

### **3.4.2 Accuracy of in situ CO<sub>2</sub> and CH<sub>4</sub> measurements during BARCA**

The accuracy of the CO<sub>2</sub> measurements of the CRDS analyzer during BARCA relative to the WMO scale is dependent on potential drift of the analyzer. A direct method would be to calibrate the analyzer using ambient air standards in the field; however, this was not possible due to logistical difficulties (shipping compressed gases to Brazil on a short time scale was not possible). Here two alternatives were employed to assure or assess the accuracy: 1) calibration of the analyzer using the synthetic air standards from the Harvard group; 2) comparison of in situ measurements with analysis of flask samples. In the case of CH<sub>4</sub>, the in situ measurements could only be compared with flask measurements as no calibration gas for CH<sub>4</sub> was available in the field.

#### **3.4.2.1 Calibration of the CRDS analyzer using synthetic air standards**

Three synthetic air standards used during BARCA were recalibrated in the laboratory of the Harvard group in January, 2010. These new values are used to calibrate the CO<sub>2</sub> measurements by the CRDS analyzer. The reason for using the recalibrated values instead of the calibration values obtained one year before the campaign is that drifts in the synthetic air standards more likely happened during the process of refilling the small

cylinders in the field rather than during shipment and storage. Therefore, CO<sub>2</sub> concentration values acquired in January 2010 are closer to the values when they were measured by the CRDS analyzer during the end of the campaign period. A linear regression is performed to derive the correction coefficients: intercept  $A = -2.42$  ppm, and slope  $B = 1.0066$  (see Fig. 3.14). The magnitude of the residuals is 0.17 ppm, which is due to the corrections (see Table 5) that have been made to the measurements of synthetic air standards by the CRDS analyzer.

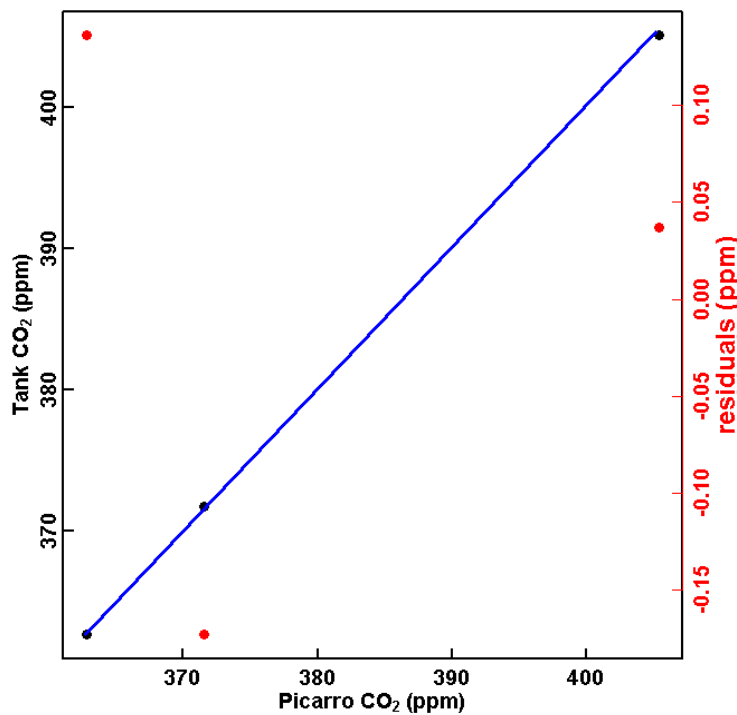


Figure 3.14. Calibration of the CO<sub>2</sub> measurements of the Picarro CRDS analyzer using three synthetic air standards, with residuals shown in red dots and read on the right axis.

The two coefficients  $A$  and  $B$  are used to correct all in situ CO<sub>2</sub> measurements made by the CRDS analyzer during BARCA. The accuracy of these in situ CO<sub>2</sub> measurements is also checked by comparison with flask CO<sub>2</sub> measurements, which is presented in the following section.

#### 3.4.2.2 Comparison of in situ with flask CO<sub>2</sub> and CH<sub>4</sub> measurements

The flasks are selected for the comparison based on two criteria: 1) no leaking of air out of the flask when the flask pressure reaches one bar above ambient; 2) the fraction of missing values due to calibration of the continuous CO<sub>2</sub> (in the case of the NDIR analyzer) during the flask sampling period is smaller than 30%. CO<sub>2</sub> concentrations from both the CRDS analyzer and the NDIR analyzer have been compared with flask CO<sub>2</sub> values (see Fig. 3.15). The in situ CO<sub>2</sub> concentrations from the CRDS analyzer are based on the calibration using three synthetic air standards; the comparisons (Fig. 3.15a) show differences with a mean of 0.09 ppm and a standard deviation of differences of 0.14 ppm, which is within the uncertainties of the in situ measurements of CO<sub>2</sub> concentrations. The comparisons of in situ measurements of CO<sub>2</sub> concentrations from the NDIR analyzer with flask values (Fig. 3.15b) have differences of -0.20 ppm (mean), with a standard deviation of differences of 0.31 ppm. Note that the in situ measurements of CO<sub>2</sub> concentrations from the NDIR analyzer have not been reprocessed using the recalibrated values; the mean difference of -0.20 ppm could be explained by the concentration changes of the calibration gases in the filling tanks as well as the compatibility error of calibration standards between MPI-BGC and Harvard. The slightly larger standard deviation could be caused by the uncertainty in the CO<sub>2</sub> values of the in-flight calibration gases.

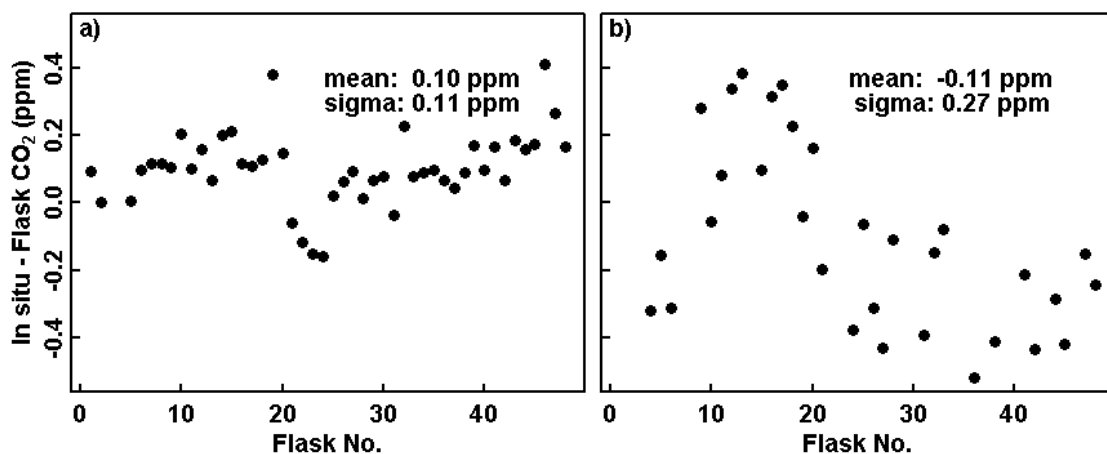


Figure 3.15. Comparison of in situ with flask measurements of CO<sub>2</sub> concentrations, plotted as a function of flask number, with mean and standard values shown in each figure: a. the in situ data are from the CRDS analyzer and b. the in situ data are from the NDIR analyzer. Note that some flask comparisons are excluded due to concurrence of calibrations of the NDIR analyzer and flask sampling.

Similarly, comparisons of in situ measurements of CH<sub>4</sub> concentrations from the CRDS analyzer with CH<sub>4</sub> flask measurements are made and shown in Fig. 3.16. The mean of the differences is -0.85 ppb and the standard deviation of differences is 2.49 ppb, which is around the uncertainty of the in situ measurements of CH<sub>4</sub> concentrations by the CRDS analyzer.

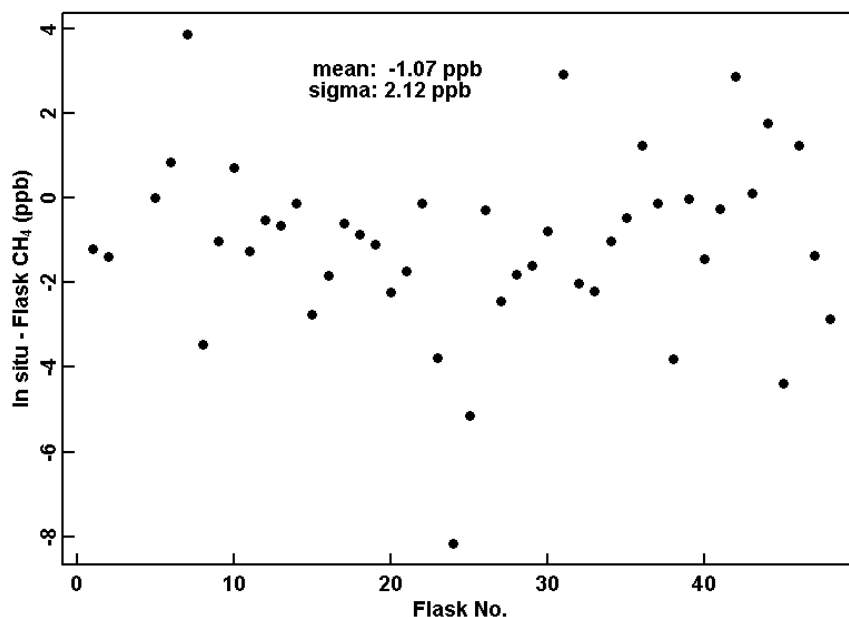


Figure 3.16. Comparison of in situ with flask measurements of CH<sub>4</sub> concentrations, plotted as a function of flask number, with mean and standard values shown.

### 3.5 Conclusions

Validation of in situ measurements from analyzers using the NDIR and CRDS techniques are presented, based on comparisons of in situ with flask measurements as well as between different in situ analyzers when available. The weighting functions for integrating in situ measurements to compare with single flask and paired flasks have been derived and proven to be able to account for the variability of in situ measurements during the period of flask sampling. The issue of insufficient drying effects has been discovered through the comparison of in situ with flask measurements of CO<sub>2</sub> concentrations from regular flights over BIK tower, and corrections have been made based on these comparisons.

The comparison of in situ measurements of CO<sub>2</sub> concentrations made by the CRDS analyzer and an NDIR analyzer on board the same aircraft during BARCA showed that measurements by the CRDS analyzer are sufficiently stable without in-flight calibrations or drying of the air sample over the campaign period. Measurements of synthetic air from the filling tanks used for the NDIR analyzer at the end of the campaign were carried out and the concentrations were determined after correcting for the variation in carbon isotopologues and for pressure-broadening effects due to variations of composition of O<sub>2</sub>, N<sub>2</sub> and Ar in synthetic air vs. in ambient air. Application of these calibrations reduced the mean of the difference between the CRDS and the NDIR during BARCA to  $0.05 \pm 0.09$  ppm. Due to the necessity of corrections for the isotope and pressure-broadening effects for CO<sub>2</sub> concentration measurements of synthetic air that introduces non-negligible uncertainties, it is strongly recommended based on these experiments to use ambient air standards instead of synthetic air standards for calibrating the CRDS analyzer.

The comparison of in situ measurements of CO<sub>2</sub> and CH<sub>4</sub> concentrations by the CRDS analyzer with flask measurements confirmed the accuracy to be within the uncertainty of measurements of each species.

### **3.6 References**

- Bischof, W. (1962). "Variations in Concentration of Carbon Dioxide in the Free Atmosphere." Tellus **14**(1): 87-90.
- Callendar, G. S. (1938). "The artificial production of carbon dioxide and its influence on temperature." Quarterly Journal of the Royal Meteorological Society **64**: 223-240.

- Chen, H., W. J., C. Gerbig, H. A., C. W. Rella, E. R. Crosson, V. P. A.D., J. Steinbach, O. Kolle, V. Beck, B. C. Daube, G. E.W., V. Y. Chow, G. W. Santoni and S. C. Wofsy (2010). "High-accuracy continuous airborne measurements of greenhouse gases (CO<sub>2</sub> and CH<sub>4</sub>) using the cavity ring-down spectroscopy (CRDS) technique." Atmos. Meas. Tech. **3**: 375-386.
- Daube, B. C., K. A. Boering, A. E. Andrews and S. C. Wofsy (2002). "A high-precision fast-response airborne CO<sub>2</sub> analyzer for in situ sampling from the surface to the middle stratosphere." Journal of Atmospheric and Oceanic Technology **19**(10): 1532-1543.
- Dlugokencky, E. J., R. C. Myers, P. M. Lang, K. A. Masarie, A. M. Crowell, K. W. Thoning, B. D. Hall, J. W. Elkins and L. P. Steele (2005). "Conversion of NOAA atmospheric dry air CH<sub>4</sub> mole fractions to a gravimetrically prepared standard scale." Journal of Geophysical Research-Atmospheres **110**(D18).
- Gurk, C., H. Fischer, P. Hoor, M. G. Lawrence, J. Lelieveld and H. Wernli (2008). "Airborne in-situ measurements of vertical, seasonal and latitudinal distributions of carbon dioxide over Europe." Atmospheric Chemistry and Physics **8**(21): 6395-6403.
- Gurney, K. R., R. M. Law, A. S. Denning, P. J. Rayner, D. Baker, P. Bousquet, L. Bruhwiler, Y. H. Chen, P. Ciais, S. Fan, I. Y. Fung, M. Gloor, M. Heimann, K. Higuchi, J. John, T. Maki, S. Maksyutov, K. Masarie, P. Peylin, M. Prather, B. C. Pak, J. Randerson, J. Sarmiento, S. Taguchi, T. Takahashi and C. W. Yuen (2002). "Towards robust regional estimates of CO<sub>2</sub> sources and sinks using atmospheric transport models." Nature **415**(6872): 626-630.
- Katrynski, K. S. (2006). "Quantifying the terrestrial carbon budget of middle latitude ecosystems: the role of Volatile Organic Compounds." Ph.D. thesis, Max Planck Institute for Biogeochemistry, Jena, Germany
- Langenfelds, R. L., M. V. van der Schoot, R. J. Francey, L. P. Steele, M. Schmidt and H. Mukai (2005). "Modification of air standard composition by diffusive and surface processes." Journal of Geophysical Research-Atmospheres **110**(D13).
- Lloyd, J., R. L. Langenfelds, R. J. Francey, M. Gloor, N. M. Tchebakova, D. Zolotoukhine, W. A. Brand, R. A. Werner, A. Jordan, C. A. Allison, V. Zrazhewske, O. Shibistova and E. D. Schulze (2002). "A trace-gas climatology above Zotino, central Siberia." Tellus Series B-Chemical and Physical Meteorology **54**(5): 749-767.
- Machida, T., H. Matsueda, Y. Sawa, Y. Nakagawa, K. Hirotani, N. Kondo, K. Goto, T. Nakazawa, K. Ishikawa and T. Ogawa (2008). "Worldwide Measurements of

- Atmospheric CO<sub>2</sub> and Other Trace Gas Species Using Commercial Airlines." Journal of Atmospheric and Oceanic Technology **25**(10): 1744-1754.
- Martins, D. K., C. Sweeney, B. H. Stirm and P. B. Shepson (2009). "Regional surface flux of CO<sub>2</sub> inferred from changes in the advected CO<sub>2</sub> column density." Agricultural and Forest Meteorology **149**(10): 1674-1685.
- Pales, J. C. and C. D. Keeling (1965). "Concentration of Atmospheric Carbon Dioxide in Hawaii." Journal of Geophysical Research **70**(24): 6053-&.
- Tans, P. P., P. S. Bakwin and D. W. Guenther (1996). "A feasible global carbon cycle observing system: A plan to decipher today's carbon cycle based on observations." Global Change Biology **2**(3): 309-318.
- VIM3 (2007). "BIPM, IEC, IFCC, ILAC, ISO, IUPAC, IUPAP and OIML 2007 International Vocabulary of Metrology—Basic and General Concepts and Associated Terms (VIM) ISO/IEC Guide 99 (Geneva: ISO)."
- WMO (2003). "Report of the 11th WMO/IAEA Meeting of Experts on Carbon Dioxide Concentration and Related Tracer Measurement Techniques, Tokyo, Japan, 25–28 September 2001, Tech. Rep. 148, World Meteorological Organisation – Global Atmospheric Watch, Geneva, Switzerland."
- Zhao, C. L. and P. P. Tans (2006). "Estimating uncertainty of the WMO mole fraction scale for carbon dioxide in air." Journal of Geophysical Research-Atmospheres **111**(D8).



## **Chapter 4 Representativeness analysis of aircraft**

### **CO/CO<sub>2</sub> profiles**

#### **4.1 Introduction**

Atmospheric CO<sub>2</sub> observations have been employed to derive sources and sinks of carbon through inverse modeling (Rayner et al., 1999; Roedenbeck et al., 2003); however, large uncertainties exist in these estimations due to insufficient constraints by observations as well as due to transport and representation errors (Engelen et al., 2002; Gerbig et al., 2008). Global inverse studies with atmospheric tracer transport models can provide information about carbon fluxes on a continental scale, but these inversions lack sufficient constraints on regional carbon fluxes (Gurney et al., 2002). On one hand, these uncertainties can be reduced by expansion of the CO<sub>2</sub> observation network. On the other hand, atmospheric transport models do not accurately represent vertical CO<sub>2</sub> gradients of aircraft profiles, which could potentially be responsible for biases in the flux estimations (Stephens et al., 2007). Therefore, regular aircraft profiles are desired in order to improve the vertical mixing of transport models (Gerbig et al., 2008). Moreover, vertical profiles of CO<sub>2</sub> from in situ measurements represent the only method to validate observations based on remote sensing techniques, which are expected to become an important source of information in the future (Miller et al., 2005).

Routine aircraft CO<sub>2</sub> profiles will be obtained starting from 2011 within the In-service Aircraft for a Global Observing System (IAGOS) project, and a large number of aircraft profiles are expected to be obtained. However, the aircraft CO<sub>2</sub> profiles from such a

commercial airliner program are usually made near populated cities and thus could be contaminated by local pollution. To make use of these profiles for validating observations based on remote sensing techniques or estimating source-sink distributions of CO<sub>2</sub> in inverse modeling frameworks, it is important to assess their representativeness. Here the representativeness analysis considers whether these CO<sub>2</sub>/CO profiles are regionally representative or contaminated by local fossil fuel emissions, and characterizes the magnitude of spatial representation errors due to different processes and mismatches between model and data.

Aircraft CO profiles (Nedelec et al., 2003) near Frankfurt (Main), Germany, have been made within the Measurement of OZone and water vapor by AIrbus in-service airCRAFT (MOZAIC) project, the precursor of the IAGOS project. Frankfurt is used to refer to Frankfurt (Main) throughout the subsequent text. CO can be used as a proxy for the CO<sub>2</sub> component from fossil fuel burning since it is co-emitted with CO<sub>2</sub> due to incomplete combustion at a typical CO/CO<sub>2</sub>(foss) ratio of, e.g., 10 – 20 ppb/ppm for Germany (Gamnitzer et al., 2006; Levin et al., 2007). Therefore, the representativeness of CO<sub>2</sub> profiles can be investigated based on the available CO profiles from the MOZAIC project.

The mismatch between point observations by aircraft and spatial averages simulated by models or from Fourier Transform Spectroscopy (FTS) and satellites is the so-called spatial “representation error,” which has been characterized through studies on the spatial variability of CO<sub>2</sub> concentrations based on observations (Gerbig et al., 2003a; Lin et al., 2004) and high-resolution modeling (Tolk et al., 2008; Pillai et al., 2010). These analyses reveal the magnitude of spatial representation errors when model simulations are used to

reproduce aircraft or satellite CO<sub>2</sub> observations during the growing season over North America and Europe. The spatial representation error of observations for inverse modeling is site- and time-dependent, and can be addressed by observations at multiple locations within distances corresponding to the resolution of transport models. An alternative is to assess the representation error based on the differences between simulated CO<sub>2</sub> from a high-resolution model run and from the degraded runs (Gerbig et al., 2003b). The variability of sources and sinks in the vicinity determines the magnitude of the representation error, e.g., the representation error of observations at a continental site is usually larger than that at a marine site.

Aircraft profiles of atmospheric CO<sub>2</sub>/CO collected using a rental aircraft near a reference site, the Bialystok (BIK) tall tower in northeastern Poland, are explored. For analysis, these profiles are grouped into two categories: regular in situ CO<sub>2</sub> profiles at two different locations are employed to assess the spatial variability, i.e., spatial representation error; regular CO<sub>2</sub>/CO profiles from analyses of air samples at one location are examined to provide a reference for the representativeness. This reference site is classified as a rural station (Henne et al., 2010) and has been chosen as a station for monitoring atmospheric background greenhouse gases and related tracers (Popa et al., 2010). The observations at BIK are assumed to be little influenced by local pollution, and regionally representative.

The surroundings of the reference site (BIK) and of one of the commercial airliner profile locations (Frankfurt airport) are shown in Fig 4.1 with the corresponding land-cover maps. The profiles at BIK are made at a relatively fixed location over a national park, while the profiles over Frankfurt are made in a certain area surrounding the Frankfurt

airport, and differ from flight to flight. It is clearly seen that the region surrounding Frankfurt is significantly more urban when compared to the reference site (urban areas are shown as red dots).

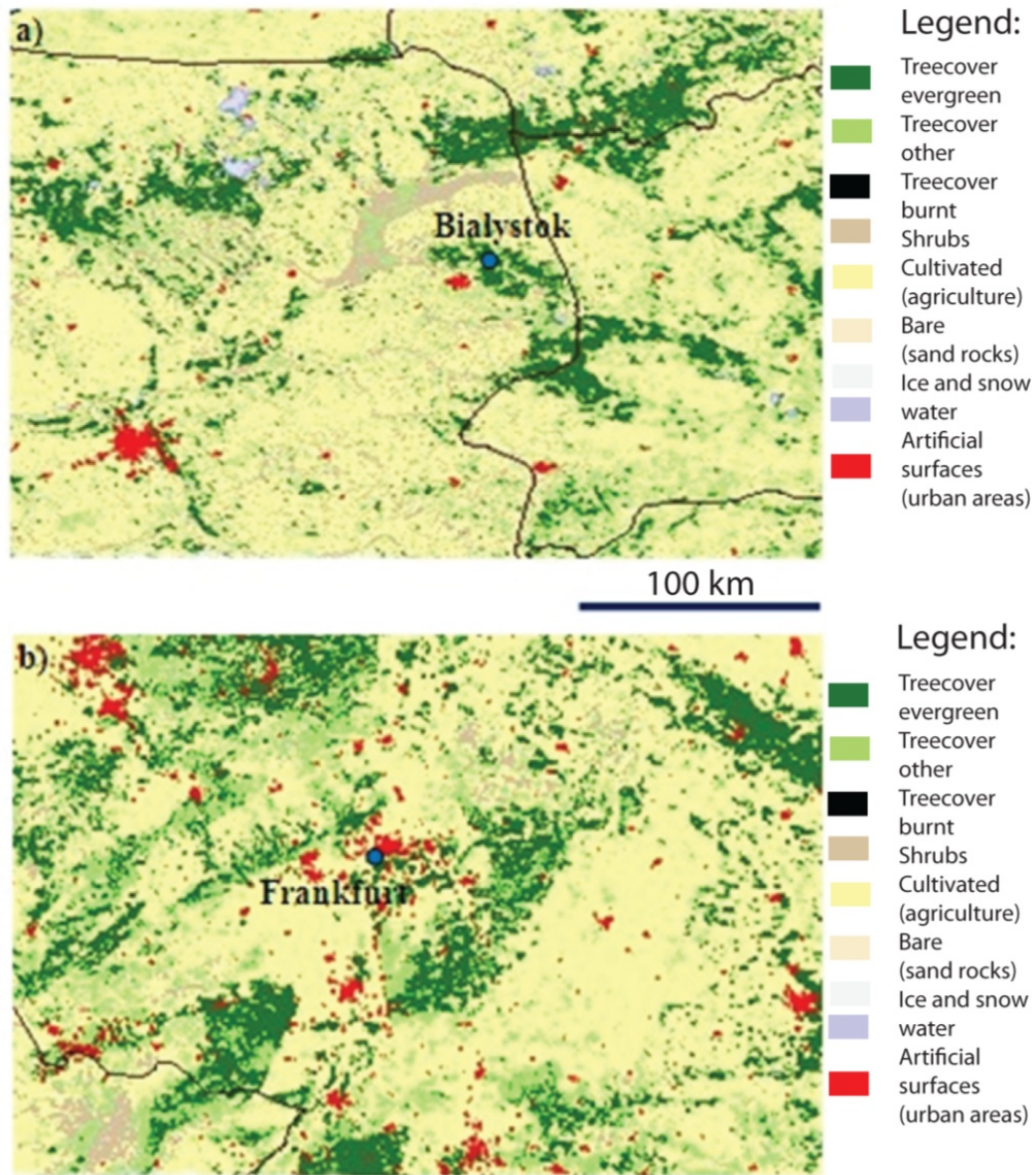


Figure 4.1 Land-cover maps a) centered at a remote site near Bialystok, Poland and b) centered at the city of Frankfurt am Main, Germany. (Source: Global Land Cover 2000 database. European Commission, Joint Research Centre, 2003). The blue dots indicate the locations of the profiles at BIK (a) and the city of Frankfurt (b). The color scheme for different types of land covers is given on the right of the figures.

This chapter is organized as follows: Chapter 4.2 analyzes the representativeness of airborne CO/CO<sub>2</sub> observations from a commercial airliner program; Chapter 4.3 assesses the spatial representation error of in situ CO<sub>2</sub> profiles at two locations and further investigates the representativeness of aircraft CO/CO<sub>2</sub> profiles near the remote site (BIK) in Poland; Chapter 4.4 discusses the comparison between the commercial airliner profiling site and the reference site and provides conclusions.

## **4.2 Representativeness analysis of CO profiles from a commercial airliner program**

The representativeness of profiles from a commercial airliner program is investigated based on the observed CO profiles over Frankfurt from the MOZAIC project: first statistical analysis is presented, and then the observations are assessed in a modeling framework. Frankfurt is chosen for the analyses because profiles made at this site are potentially polluted by fossil fuel emissions from the surrounding urban areas (see Fig. 4.1). Another reason is that profiles have been most frequently made at this site.

### **4.2.1 Statistical analysis of CO profiles over Frankfurt**

The measurements made over Frankfurt during the years 2002-2004, consisting of 1943 profiles, have been used to perform the statistical studies. The distribution of the number of profiles over the time shows that profiles were more frequently taken in 2003 and 2004 than in 2002 (Fig. 4.2).

The distribution of the number of profiles over the hour of the day shows several spikes centered at UTC 4:00, 8:00, 12:00, 16:00 and 22:00, which correspond to the scheduled

take-off or landing hours of the passenger aircraft that carry the MOZAIC instruments (Fig. 4.3). Note that a large number of profiles were taken during nighttime.

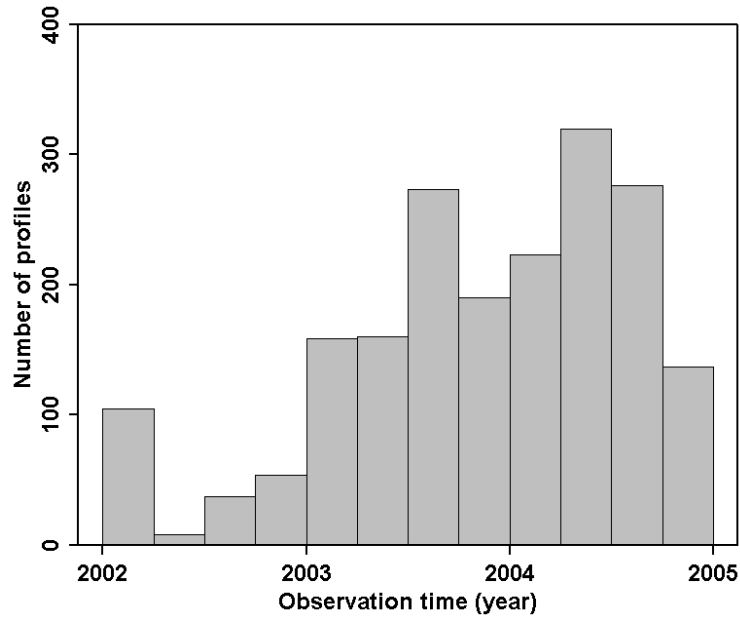


Figure 4.2 Temporal distribution of the number of profiles for the MOZAIC profiles over Frankfurt during the years 2002-2004, binned in three-month periods

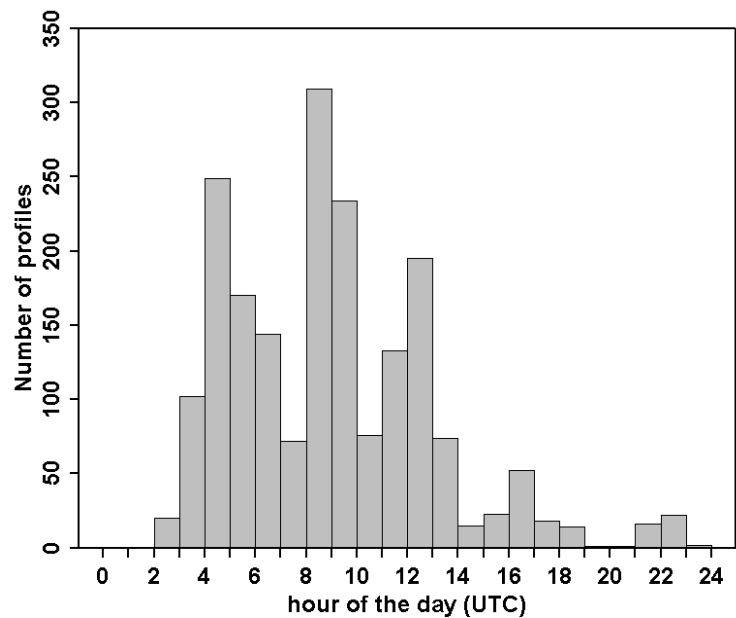


Figure 4.3 Temporal distribution of the number of profiles for the MOZAIC profiles over Frankfurt during the years 2002-2004, binned by hour of day

An overview of the locations of observations below 2000 m for the profiles into and out of the Frankfurt airport (Fig.4.4) shows that the distance of the observations to the Frankfurt airport increases with altitude, as the aircrafts always either climb (after take-off) or descend (before landing). The regular pattern for the flight tracks (mostly below 1000m) is associated with the airfield traffic pattern (different paths that aircraft are bound to correspond to different wind directions). The locations of observations are overlaid on a fossil fuel CO emission map (annual mean fluxes from the IER emission inventory) at a resolution of 10 km by 10 km. The emissions near the airport and the city are high, but decrease sharply with the distance from the airport or the city (note that the color is on the logarithmic scale). The city of Frankfurt is about 10 km to the northeast of the airport.

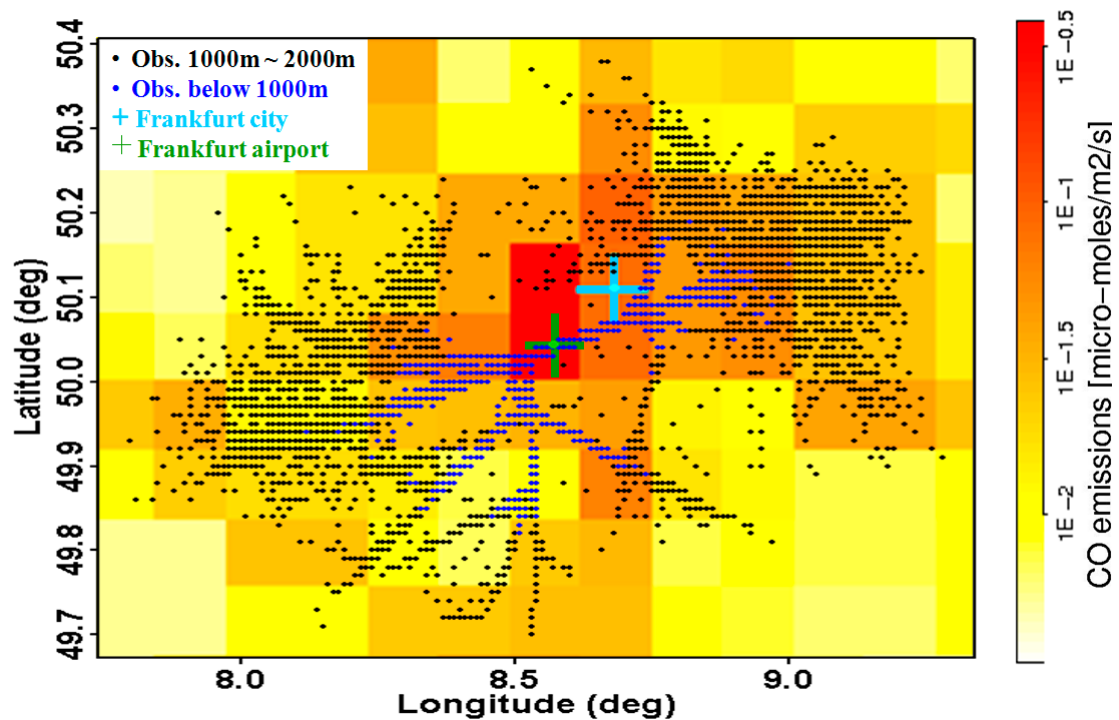


Figure 4.4 Locations of CO observations from profiles (for the years 2002-2004) over Frankfurt superimposed on a CO fossil fuel emission map. The Frankfurt airport and the city of Frankfurt are shown as green and cyan crosses. The dots indicate the locations of profile observations (aggregated into 150m vertical bins) from the lower part of profiles (blue: 0-1000 m, black: 1000-2000m). The color is on a logarithmic scale and shown on the right of the figure.

For further analysis, enhancements of CO within the planetary boundary layer (PBL) are calculated for profiles that were taken during daytime (UTC 11:00 – 17:00). 492 out of 1943 profiles are selected. The reason for selecting only daytime profiles is that during nighttime the PBL is normally shallow and is largely influenced by local emissions. This is also consistent with the data used for model simulations given in the following section.

The PBL is the lowest part of the atmosphere that is strongly influenced by exchange processes at the Earth’s surface. Emissions from local and regional sources are mixed



vertically within this layer. Besides CO, meteorological parameters (ambient pressure, relative humidity, temperature, wind speed, and wind direction) and aircraft location and speed were measured during MOZAIC flight as well. First the height of the PBL,  $z_i$ , is determined from the potential temperature profile for each profile using the parcel method (Seibert et al., 2000). The CO enhancements are then calculated from the CO profiles as the CO concentration within the PBL subtracting the CO values at 2km above  $z_i$  (Fig. 4.5). The PBL is divided into the lower half and the upper half and the average of each is calculated. The reason for separating the PBL is that the distances of the observations in the upper half of the PBL to the airport or the city are larger than in the lower half of the PBL, and the local fossil fuel emissions might have a different impact on the observations at different parts of the PBL.

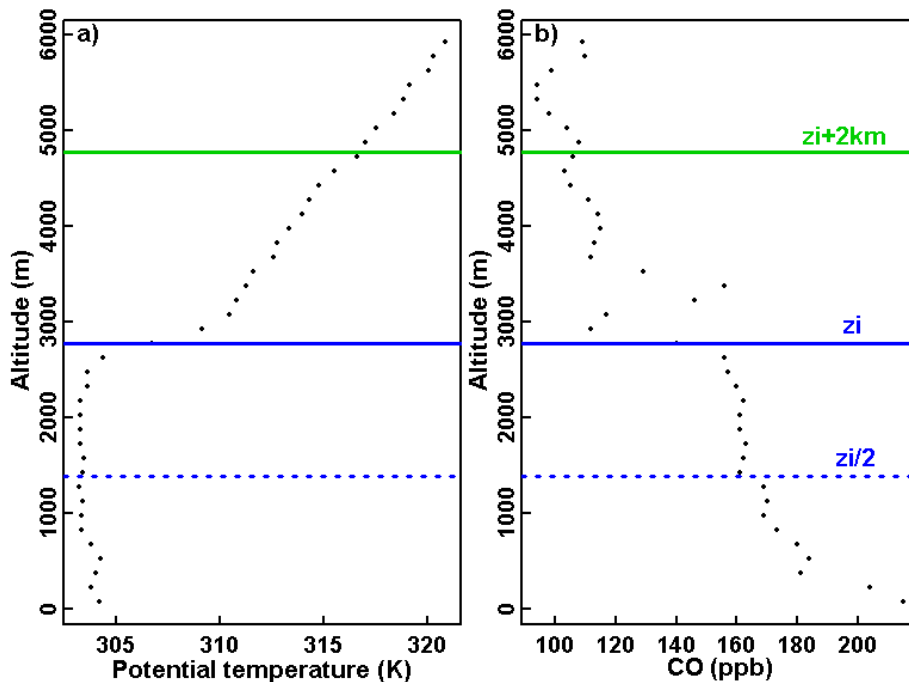


Figure 4.5. Illustration of the concept of CO enhancement using the CO and potential temperature profiles: a) the potential temperature profile; b) the CO profile. The solid blue line specifies the PBL height; the dashed blue line indicates half the PBL height; the solid green line points out the level 2km above the PBL height.

The distribution of average CO enhancements for the lower half and the upper half of the PBL is shown in Fig. 4.6. The average enhancement is 112 ppb for the lower half and 75 ppb for the upper half. It can be seen from the figure that the maximum in the distribution for the upper half of the PBL occurs at smaller CO enhancements than for the lower half of the PBL. The fraction of CO enhancements larger than 100 ppb for the lower half of the PBL (~ 41.1%) is significantly larger than that for the upper half of the PBL (~ 21.6%). The maximum values for both cases are close, between 600 ppb and 650 ppb. Note that 0.7% of value for the upper half of the PBL are negative value, indicating a CO inversion in those profiles.

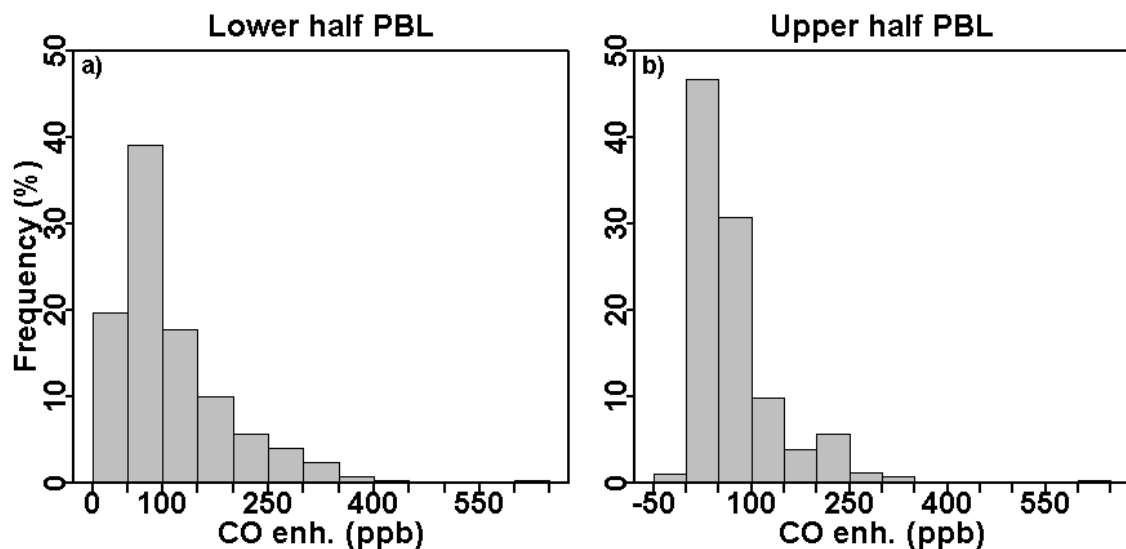


Figure 4.6 Distribution of average CO enhancements of the lower half (a) and the upper half (b) of the PBL for daytime profiles over Frankfurt during the period 2002-2004, binned in 50 ppb intervals. There are fewer observations in the lower half of the PBL (299) than the upper half of the PBL (407) due to delayed start or early shut down of CO measurements during take-off or landing.

#### **4.2.2 Representativeness of CO profiles over Frankfurt**

In order to investigate whether future CO<sub>2</sub> profiles from a commercial airliner program are regionally representative and thus suitable for carbon cycle studies, the CO profiles over Frankfurt are assessed as a proxy for the contribution of fossil fuel emissions to CO<sub>2</sub>. For this, the observations are combined with a regional modeling framework for atmospheric CO and CO<sub>2</sub>. The modeling framework allows one to change the spatial resolution of surface fluxes, which is employed here to specifically to assess representativeness. Gerbig et al. (2003a and b) have shown using multiple aircraft profiles that at least in the case of CO<sub>2</sub>, spatial representativeness is dominated by small spatial scale variations in surface fluxes, and that the impact of those variations on the spatial representativeness of atmospheric CO<sub>2</sub> measurements can be simulated using different flux resolutions.

For model simulations, only daytime (UTC 11:00-17:00) profiles are selected for the assessment because model comparison studies (Geels et al., 2007) suggest that daytime observations can be better represented by models while nighttime observations are generally underestimated.

##### **4.2.2.1 Modeling framework**

The representativeness of CO profiles over Frankfurt is assessed using the stochastic time-inverted Lagrangian transport (STILT) model (Lin et al., 2003) coupled with high-resolution emissions. The STILT model was developed based on the HYSPLIT model (Draxler et al., 1998). It employs a source-receptor concept (see Fig.4.7), where the

mixing ratios of trace gases at a measurement location (receptor) are calculated from the upstream surface fluxes (source) weighted by the strength of the influence (also called footprint).

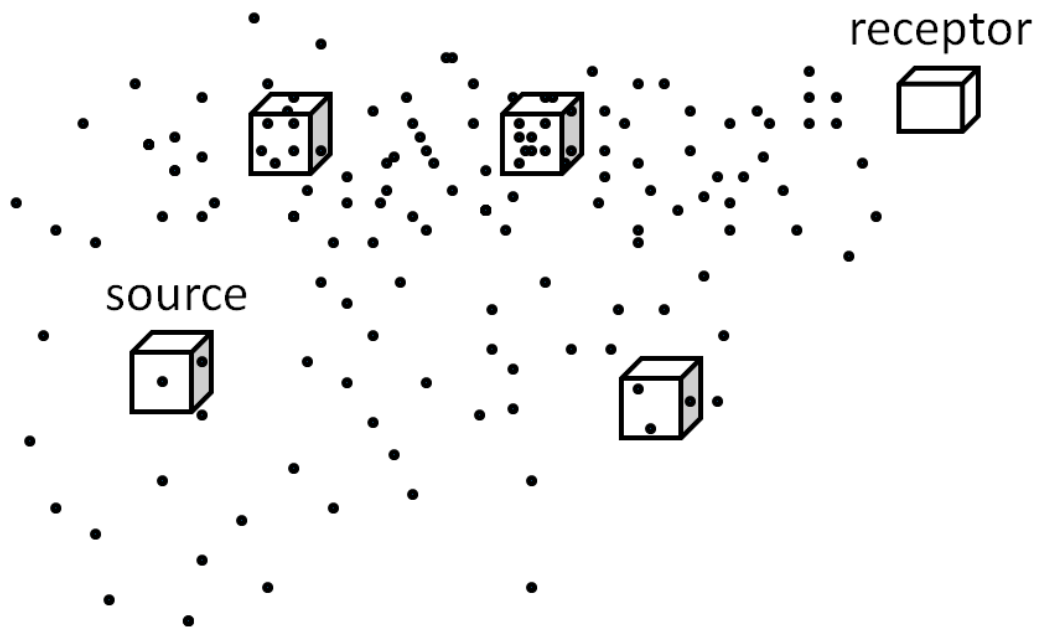


*Figure 4.7 Illustration of simulations of the STILT model: the area with dots is the influencing area for the receptor and the density of dots in the source boxes denotes the strength of fluxes.*

To implement the STILT model for the European domain, three-hourly averaged short-term forecasted meteorological data from the European Center for Medium-Range Weather Forecasts (ECMWF) model are used (Gerbig et al., 2008). Simulation of CO concentration consists of two parts: the influence from CO emissions within the model domain and the contribution from the initial boundary values. The influence of CO emissions on the mixing ratio at the receptor can be derived by multiplying the so-called footprint calculated by STILT with corresponding surface fluxes. The dominant surface fluxes for CO are from fossil fuel burning, which are obtained from the high-resolution

emission inventory from the Institute of Economics and the Rational Use of Energy (IER), University of Stuttgart (<http://carboeurope.ier.uni-stuttgart.de/>). The inventory contains hourly emission of greenhouse gases for the year 2000 at a spatial resolution of 10 km for European countries. These data are adapted by taking into account the shift in weekdays between the years 2000 and 2004 so that the temporal emission patterns (weekends versus weekdays) are retained. Instead of using CO fields from a global model, for simplicity we use a zero lateral boundary condition, and compare only the simulated CO enhancements within the PBL to the measured enhancements to assess how well these observations can be represented by the STILT model.

The simulations were done for all daytime profiles in 2004, for a total of 182 profiles. The footprints were generated using STILT at a resolution of 10 km. The simulated CO enhancements were calculated in the same way as the observed ones, i.e. PBL values subtracting 2 km above the PBL height; however, the simulated PBL heights were used for the calculations, rather than those derived from measurements. The simulated CO enhancements are divided into upper half and lower half of the PBL, and mean values of each are calculated. The average footprints for the lower half and the upper half of the PBL are shown in Fig. 4.8. The average footprints in the whole European domain (Fig.4.8a and b) for both the upper half and the lower look similar and show that observations are mainly influenced by surface fluxes in the central and west Europe; however, the footprints near Frankfurt (Fig.4.8c and d) indicate that the airport and the city of Frankfurt have a stronger influence on the lower half of the PBL than on the upper half of the PBL.

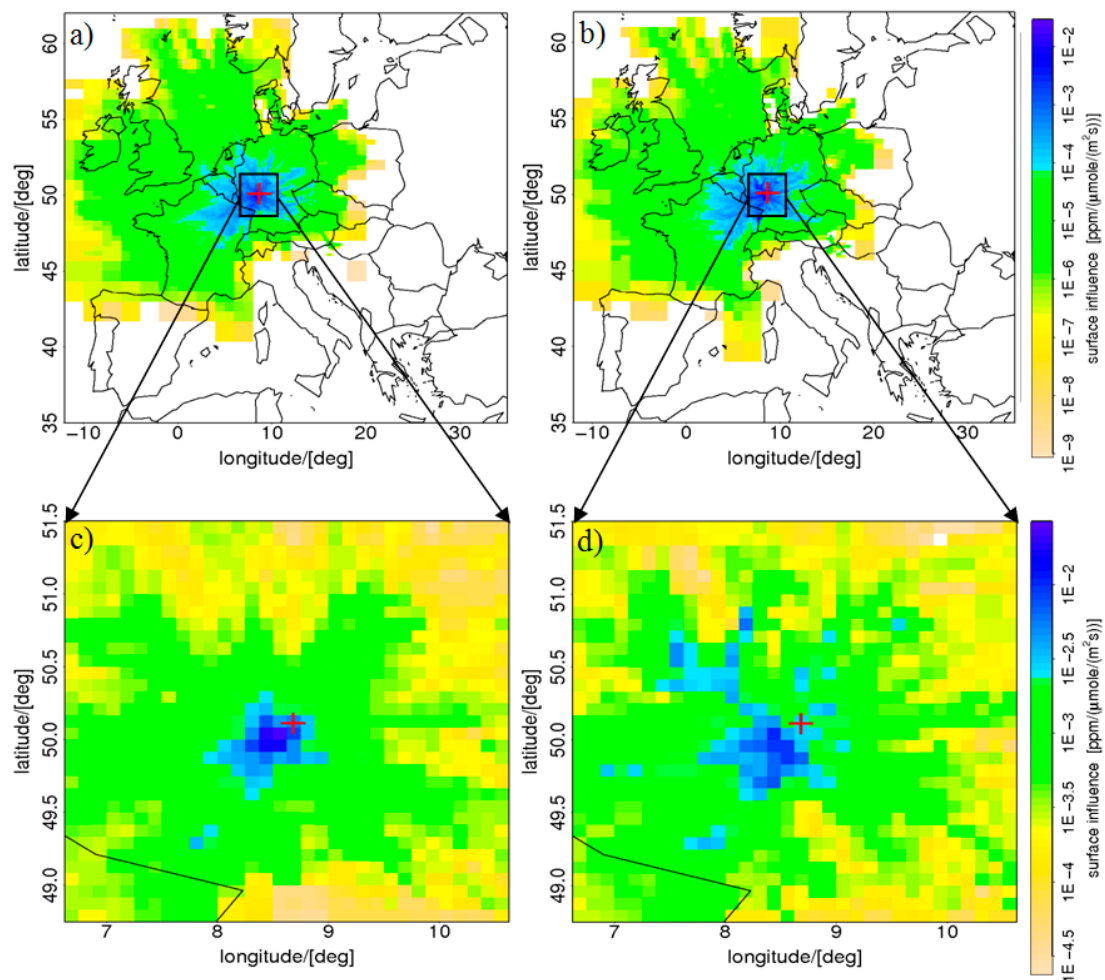


Figure 4.8 Average footprints for the European domain for the lower half (a) and the upper half (b) of the PBL for daytime observations over Frankfurt in 2004; the footprints are zoomed in for the lower half (c) and the upper half (d) of the PBL. The symbol of plus in the figure indicate the location of the city of Frankfurt. These footprints are derived from particle locations generated by STILT between -24 and 0 hours.

#### 4.2.2.2 Modeling results

The comparison of observed and simulated CO enhancements (Fig 4.9) shows that the model captures a significant part of the observed variability, with R-squared values of 0.45 for the lower half of the PBL and 0.43 for the upper half of the PBL. However the slopes of the regression between the observations and the simulations are 0.51 for the

lower half of the PBL and 0.37 for the upper half of the PBL, far smaller than 1, indicating that the model underestimates the values for both cases. The reason for the underestimation is discussed in the following section.

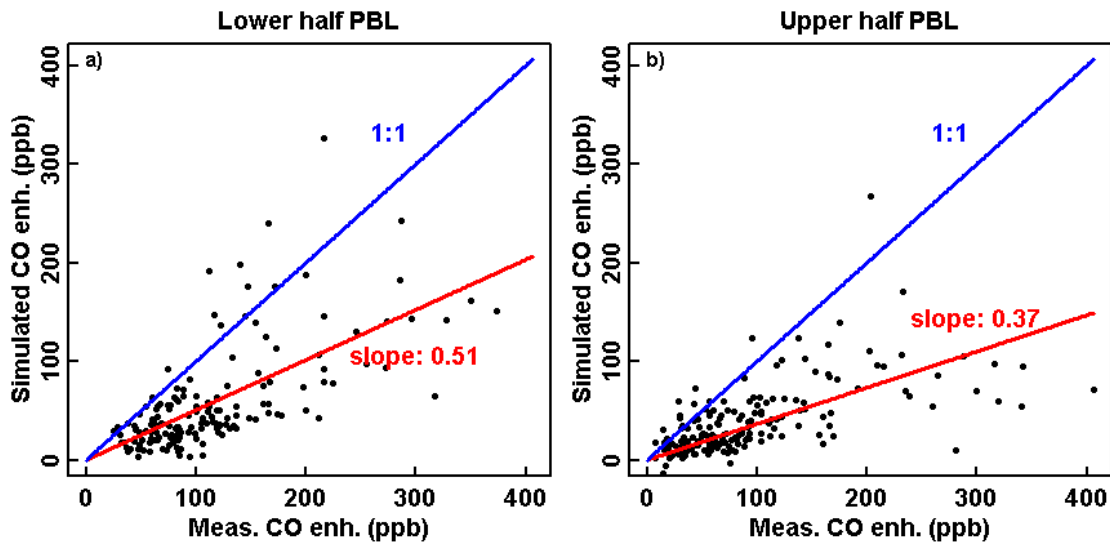


Figure 4.9. Comparisons between observed and simulated CO enhancements from daytime profiles over Frankfurt in 2004 for the lower half of the PBL (a) and for the upper half of the PBL (b). The blue line indicates 1:1 and the red line shows the linear fit. The R-squared values are 0.45 for the lower half of the PBL and 0.43 for the upper half of the PBL.

Further, STILT was run at resolutions of 20 km, 40 km, 80 km, 160 km and 320 km to examine the dependence of simulations on spatial scales. Note that the trajectory ensembles calculated by STILT are not dependent on the resolutions; only the fluxes are aggregated when coarser resolutions are employed. The comparisons between observed and simulated CO enhancements at different resolutions are shown in Table 4.1 for the lower half of the PBL and Table 4.2 for the upper half of the PBL. The results show that the slopes for the lower half of the PBL decrease with model resolution, while the slopes for the upper half of the PBL do not change with model resolution up to 80 km. Only at scales larger than 80 km do both slopes decrease.

Table 1. Comparisons between observed and STILT simulated **lower** half PBL average CO enhancements at different resolutions.

STILT resolutions (km)	R-squared	Slopes of linear fits*	Standard deviation of Residuals (ppb)	Obs. mean (ppb)	Standard deviation of Obs. (ppb)	Model mean (ppb)	Standard deviation of Model (ppb)
10km	0.45	0.51±0.02	39.9	113.2	69.1	57.5	53.1
20km	0.47	0.46±0.02	33.5	113.2	69.1	53.1	45.2
40km	0.49	0.38±0.01	24.9	113.2	69.1	43.9	34.5
80km	0.50	0.38±0.02	25.6	113.2	69.1	44.4	34.9
160km	0.49	0.32±0.01	20.7	113.2	69.1	38.1	28.0
320km	0.48	0.30±0.01	19.2	113.2	69.1	35.6	26.0

\* the slopes are for a linear model with zero intercept.

Table 2. Comparisons between observed and STILT simulated **upper** half PBL average CO enhancements at different resolutions

STILT resolutions (km)	R-squared	Slopes of linear fits*	Standard deviation of Residuals (ppb)	Obs. mean (ppb)	Standard deviation of Obs. (ppb)	Model mean (ppb)	Standard deviation of Model (ppb)
10km	0.43	0.37±0.02	25.9	88	66.1	36.8	34.2
20km	0.42	0.37±0.02	26.8	88	66.1	37.1	35.1
40km	0.41	0.36±0.02	25.4	88	66.1	36.2	33.1
80km	0.47	0.37±0.02	24.9	88	66.1	37.5	34.1
160km	0.45	0.33±0.02	21.2	88	66.1	34.1	28.6
320km	0.47	0.31±0.01	19.3	88	66.1	32.3	26.5

\* the slopes are for a linear model with zero intercept.

The most obvious discrepancy between model and observation is that the model underestimates the CO enhancements for all resolutions and for both the upper and lower half of the PBL. To assess whether this bias is caused by local pollution underestimated in the emission inventory, a clean sector among the upper half of the PBL has been



selected based on two factors: 1) the distances between the observations and both the airport and the city of Frankfurt are larger than 15 km; 2) the observations are located upwind of the airport and the city of Frankfurt. The comparison of observed and simulated CO enhancements from the clean sector reveals that the slope of the linear fit is 0.37, indicating the model is still underestimating the CO enhancements by a factor of 2.7. This shows that the underestimation by the model is not caused by local pollution.

To assess the spatial representation error of fossil fuel CO<sub>2</sub>, the differences of simulated CO enhancements from the high-resolution run (10 km fossil fuel emission fluxes) and from degraded runs (from 20km to 320km) are calculated. The spatial representation errors for CO over Frankfurt are calculated as the standard deviations of these differences for the different resolved grid scales of the degraded runs for the lower half and the upper half of the PBL. The spatial representation errors of fossil fuel CO<sub>2</sub> are then obtained from the spatial representation errors of CO divided by the inventory-based CO/CO<sub>2</sub> ratios (Fig. 4.10). The representation error of the lower half of the PBL over Frankfurt increases significantly with model scales. Starting from 40 km, the representation error for the upper half of the PBL is a factor of two smaller than that of the lower half of the PBL. The representation error for BIK will be discussed in Chapter 4.3.

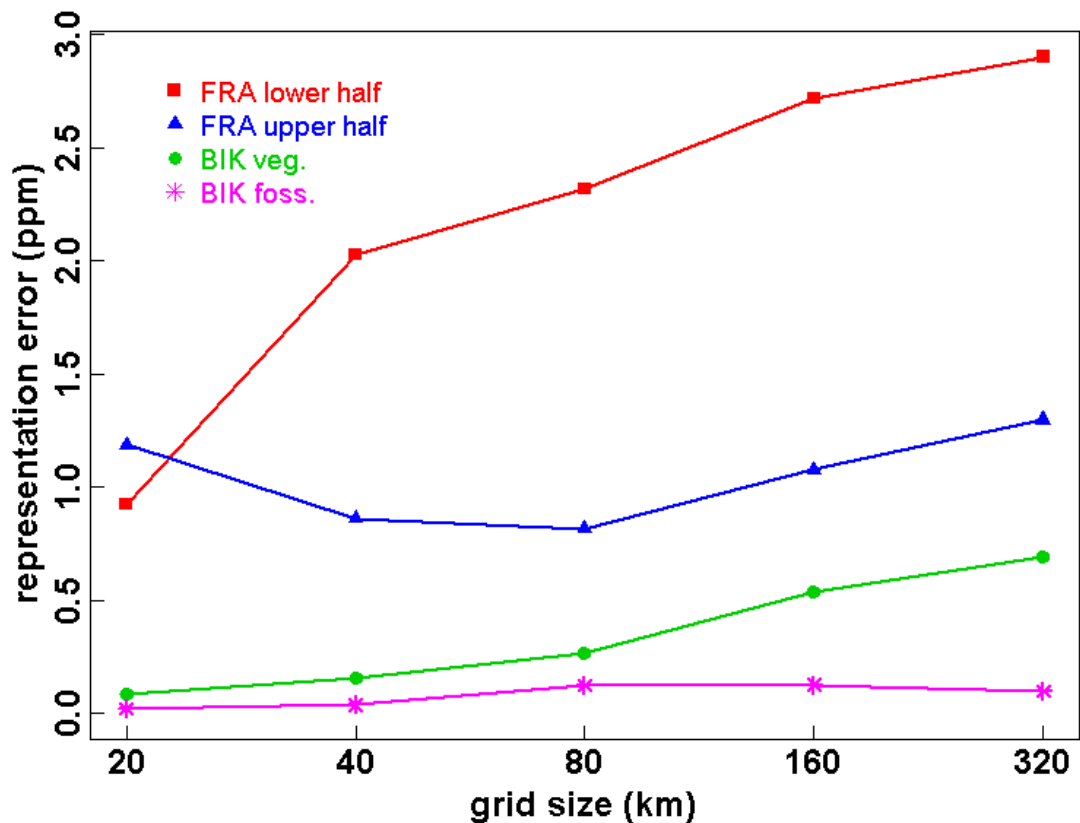


Figure 4.10. Representation error of fossil fuel CO<sub>2</sub> for the lower half (red square) and the upper half (blue triangle) of the PBL over Frankfurt, calculated as the representation error of CO enhancements divided by the inventory-based emission ratio of CO/CO<sub>2</sub>. The representation error of biospheric CO<sub>2</sub> (green circle) and fossil fuel CO<sub>2</sub> (magenta star) at the reference site BIK are also shown. Note that for fossil fuel CO<sub>2</sub> from profiles over FRA, these values will be a factor of 1 to 2.7 larger when fossil fuel CO<sub>2</sub> fluxes are optimized; for fossil fuel CO<sub>2</sub> from profiles near BIK, the representation error will be a factor of 1 to 2.1 larger when fossil fuel CO<sub>2</sub> fluxes are optimized.

#### 4.2.2.3 Discussion

Given the fact that the CO emissions are much higher near the airport and the city of Frankfurt than in other areas in this region (Fig. 4.4), the decrease of the slopes for the lower half of the PBL (Table 4.1) suggests that these observations are influenced by local fossil fuel CO emissions. On the contrary, the observations from the upper half of the

PBL (Table 4.2) seem not influenced by local fossil fuel CO emissions at scales between 10 and 80 km, as indicated by the lack of a change in the slope with increasing resolution. Similarly, the representation error of fossil fuel CO<sub>2</sub> of the lower half of the PBL increases with model scales, while that of the upper half of the PBL does not increase from 20 km to 80km, and only increase from 80 km to 320 km. These results all suggest that those observations from the upper half of the PBL are more representative for regional scales up to 80 km.

Two issues need to be addressed before these observations are used for regional carbon flux studies or validating measurements from remote sensing techniques: the obvious underestimation of modeled CO within the PBL, which is potentially associated with an underestimation of fossil fuel CO<sub>2</sub>; the estimation of the actual total error caused by fossil fuel CO<sub>2</sub>, which will be derived from residual differences between modeled and measured CO enhancements.

The underestimation of CO enhancements could be caused by different aspects: deficiencies in the model setup, transport uncertainties, or missing emission sources. All of these will be addressed in the following.

To assess if deficiencies in the model setup could be responsible for the underestimation, the sensitivity of the observed CO enhancements on the choice of free troposphere CO concentration is examined. Instead of using the CO values at 2km above the PBL height, the CO enhancements are calculated as PBL values subtracting the CO values at 1km above the PBL. A comparison between the CO enhancements that are calculated relative

to values at 1km and 2km above the PBL height shows that the relative difference is smaller than 8% for both the lower and upper half of the PBL and is far from explaining the underestimation of a factor of 2.7.

Further, the model setup employs zero lateral boundaries, and thus any vertical gradients in the simulated CO profiles due to advection of boundary fields of CO are missing. The STILT simulations show that most of the particles exit the domain to the west (54%) and to the north (32%). Small fractions of particles leave the domain to the south (5%) and to the east (4%). Most of the remainder (5%) stay inside the European domain during the 15 days backward simulations. The boundaries are mainly Oceans, where the vertical CO gradients are small, especially when compared to the gradients observed over Frankfurt. Therefore, this cannot be the reason for the underestimation.

Next, uncertainties in transport as represented by the model are investigated. Vertical mixing plays an important role in the model simulations. To assess how well the vertical mixing is represented by the model, a comparison between the observed PBL heights and the modeled PBL heights over Frankfurt is made. The simulated PBL heights are about 20% lower than the observed ones. The underestimation of the PBL heights means that the model could have accumulated more CO emissions in the PBL and derived larger CO enhancements, but the comparisons between the observed and simulated CO enhancement show the offset in the opposite direction. Thus if one compensates for the 20% weaker vertical mixing in the model results, the underestimation is even more severe. This rules out the uncertainties in PBL mixing as a cause.

A further potential uncertainty in transport is related to the subgrid-parameterization of convective transport in cloud systems. A possibility for explaining the underestimation by the model is that the model has overestimated the amount of convective vertical transport into the free troposphere, causing smaller CO gradients between the PBL and the free troposphere. A simple test has been done to rerun the simulations with the convection module of the model turned off. Indeed, the slope of the comparison between the observed and simulated CO enhancement for upper half of the PBL increased from 0.37 to 0.42 when turning convection off. Thus convection reduces the enhancement by about 13%, but by far not enough to explain the difference of a factor of 2.7. Furthermore, convection is an intrinsic part of transport and thus should be included in the transport model. Therefore, the underestimation of CO enhancements cannot be explained by too much convection in the model.

Missing natural CO sources in the model, such as biomass burning, oxidation of CH<sub>4</sub> and non-methane volatile organic carbons (VOCs) could potentially cause a bias in the simulations. According to the footprints shown in Fig. 4.8, the area of influence for the simulations over Frankfurt is mainly in central and western Europe, and thus the contribution of the biomass burning CO signal is not significant. The CO emissions due to oxidation of CH<sub>4</sub> and non-methane VOCs may have some influence on observations made in summer, but little influence on those made in winter (Potosnak et al., 1999). The comparison of observed and simulated CO enhancements in winter reveals that the slope of the linear fit is comparable to the one when all data are used, indicating that the missing sources due to oxidation of CH<sub>4</sub> and non-methane VOCs are not the reason for the underestimation by the model. The potential sinks are from deposition of CO on the

surface and photochemical processes; however, the contributions of these sinks to the simulations are not significant since the simulation period is relatively short when compared to the lifetime of CO.

The underestimation of CO enhancements could potentially be explained by an underestimation of fossil fuel CO emissions. In the CO emission inventory, e.g. IER, emission fluxes are estimated based on the statistics of fossil fuel use and the ratio of CO/CO<sub>2</sub>(foss). On the national scale, there is ~5% uncertainty in the statistics of fossil fuel use (Andres et al., 1996); however, the uncertainty increases significantly for smaller spatial scales due to strong variations of emission fluxes. The ratio of CO/CO<sub>2</sub>(foss) varies for different types of combustion and thus may be space and time dependent. Therefore, the model underestimation is likely caused by the underestimation of fossil fuel CO emissions in the inventory.

For the second issue, the estimation of the actual total uncertainty caused by fossil fuel CO<sub>2</sub> is derived from residual differences between modeled and measured CO enhancements. This uncertainty in fossil fuel CO<sub>2</sub> depends on the cause of the underestimation of the emission inventory: either both fossil fuel CO and CO<sub>2</sub> are underestimated or the ratio of CO/CO<sub>2</sub> is underestimated. In the first case, the uncertainty in fossil fuel CO<sub>2</sub> will be amplified when fossil fuel CO<sub>2</sub> fluxes are scaled up to match the observations. However, in the second case, only the ratio needs to be scaled up and the uncertainty in fossil fuel CO<sub>2</sub> is not affected. It is likely that the underestimation of the emission inventory is caused by both of the above-mentioned causes. Therefore, the estimated total uncertainty needs to be scaled up by a factor of 1 to 2.7 depending on the

causes. In the following discussion, the lower limit of the total uncertainty is derived based on the residual differences and inventory-based CO/CO<sub>2</sub> ratios, and then a factor of 2.7 is applied to obtain the upper limit (see Table 4.3).

The total uncertainty of the CO enhancements of the lower half and the upper half of the PBL at the resolution of 10 km is estimated to be 25.9 ppb and 39.9 ppb (see Table 4.2). Given a mean CO/CO<sub>2</sub>(foss) ratio of 12.6 ppb/ppm (calculated from the simulated fossil fuel CO and CO<sub>2</sub> by STILT for the upper half of the profiles using the IER emission inventory), the total uncertainty for fossil fuel CO<sub>2</sub> components is anticipated to be 3.0 – 8.1 ppm for the lower half and 2.1 – 5.7 ppm for the upper half of the PBL, which are comparable to the prior uncertainty in biospheric fluxes of 2 – 8 ppm (P. Peylin, personal communication, 2008). The total uncertainty for fossil fuel CO<sub>2</sub> components in summer only is estimated to be 1.6 – 4.3 ppm for the lower half of the PBL and 1.2 – 3.2 ppm for the upper half of the PBL, which is smaller than the uncertainty in transport models of ~5 ppm due to advection for summer time (Gerbig et al., 2008). Note that total uncertainty includes transport error as well, and thus is the upper bound of the uncertainty caused by fossil fuel CO<sub>2</sub>.

The underestimation of CO enhancements by the model implies underestimation of CO<sub>2</sub> fossil fuel signals. In standard inverse studies for CO<sub>2</sub> (Roedenbeck et al., 2003; Baker et al., 2006), the fossil fuel CO<sub>2</sub> components are regarded as known a-priori and are subtracted from the CO<sub>2</sub> observations before the fluxes are optimized. The reason for doing this is that the inversions cannot distinguish between fossil fuel CO<sub>2</sub> signals and the respired CO<sub>2</sub> from the biosphere over land. The CO<sub>2</sub> and CO correlations have been

employed to improve inverse analyses of carbon fluxes (Palmer et al., 2006; Wang et al., 2009). With the additional information about the fossil fuel emissions provided by CO observations, a joint CO<sub>2</sub>-CO inversion is expected to improve the inversions, especially when the fossil fuel CO<sub>2</sub> component is significant.

### **4.3 Representativeness analysis of CO/CO<sub>2</sub> profiles from a remote site**

The representativeness of CO/CO<sub>2</sub> profiles from a remote site, Bialystok, Poland is assessed. As introduced in Chapter 4.1, first the variability of in situ CO<sub>2</sub> profiles is investigated to provide an estimate of observed representation error for the scale of 20 km near this site. The detailed information about these profiles is given in Chapter 3.3. Furthermore, the representativeness analysis for regular CO and CO<sub>2</sub> flask measurements that were made in 2006 and 2007 is performed. This study provides a reference for assessing the representativeness from a commercial airliner program because the potential influence of local fossil fuel emissions on observations at a remote site is expected to be insignificant.

#### **4.3.1 Spatial variability of mixed-layer CO<sub>2</sub> averages**

Since August 2008, one ascending profile and one descending profile have been collected during each flight (see Fig. 3.9) near Bialystok, which provides an opportunity to assess the spatial variability of mixed-layer CO<sub>2</sub> averages based on observations. The profiles are made every one to three weeks, around mid-day under fair weather conditions. The ascending profiles are usually made in about one hour over a national park that is about 17 km northwest of the city of Bialystok, while the descending profiles are typically completed in only 10 minutes over a mixture of forest and cultivated land about 20 km



away on the other side of the city of Bialystok. The descending profiles are always made after the ascending profiles, roughly 50 minutes later (the average time difference between the time when the ascending and the descending profiles are carried out).

The PBL heights are determined from the potential temperature profiles using the parcel method (Seibert et al., 2000). The mixed-layer average CO<sub>2</sub> concentration for each profile,  $\overline{CO_2}$ , is calculated as the mass weighted average, excluding the bottom 10% and the top 20% of the mixed layer to avoid the influence of both the surface layer at the bottom and the entrainment zone at the top. The differences of mixed-layer CO<sub>2</sub> averages between the ascending and the descending profiles are shown in Fig. 4.11, separated as the part of the growing season with peak carbon uptake (June, July, and August) and the rest of the growing season (April, May, and September), hereafter referred to as the peak growing season and the non-peak growing season, respectively. The uncertainty of the mixed-layer averages for each profile is estimated based on the method employed in Gerbig, et al. 2003. The uncertainty ranges from 0.04 to 0.41 ppm for individual profiles. The uncertainty of the differences is the square root of the sum of variances of the ascending and the descending profiles.

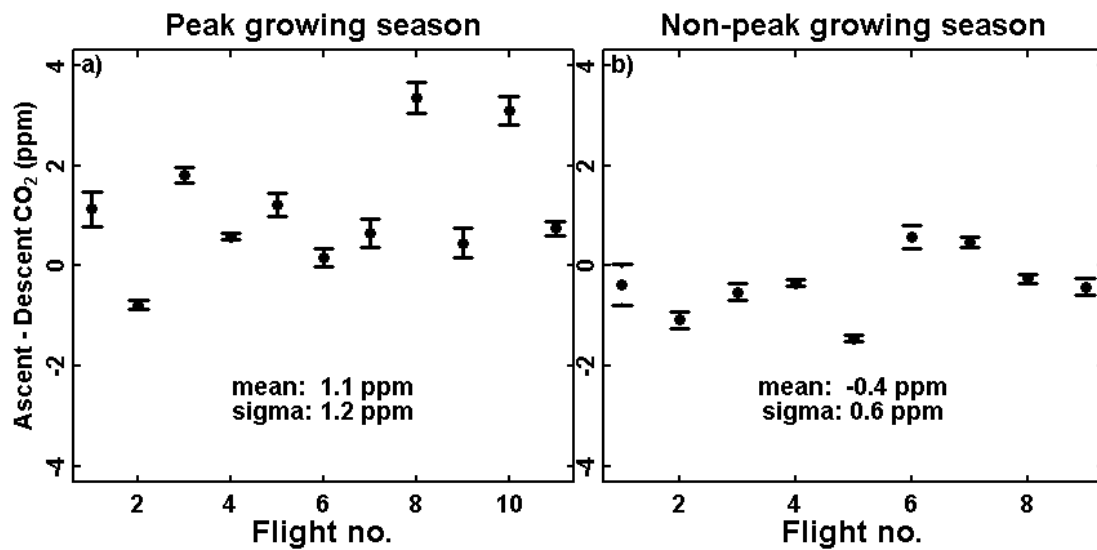


Figure 4.11. Differences of mixed-layer CO<sub>2</sub> averages between the ascending and the descending profiles near Bialystok: a) for the profiles made during the peak growing season; b) for the profiles made during the non-peak growing season. The data were collected during 2008 and 2009.

The differences of mixed-layer CO<sub>2</sub> averages between the ascending and the descending profiles during the peak growing season are significantly larger than 0 ppm (t-test p-value 0.006), while for the non-peak growing season they are not significantly different from 0 ppm (t-test p-value 0.115). The differences of mixed-layer CO<sub>2</sub> averages could have resulted from two main factors: the spatial variability and the time-dependant variation due to CO<sub>2</sub> sources or sinks on the surface. In the peak growing season, CO<sub>2</sub> is depleted in the mixed layer due to the uptake by vegetation, and as a result, the mixed-layer CO<sub>2</sub> average during ascending is higher than the mixed-layer CO<sub>2</sub> average during descending made roughly 50 minutes later. The average CO<sub>2</sub> uptake rate in Jun-Sep between LT 10:00 and 15:00 is estimated to be 0.24 ppm/50 min based on tower observations (Popa et al., 2010), which is much smaller than the mean difference of 1.1 ppm during the peak growing season. Note that the aircraft profiles were made during days with good weather,

and this fair weather bias might give an explanation why the differences are larger than the average CO<sub>2</sub> uptake rate. The spatial representation error calculated as the variability of the differences of the mixed-layer average CO<sub>2</sub> is 1.2 ppm during the peak growing season, which is larger than that during the non-peak growing season, 0.6 ppm.

### **4.3.2 Representativeness of aircraft CO/CO<sub>2</sub> profiles**

In situ CO aircraft profiles are not available; however, both CO and CO<sub>2</sub> mixing ratios have been obtained from the analysis of air samples in the flasks taken during regular profiling. These regular CO/CO<sub>2</sub> profiles are employed to assess the representativeness for this site.

#### 4.3.2.1 Modeling framework

The modeling framework for simulations of CO is established in a way similar to that described in Chapter 4.2.2, using the same meteorological fields, the same emission inventory, and the same European domain. The simulations are performed for daytime (UTC 11:00 –UTC 17:00) CO flask measurements in 2006 and 2007. The observed CO enhancements are calculated as the CO values within the PBL subtracting the average CO value between the PBL height and the highest available altitude of 2500 m. The simulated CO enhancements are computed in the same way, but using the simulated PBL height. For both observed and simulated CO enhancements, the average CO enhancements within the whole PBL are derived and used for comparison. Here the PBL is not divided into the lower half and the upper half because the profiles were made over a national park and no contamination by local fossil fuel emissions is expected.

For simulations of CO<sub>2</sub> at this site the diagnostic biosphere flux model VPRM (Vegetation Photosynthesis and Respiration Model) (Mahadevan et al., 2008) is coupled with the STILT model, driven by ECMWF meteorological fields for the European domain. VPRM estimates the values of Net Ecosystem Exchange (NEE) of CO<sub>2</sub> based on the reflectance data from the Moderate Resolution Imaging Spectroradiometer (MODIS) aboard the NASA Terra and Aqua satellites. The fossil fuel CO<sub>2</sub> emissions are taken from the IER inventory. The CO<sub>2</sub> mixing ratio is represented in the model as a sum of different components:

$$CO_2 = CO_{2,background} + CO_{2,fossil\ fuel} + CO_{2,photosynthetic\ uptake} + CO_{2,respiration} \quad (4.1)$$

Here CO<sub>2,background</sub> is the contribution from the lateral boundary fields obtained from the TM3 global transport model (Roedenbeck et al., 2003; Roedenbeck 2005); CO<sub>2,photosynthetic uptake</sub> and CO<sub>2,respiration</sub>, are uptake and release of CO<sub>2</sub> by plants generated by VPRM. The biospheric signal  $\Delta CO_{2,bio}$  can be calculated as

$$\Delta CO_{2,bio} = CO_2 - CO_{2,background} - CO_{2,fossil\ fuel} \quad (4.2)$$

Observation-based  $\Delta CO_{2,bio}$  can be obtained when CO<sub>2</sub> in Eq. 4.2 is from observations. The model was run for both CO and CO<sub>2</sub> first at a resolution of 10 km. Further, the model was run at resolutions of 20 km, 40 km, 80 km, 160 km and 320 km.

#### 4.3.2.2 Results and discussion

The comparison between observed and simulated average CO enhancements in the PBL for the flask measurements in 2006 and 2007 shows that the slope of a linear fit is 0.46, indicating that the model is underestimating the CO enhancements. The R-squared value

is 0.27. Referring to the discussion for the underestimation of CO enhancements over Frankfurt (Chapter 4.2), this underestimation is also likely due to an underestimation of the emission inventory.

The representation errors of fossil fuel and biospheric CO<sub>2</sub> are calculated and shown in Fig. 4.10. They are estimated based on the differences of CO enhancements and biospheric CO<sub>2</sub> from the high-resolution run (10 km fossil fuel emission fluxes) and from degraded runs (from 20km to 320km). The results show that the representation error of fossil fuel CO<sub>2</sub> at BIK is smaller than 0.2 ppm at all scales. The representation error of fossil fuel CO<sub>2</sub> for both the lower half and the upper half of the PBL profiles over Frankfurt is larger than the representation error of fossil fuel and biospheric CO<sub>2</sub> at BIK. The total uncertainty of CO enhancements, calculated as the standard deviation of the residual differences, is 15 ppb. Given the mean CO/CO<sub>2</sub>(foss) ratio of 22.9 ppb/ppm for this particular site (calculated from the simulated fossil fuel CO and CO<sub>2</sub> by STILT using the IER emission inventory) and the underestimation of fossil fuel CO<sub>2</sub> fluxes by a factor of 2.1, the total uncertainty for CO enhancements implies an total uncertainty of 0.7 – 1.4 ppm for fossil fuel CO<sub>2</sub>.

Table 4.3. Comparison of representation error and total uncertainty for fossil fuel CO<sub>2</sub> within the PBL of profiles over Frankfurt (FRA) and for fossil fuel and biospheric CO<sub>2</sub> within the PBL of profiles near Bialystok (BIK)

	<b>Representation error of fossil fuel CO<sub>2</sub> at 80km (ppm)</b>	<b>Total uncertainty of fossil fuel CO<sub>2</sub> at 10km (ppm)</b>	<b>Representation error of biospheric CO<sub>2</sub> at 80 km (ppm)</b>	<b>Total uncertainty of biospheric CO<sub>2</sub> at 10km (ppm)</b>
<b>FRA lower half</b>	2.3 – 6.2	3.0 – 8.1	–	–
<b>FRA upper half</b>	0.8 – 2.2	2.1 – 5.7	–	–
<b>FRA lower half (summertime)</b>	1.0 – 2.7	1.6 – 4.3	–	–
<b>FRA upper half (summertime)</b>	0.3 – 0.8	1.2 – 3.2	–	–
<b>BIK</b>	0.1 – 0.2	0.7 – 1.4	0.3	3.8

The total and biospheric CO<sub>2</sub> for both observed and simulated CO<sub>2</sub> PBL average are shown in Fig.4.12. The observation-based biospheric CO<sub>2</sub> is calculated from Eq. 4.2 using observed CO<sub>2</sub>. The seasonal variation is well captured by the simulations, with an R-squared value of 0.71; however, discrepancies are obvious at smaller scales. The total uncertainty of biospheric CO<sub>2</sub> signals, estimated as the standard deviation of the residual differences from a linear fit between simulated and observed biospheric CO<sub>2</sub>, is 3.8 ppm. This total uncertainty of biospheric CO<sub>2</sub> is much larger than the total uncertainty of fossil fuel CO<sub>2</sub> (0.7 – 1.4 ppm) at the same site (see Table 4.3). The total uncertainties of fossil fuel CO<sub>2</sub> over Frankfurt are comparable to the total uncertainty of biospheric CO<sub>2</sub> at BIK; however, the total uncertainty of fossil fuel CO<sub>2</sub> for the upper half of the PBL for summertime is smaller than the total uncertainty of biospheric CO<sub>2</sub> at BIK. As mentioned above, this total uncertainty includes transport errors and thus should be regarded as the

upper bound of the uncertainty of biospheric CO<sub>2</sub>. These suggest that the upper half of the PBL over Frankfurt can be useful for carbon cycle studies to constrain biospheric fluxes. Again, a joint CO<sub>2</sub>-CO inversion is suggested to optimize both the fossil fuel CO<sub>2</sub> and biospheric CO<sub>2</sub> fluxes simultaneously for using the profiles from a commercial airliner program.

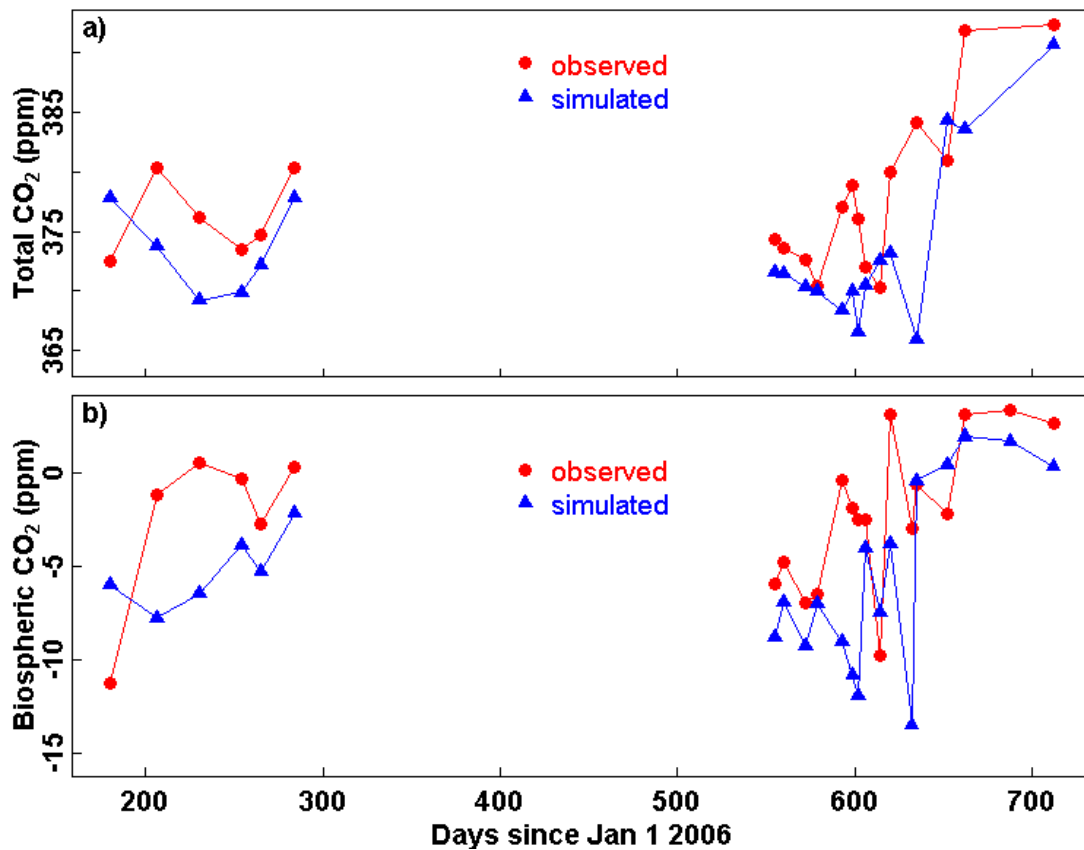


Figure 4.12 The temporal variations of total and biospheric CO<sub>2</sub> for both observed and simulated CO<sub>2</sub> PBL average from profiles over Bialystok in 2006 and 2007. The observed biospheric CO<sub>2</sub> is calculated as observed CO<sub>2</sub> subtracting the simulated initial value and fossil fuel CO<sub>2</sub>.

#### 4.4 Conclusions and discussion

The representativeness analysis of CO profiles over Frankfurt from a commercial airliner program shows that the measurements in the upper half of the PBL are regionally representative since the model simulations for these data do not depend on the model resolutions. The model is underestimating CO enhancements, which can only be explained by an underestimation of fossil fuel emissions in the inventory after excluding other potential causes, such as the model setup, transport uncertainties, or missing emission sources.

The representation error of fossil fuel CO<sub>2</sub> for profiles from Frankfurt is significantly larger than that at BIK at all scales, suggesting that a high-resolution model is required to represent the fossil fuel CO<sub>2</sub> over Frankfurt, while the observations at BIK are influenced little by fossil fuel. Moreover, the total uncertainty of fossil fuel CO<sub>2</sub> for the upper half of the PBL over Frankfurt for summer time (1.2 – 3.2 ppm) is smaller than the total uncertainty of biospheric CO<sub>2</sub> at BIK (3.8 ppm). This implies that the upper half of the PBL over Frankfurt can be useful for carbon cycle studies to constrain biospheric fluxes.

The representation error derived from the variability of the differences of the mixed-layer average CO<sub>2</sub> from profiles (20km apart) shows larger values (1.2 ppm during the peak growing season and 0.6 ppm during the non-peak growing season) than the representation error of fossil fuel (0.1ppm) or of biospheric CO<sub>2</sub> (0.3ppm) at the scale of 80 km, especially for the growing season. This suggests a larger variability of CO<sub>2</sub> near the city of Bialystok, either due to variations in fossil fuel or biospheric fluxes.



To deal with the unresolved variability of fossil fuel CO<sub>2</sub> from a commercial airliner program, a joint CO<sub>2</sub>-CO inversion is suggested. With the additional information about the fossil fuel emissions provided by CO observations, such a joint inversion is expected to be able to optimize both anthropogenic and biospheric CO<sub>2</sub> fluxes simultaneously. This is important for using observations at a continental site where fossil fuel CO<sub>2</sub> components are significant. Note that in this inversion scheme, a decent knowledge of the ratio of CO/CO<sub>2</sub>(foss) is required. The ratio can be validated when observations of <sup>14</sup>CO<sub>2</sub> are available (Hsueh et al., 2007; Levin et al., 2007; Turnbull et al., 2009). However, it is not realistic to have routine measurements of <sup>14</sup>CO<sub>2</sub> in the commercial airliner program since it requires air samples to be taken during flight and analyzed later in the laboratory. A good method is to estimate these ratios using the footprints calculated from a Lagrangian transport model multiplied with a reliable high-resolution CO/CO<sub>2</sub>(foss) inventory.

## 4.5 References

- Andres, R. J., G. Marland, I. Fung and E. Matthews (1996). "A 1 degrees x 1 degrees distribution of carbon dioxide emissions from fossil fuel consumption and cement manufacture, 1950-1990." Global Biogeochemical Cycles **10**(3): 419-429.
- Baker, D. F., R. M. Law, K. R. Gurney, P. Rayner, P. Peylin, A. S. Denning, P. Bousquet, L. Bruhwiler, Y. H. Chen, P. Ciais, I. Y. Fung, M. Heimann, J. John, T. Maki, S. Maksyutov, K. Masarie, M. Prather, B. Pak, S. Taguchi and Z. Zhu (2006). "TransCom 3 inversion intercomparison: Impact of transport model errors on the interannual variability of regional CO<sub>2</sub> fluxes, 1988-2003." Global Biogeochemical Cycles **20**(1).

- Draxler, R. R. and G. D. Hess (1998). "An overview of the HYSPLIT\_4 modelling system for trajectories, dispersion and deposition." Australian Meteorological Magazine **47**(4): 295-308.
- Engelen, R. J., A. S. Denning and K. R. Gurney (2002). "On error estimation in atmospheric CO<sub>2</sub> inversions." Journal of Geophysical Research **107**(D22): ACL10-1-ACL10-ACL10-13.
- Gammitzer, U., U. Karstens, B. Kromer, R. E. M. Neubert, H. A. J. Meijer, H. Schroeder and I. Levin (2006). "Carbon monoxide: a quantitative tracer for fossil fuel CO<sub>2</sub>?" Journal of Geophysical Research-Part D-Atmospheres **111**(D22): 1-19.
- Geels, C., M. Gloor, P. Ciais, P. Bousquet, P. Peylin, A. T. Vermeulen, R. Dargaville, T. Aalto, J. Brandt, J. H. Christensen, L. M. Frohn, L. Haszpra, U. Karstens, C. Rodenbeck, M. Ramonet, G. Carboni and R. Santaguida (2007). "Comparing atmospheric transport models for future regional inversions over Europe - Part 1: mapping the atmospheric CO<sub>2</sub> signals." Atmospheric Chemistry and Physics **7**(13): 3461-3479.
- Gerbig, C., S. Koerner and J. C. Lin (2008). "Vertical mixing in atmospheric tracer transport models: error characterization and propagation." Atmospheric Chemistry and Physics **8**(3): 591-602.
- Gerbig, C., J. C. Lin, S. C. Wofsy, B. C. Daube, A. E. Andrews, B. B. Stephens, P. S. Bakwin and C. A. Grainger (2003a). "Toward constraining regional-scale fluxes of CO<sub>2</sub> with atmospheric observations over a continent: 1. Observed spatial variability from airborne platforms." Journal of Geophysical Research-Atmospheres **108**(D24).
- Gerbig, C., J. C. Lin, S. C. Wofsy, B. C. Daube, A. E. Andrews, B. B. Stephens, P. S. Bakwin and C. A. Grainger (2003b). "Toward constraining regional-scale fluxes of CO<sub>2</sub> with atmospheric observations over a continent: 2. Analysis of COBRA data using a receptor-oriented framework." Journal of Geophysical Research-Atmospheres **108**(D24).
- Gurney, K. R., R. M. Law, A. S. Denning, P. J. Rayner, D. Baker, P. Bousquet, L. Bruhwiler, Y. H. Chen, P. Ciais, S. Fan, I. Y. Fung, M. Gloor, M. Heimann, K. Higuchi, J. John, T. Maki, S. Maksyutov, K. Masarie, P. Peylin, M. Prather, B. C. Pak, J. Randerson, J. Sarmiento, S. Taguchi, T. Takahashi and C. W. Yuen (2002). "Towards robust regional estimates of CO<sub>2</sub> sources and sinks using atmospheric transport models." Nature **415**(6872): 626-630.

- Henne, S., D. Brunner, D. Folini, S. Solberg, J. Klausen and B. Buchmann (2010). "Assessment of parameters describing representativeness of air quality in-situ measurement sites." Atmospheric Chemistry and Physics **10**(8): 3561-3581.
- Hsueh, D. Y., N. Y. Krakauer, J. T. Randerson, X. M. Xu, S. E. Trumbore and J. R. Southon (2007). "Regional patterns of radiocarbon and fossil fuel-derived CO<sub>2</sub> in surface air across North America." Geophysical Research Letters **34**(2).
- Levin, I. and U. Karstens (2007). "Inferring high-resolution fossil fuel CO<sub>2</sub> records at continental sites from combined (CO<sub>2</sub>)-C-14 and CO observations." Tellus Series B-Chemical and Physical Meteorology **59**(2): 245-250.
- Lin, J. C., C. Gerbig, B. C. Daube, S. C. Wofsy, A. E. Andrews, S. A. Vay and B. E. Anderson (2004). "An empirical analysis of the spatial variability of atmospheric CO<sub>2</sub>: Implications for inverse analyses and space-borne sensors." Geophysical Research Letters **31**(23).
- Lin, J. C., C. Gerbig, S. C. Wofsy, A. E. Andrews, B. C. Daube, K. J. Davis and C. A. Grainger (2003). "A near-field tool for simulating the upstream influence of atmospheric observations: The Stochastic Time-Inverted Lagrangian Transport (STILT) model." Journal of Geophysical Research-Atmospheres **108**(D16).
- Mahadevan, P., S. C. Wofsy, D. M. Matross, X. M. Xiao, A. L. Dunn, J. C. Lin, C. Gerbig, J. W. Munger, V. Y. Chow and E. W. Gottlieb (2008). "A satellite-based biosphere parameterization for net ecosystem CO<sub>2</sub> exchange: Vegetation Photosynthesis and Respiration Model (VPRM)." Global Biogeochemical Cycles **22**(2).
- Miller, C. E., L. R. Brown, R. A. Toth, D. C. Benner and V. M. Devi (2005). "Spectroscopic challenges for high accuracy retrievals of atmospheric CO<sub>2</sub> and the Orbiting Carbon Observatory (OCO) experiment." Comptes Rendus Physique **6**(8): 876-887.
- Nedelec, P., J. P. Cammas, V. Thouret, G. Athier, J. M. Cousin, C. Legrand, C. Abonnel, F. Lecoer, G. Cayez and C. Marizy (2003). "An improved infrared carbon monoxide analyser for routine measurements aboard commercial Airbus aircraft: technical validation and first scientific results of the MOZAIC III programme." Atmospheric Chemistry and Physics **3**: 1551-1564.
- Palmer, P. I., P. Suntharalingam, D. B. A. Jones, D. J. Jacob, D. G. Streets, Q. Y. Fu, S. A. Vay and G. W. Sachse (2006). "Using CO<sub>2</sub> : CO correlations to improve inverse analyses of carbon fluxes." Journal of Geophysical Research-Atmospheres **111**(D12).

- Pillai, D., C. Gerbig, J. Marshall, R. Ahmadov, R. Kretschmer, T. Koch and U. Karstens (2010). "High resolution modeling of CO<sub>2</sub> over Europe: implications for representation errors of satellite retrievals." Atmospheric Chemistry and Physics **10**(1): 83-94.
- Popa, M. E., M. Gloor, A. C. Manning, A. Jordan, U. Schultz, F. Haensel, T. Seifert and M. Heimann (2010). "Measurements of greenhouse gases and related tracers at Bialystok tall tower station in Poland." Atmos. Meas. Tech. **3**: 407-427.
- Potosnak, M. J., S. C. Wofsy, A. S. Denning, T. J. Conway, J. W. Munger and D. H. Barnes (1999). "Influence of biotic exchange and combustion sources on atmospheric CO<sub>2</sub> concentrations in New England from observations at a forest flux tower." Journal of Geophysical Research-Atmospheres **104**(D8): 9561-9569.
- Rayner, P. J., I. G. Enting, R. J. Francey and R. Langenfelds (1999). "Reconstructing the recent carbon cycle from atmospheric CO<sub>2</sub>, delta C-13 and O-2/N-2 observations." Tellus Series B-Chemical and Physical Meteorology **51**(2): 213-232.
- Roedenbeck, C. (2005). "Estimating CO<sub>2</sub> sources and sinks from atmospheric mixing ratio measurements using a global inversion of atmospheric transport." Technical Report 6, Max Planck Institute for Biogeochemistry, Jena.
- Roedenbeck, C., S. Houweling, M. Gloor and M. Heimann (2003). "CO<sub>2</sub> flux history 1982-2001 inferred from atmospheric data using a global inversion of atmospheric transport." Atmospheric Chemistry and Physics **3**: 1919-1964.
- Roedenbeck, C., S. Houweling, M. Gloor and M. Heimann (2003). "Time-dependent atmospheric CO<sub>2</sub> inversions based on interannually varying tracer transport." Tellus Series B-Chemical and Physical Meteorology **55**(2): 488-497.
- Seibert, P., F. Beyrich, S. E. Gryning, S. Joffre, A. Rasmussen and P. Tercier (2000). "Review and intercomparison of operational methods for the determination of the mixing height." Atmospheric Environment **34**(7): 1001-1027.
- Stephens, B. B., K. R. Gurney, P. P. Tans, C. Sweeney, W. Peters, L. Bruhwiler, P. Ciais, M. Ramonet, P. Bousquet, T. Nakazawa, S. Aoki, T. Machida, G. Inoue, N. Vinnichenko, J. Lloyd, A. Jordan, M. Heimann, O. Shibistova, R. L. Langenfelds, L. P. Steele, R. J. Francey and A. S. Denning (2007). "Weak northern and strong tropical land carbon uptake from vertical profiles of atmospheric CO<sub>2</sub>." Science **316**(5832): 1732-1735.
- Tolk, L. F., A. Meesters, A. J. Dolman and W. Peters (2008). "Modelling representation errors of atmospheric CO<sub>2</sub> mixing ratios at a regional scale." Atmospheric Chemistry and Physics **8**(22): 6587-6596.

- Turnbull, J., P. Rayner, J. Miller, T. Naegler, P. Ciais and A. Cozic (2009). "On the use of (CO<sub>2</sub>)-C-14 as a tracer for fossil fuel CO<sub>2</sub>: Quantifying uncertainties using an atmospheric transport model." Journal of Geophysical Research-Atmospheres **114**.
- Wang, H., D. J. Jacob, M. Kopacz, D. B. A. Jones, P. Suntharalingam, J. A. Fisher, R. Nassar, S. Pawson and J. E. Nielsen (2009). "Error correlation between CO<sub>2</sub> and CO as constraint for CO<sub>2</sub> flux inversions using satellite data." Atmospheric Chemistry and Physics **9**(19): 7313-7323.

## **Chapter 5 Conclusions and future work**

Observations of atmospheric CO<sub>2</sub>, CH<sub>4</sub> and H<sub>2</sub>O concentrations are of central interest for understanding the global carbon cycle and the impact of these gases on climate change. Use of commercial airliners for routine airborne observations complements ground-based observations and strengthens the current global observational network for CO<sub>2</sub> and CH<sub>4</sub>. Within this thesis work, the design of a high-accuracy continuous analyzer for measuring atmospheric CO<sub>2</sub> and CH<sub>4</sub> aboard commercial airliners has been accomplished; starting from 2011, 7 aircraft will be implemented with the CO<sub>2</sub>/CH<sub>4</sub>/H<sub>2</sub>O analyzer within the IAGOS (In-service Aircraft for a Global Observing System) project. Furthermore, a joint CO<sub>2</sub>-CO inversion for carbon flux studies using observations from commercial airliner programs has been proposed based on the representativeness analysis.

### **Design of CO<sub>2</sub>/CH<sub>4</sub>/H<sub>2</sub>O instrumentation aboard commercial airliner**

The design for a high-accuracy continuous CO<sub>2</sub>/CH<sub>4</sub>/H<sub>2</sub>O analyzer aboard commercial airliners has been achieved based on improvements of a commercially available instrument using the cavity ring-down spectroscopy (CRDS) technique. The CRDS analyzer has been chosen to be installed aboard commercial airliners mainly because of its high stability, as shown in laboratory experiments and during a series of test flights in the BARCA (Balanço Atmosférico Regional de Carbono na Amazônia) campaign. The

precision of the CRDS analyzer for measurements of CO<sub>2</sub> and CH<sub>4</sub> meets the WMO recommendations.

Quadratic water correction functions have been derived from laboratory experiments, in which dry and humidified air were alternately sampled. Using the water vapor mixing ratios simultaneously measured by the CRDS, these water corrections have been proven to be fully adequate in correcting the dilution and pressure-broadening effects for both CO<sub>2</sub> and CH<sub>4</sub> during the BARCA campaign. Use of these water corrections eliminates any need for drying the sample air, which significantly reduces the maintenance and makes the CRDS analyzer more attractive for deployment aboard a commercial aircraft. These water corrections have been found to be transferable from one instrument to another when the measurements of H<sub>2</sub>O mixing ratios were placed on the same scale, and were proven to be stable over time. Furthermore, the water vapor measurements by the CRDS analyzer have been calibrated against a dew point mirror, providing the ability to monitor atmospheric water vapor concentrations.

### **Methods for validating airborne in situ CO<sub>2</sub> and CH<sub>4</sub> measurements**

One method for validation of in situ airborne CO<sub>2</sub> and CH<sub>4</sub> measurements is to compare them with the results from air samples that are taken during the same time period. The air samples are normally taken with flasks over 2-3 minutes and only one value can be obtained for each flask, while the in situ measurements are often reported every second. In order to compare each individual flask analysis result with in situ measurements over the 2-3 minutes, weighting functions have been derived for both single flask and paired

flasks. The basic assumption of instantaneous mixing of air in the flask has been proven by a laboratory experiment. These weighting functions have been shown to be able to account for the variability of in situ measurements during the period of flask sampling.

An alternative method for validation of in situ airborne CO<sub>2</sub> measurements is to compare measurements from two independent analyzers on board the same aircraft. For the comparison of in situ measurements of CO<sub>2</sub> concentrations made by the CRDS analyzer with those from an NDIR analyzer during BARCA, a series of corrections have been developed regarding the calibrations of the CRDS and the NDIR using synthetic air standards. First, the isotope effect for the CRDS due to the variation in <sup>13</sup>C<sup>16</sup>O<sub>2</sub> and <sup>12</sup>CO<sub>16</sub>O<sub>18</sub> is corrected using the isotope ratios in the synthetic air and ambient air. Second, the pressure-broadening effect for the CRDS due to the variation of composition of O<sub>2</sub>, N<sub>2</sub> and Ar in synthetic vs. ambient air is corrected using the measured absorption line widths. Last but not least, the isotope effect for the NDIR is also taken into account. Due to the necessity of correcting for the isotope and pressure-broadening effects for CO<sub>2</sub> concentration measurements of synthetic air that introduces non-negligible uncertainties, it is strongly recommended, based on these experiments, to use ambient air standards instead of synthetic air standards for calibrating the CRDS analyzer.

### **Routine accurate observations of in situ CO<sub>2</sub> near the Bialystok tall tower**

One commercially available CO<sub>2</sub> analyzer based on the non-dispersive infrared (NDIR) technique has also been assessed for measurements aboard commercial airliners, but failed to meet the requirements due to lack of stability. This NDIR analyzer has been



modified and deployed aboard a rental aircraft to perform regular profiling near the Bialystok tall tower. As a result of the automation of the analyzer, two profiles can be obtained per flight, at locations that are 20 km apart. The accuracy of the measurements is guaranteed by short and frequent calibrations. Note that a strategy for flushing the calibration gases at the beginning of each flight has been employed based on laboratory investigations to remove any potential drift of calibration gases in the regulator. These in situ observations provide information about the actual mixing of the atmosphere and can be used to validate transport models. In addition, regular profiles at two different locations enable the assessment of both spatial and temporal variations of atmospheric CO<sub>2</sub> at this particular site. The variations of mixed-layer mean CO<sub>2</sub> for the two locations near Bialystok is 1.2 ppm for summer months and 0.6 ppm for spring and autumn months. The temporal difference between the two profiles is significant for the summer months but not significant for the spring and autumn months.

### **Representativeness analysis of observations from commercial airliner programs**

To investigate whether the observations from a commercial airliner program are regionally representative, CO profiles over Frankfurt from the Measurement of OZone and water vapor by AIrbus in-service airCraft (MOZAIC) project are assessed as a proxy for fossil fuel CO<sub>2</sub> using the stochastic time-inverted Lagrangian transport (STILT) model coupled with a fossil fuel CO emission inventory. The analyses show that measurements in the upper half of the PBL are regionally representative since the model simulations for these data do not depend on the model resolution. The model is underestimating CO enhancements, which can only be explained by an underestimation

of fossil fuel emissions in the inventory after excluding other potential causes, such as the model setup, transport uncertainties, or missing emission sources.

The representation errors of fossil fuel CO<sub>2</sub> for profiles from Frankfurt (0.8 ppm for the upper half of the PBL) and from BIK (0.1 ppm) are estimated based on the differences between simulated CO<sub>2</sub> from a high-resolution model run and from the degraded runs. Moreover, the total uncertainties of fossil fuel CO<sub>2</sub> for the upper half of the PBL over Frankfurt (2.1 ppm) and for BIK (0.7 ppm) provide upper bounds for the uncertainties caused by fossil fuel emissions. The total uncertainties of fossil fuel CO<sub>2</sub> are smaller than the total uncertainty of biospheric CO<sub>2</sub> at BIK (3.8 ppm). The representation error derived from the variability of the differences of the mixed-layer average CO<sub>2</sub> from profiles 20 km apart at BIK shows larger values (1.2 ppm during the peak growing season and 0.6 ppm during the non-peak growing season) than the representation error of fossil fuel (0.1 ppm) or of vegetation CO<sub>2</sub> (0.3 ppm) at a scale of 80 km at the same site. The variations in fossil fuel or biospheric fluxes across the city of Bialystok may be responsible for this.

To deal with the unresolved variability of fossil fuel CO<sub>2</sub> from a commercial airliner program, a joint CO<sub>2</sub>-CO inversion is suggested. With the additional information about the fossil fuel emissions provided by CO observations, such a joint inversion is expected to be able to optimize both anthropogenic and biospheric CO<sub>2</sub> fluxes simultaneously.

## **Future work**

The design of CO<sub>2</sub>/CH<sub>4</sub>/H<sub>2</sub>O instrumentation for commercial airliner programs can be configured to measure other species and isotopes in the future. Several other species are useful in helping understand processes of the carbon cycle; for example, C<sub>2</sub>H<sub>2</sub> is a good tracer for biomass burning and COS can be used to constrain photosynthetic uptake of CO<sub>2</sub> by plants. Currently, the CRDS technique is not sensitive enough to detect trace gases with extremely low concentrations; however, efforts have been made to use the CRDS technique to detect absorptions in the mid-IR range, which has greatly improved the sensitivity for measuring N<sub>2</sub>O and is promising for other trace gases.

Once the CO<sub>2</sub>/CH<sub>4</sub>/H<sub>2</sub>O analyzer is implemented aboard the commercial aircraft, a large number of profiles over many major airports will be obtained. The CO<sub>2</sub> profiles, together with CO profiles, can be employed in a joint CO<sub>2</sub>-CO inverse modeling framework to derive both anthropogenic and biospheric carbon fluxes.

## Appendix A

The following presents a detailed description of deriving the weighting functions for integrating in situ measurements for comparison with single and paired flask measurements based on two assumptions during the flask sampling process: 1) instantaneous mixing of incoming air with the existing air in the flasks 2) the change of temperature in the flasks is negligible.

### A1. Single flask model

The weighting function for integrating in situ measurements to compare with a single flask measurement is divided into two parts based on the processes during flask sampling: flushing and pressurizing (see Fig. 3.3). When the flask sampling is completed, the influence of remaining conditioning air on the CO<sub>2</sub> mixing ratio in the flask is negligible. The concentration of CO<sub>2</sub> in the flask is determined by the CO<sub>2</sub> concentrations of sampling air since the beginning of flushing until pressurizing is complete, weighted by a function. The CO<sub>2</sub> mixing ratio within the flask can be written as:

$$\begin{aligned} \langle CO_2 \rangle &= \int_0^{t_e} CO_2(t) \times W(t) dt \\ &= \int_0^{t_s} CO_2(t) \times W_f(t) dt + \int_{t_s}^{t_e} CO_2(t) \times W_p(t) dt \end{aligned} \quad (A.1)$$

where  $\langle CO_2 \rangle$  is the CO<sub>2</sub> concentration of the air in the flask;  $t_s$  and  $t_e$  are the time when the pressurizing process starts and ends;  $W(t)$  is the weighting function that consists of  $W_f(t)$  and  $W_p(t)$ , for the flushing and the pressurizing periods, respectively.

The weighting function is proportional to the volume of the air (entering the flask at time  $t$ ) in the flask, i.e., the volume of sampling air flowing into the flask at time  $t$  multiplied by the fraction of the air that is preserved in the flask, given the volume is given at the same pressure. The sum of the overall weighting function is normalized to 1.

During the flushing period ( $0 < t < t_s$ ), the incoming air mixes with the air in the flask and flows through the flask. When the pressurizing starts ( $t = t_s$ ), the air already in the flask is preserved. Because the flushing period is short (around 2 minutes), the ambient air pressure and the volume flow rate can be regarded as constants, i.e.,  $f(t) = f_0$ ,  $p(t) = p_s$ . The mass balance for air in the flask at any time  $t$  can be written as:

$$V \cdot \frac{dc(t')}{dt'} = -f_0 \cdot c(t') \quad (\text{A.2})$$

where  $c(t')$  is, at any given time  $t'$  ( $t < t' < t_s$ ), the fraction of the air (in the flask at time  $t$ ) remaining in the flask, given the boundary condition  $c(t' = t) = 1$ ;  $V$  is the volume of the flask, and  $f_0$  is the volume flow rate at the ambient pressure  $p_s$ .

The solution of the equation:

$$c(t', t) = e^{-(t'-t)/\tau}, \quad \tau = \frac{V}{f_0} \quad (\text{A.3})$$

At the end of the flushing period, i.e.,  $t' = t_s$ , the fraction of the air (in the flask at time  $t$ ) remaining in the flask is

$$c(t_s, t) = e^{-(t_s-t)/\tau} \quad (\text{A.4})$$

According to Eq.A.4, for the air entering the flask at any given time  $t$  (with the volume  $f_0 \cdot dt$ ), the remaining volume in the flask at time  $t_s$  is  $f_0 \cdot dt \cdot e^{-(t_s-t)/\tau}$ . The weighting function  $W_f(t)$  is then proportional to  $f_0 \cdot dt \cdot e^{-(t_s-t)/\tau}$ :

$$W_f(t) \sim e^{-(t_s-t)/\tau} \quad (\text{A.5})$$

During the pressurizing process, all incoming air is kept in the flask until the whole flask sampling process is completed (see Fig. 3.3). The weighting function  $W_p(t)$  is thus proportional to the volume flow rate, for which mass balance gives:

$$W_p(t) \sim f(t) = \frac{V}{P_s} \cdot \frac{dp(t)}{dt} \quad (\text{A.6})$$

where  $p_s$  is the ambient pressure before the pressurizing period starts,  $f(t)$  is the volume flow rate at the pressure of  $p_s$ , and  $p(t)$  is the air pressure in the flask.

When the flask sampling is completed, the flask pressure is  $P_s$ , and the fraction of all flushing air in the flask is

$$F_1 = \frac{P_s}{P_e} \quad (\text{A.7})$$

and the fraction of all pressurizing air in the flask is

$$F_2 = 1 - \frac{P_s}{P_e} \quad (\text{A.8})$$

Based on Eqs.A.5-8, the weighting coefficients for integrating in situ measurements to compare with one single flask is described as

$$\begin{aligned}
W(t) &= \begin{cases} W_1(t) = \frac{p_s}{p_e} \cdot e^{-(t_s-t)/\tau} / \int_0^{t_s} e^{-(t_s-t)/\tau} dt & 0 < t < t_s \\ W_2(t) = \left(1 - \frac{P_s}{P_e}\right) \cdot \frac{dp(t)}{dt} / \int_{t_s}^{t_e} \frac{dp(t)}{dt} dt & t_s \leq t < t_e \end{cases} \\
&= \begin{cases} W_1(t) = \frac{p_s}{p_e} \cdot \frac{1}{\tau} e^{-(t_s-t)/\tau} / \left(1 - e^{-t_s/\tau}\right), \tau = \frac{p_s}{\frac{dp(t_s)}{dt}} & 0 < t < t_s \\ W_2(t) = \frac{1}{p_e} \cdot \frac{dp(t)}{dt} & t_s \leq t < t_e \end{cases} \quad (\text{A.9})
\end{aligned}$$

## A2. Paired flask model

The weighting coefficients for integrating in situ measurements to compare with paired flask measurements are also divided into two parts during the flask sampling: flushing and pressurizing; however, the situations for the upstream and the downstream flasks are different and need to be considered separately.

The CO<sub>2</sub> mixing ratio within the flask can be written as:

$$\begin{aligned}
\langle CO_2 \rangle_{1,2} &= \int_0^{t_e} CO_2(t) \times W_{1,2}(t) dt \\
&= \int_0^{t_s} CO_2(t) \times W_{1,2f}(t) dt + \int_{t_s}^{t_e} CO_2(t) \times W_{1,2p}(t) dt \quad (\text{A.10})
\end{aligned}$$

where the subscripts 1 or 2 denotes the upstream and the downstream flasks respectively.

### A2.1 Upstream flask

During the flushing period, the situation for the upstream flask is the same as in the single flask model and the weighting function  $W_{1f}$  is proportional to

$$c_1(t) = e^{-(t_s-t)/\tau} \quad (\text{A.11})$$

During the pressurizing period, the process for the upstream flask is a combination of a flushing process and a pressurizing process due to the fact that part of the air from the upstream flask leaves into the downstream flask at half of the flow rate (see Fig. 3.5).

For air in the flask at any given time  $t$ , ( $t_s < t < t_e$ ), the mass balance equation gives:

$$\frac{d\left(V \cdot \frac{p(t)}{p_s} \cdot c_1'(t')\right)}{dt'} = -\frac{f(t')}{2} \cdot \frac{p(t)}{p(t')} \cdot c_1'(t') \quad (\text{A.12})$$

$c_1'(t')$  is the fraction of the air (in the flask at time  $t$ ) remaining in the flask at any given time  $t'$  ( $t < t' < t_e$ ), and  $f(t')$  is the volume flow rate (at pressure  $p_s$ ) of sampling air.

Besides,  $f(t')$  and  $p(t')$  are constrained by the equation

$$\frac{1}{2} \cdot f(t') = \frac{V}{p_s} \cdot \frac{dp(t')}{dt'} \quad (\text{A.13})$$

Combining Eq.A.8 and Eq.A.9:

$$\frac{dp(t')}{dt'} \cdot c_1'(t') + p(t') \cdot \frac{dc_1'(t')}{dt'} = 0 \quad (\text{A.14})$$

The solution of Eq.A.10 is:

$$c_1'(t', t) = \frac{p(t)}{p(t')} \quad (\text{A.15})$$

When the flask sampling is completed, i.e.,  $t' = t_e$ , the pressure reaches its final value,  $p_e$ , the fraction of the air (in the flask at time  $t$ ) remaining in the flask is

$$c_1'(t_e, t) = \frac{p(t)}{p_e} \quad (\text{A.16})$$

According to Eq.A.14, for the air entering the flask at any given time  $t$  (with the volume  $f_0 \cdot dt$ ), the remaining volume in the flask at time  $t_e$  is  $f_0 \cdot dt \cdot \frac{p(t)}{p_e}$ . The



weighting function  $W_{1p}(t)$  is then proportional to  $\frac{p(t)}{P_e}$ , i.e., Eq.A.14. The fractions of the flushing air remaining in the upstream flask at the time  $t_s$  and the fractions of pressurizing air in the downstream flask at the time  $t_e$  are shown in Fig. A1.

When  $t = t_e$ , the fraction of the air (entering the upstream flask at time  $t$ , with the volume of  $f(t) \cdot dt$ ) remaining in the upstream flask is  $\frac{p(t)}{P_e}$ , and the fraction flowing into the downstream flask is  $1 - \frac{p(t)}{P_e}$ .

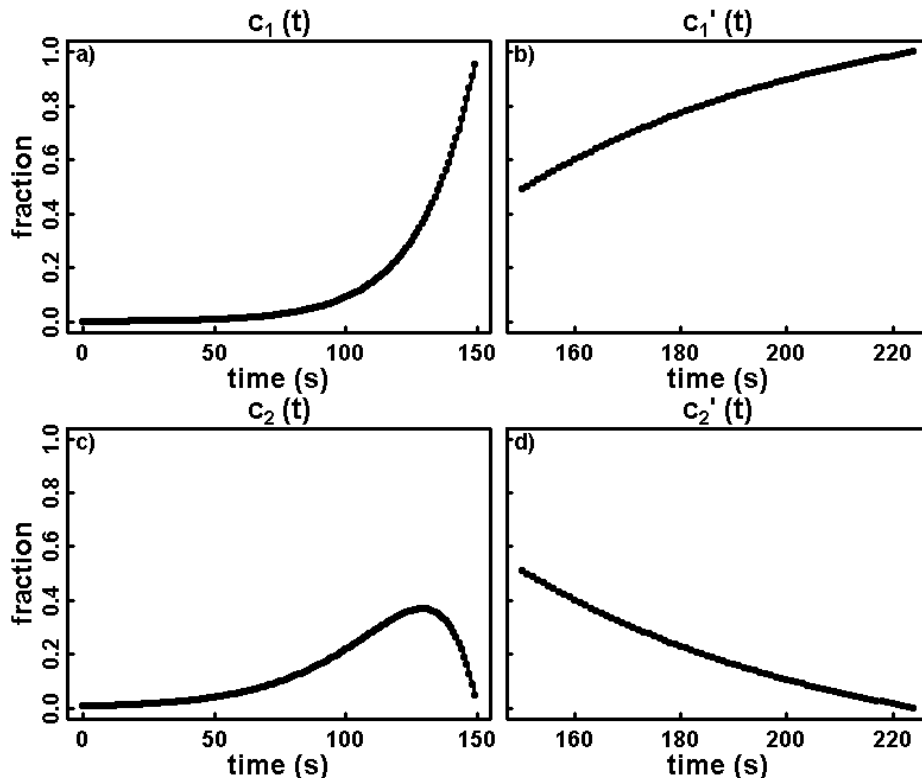


Figure A.1. The fraction of the air (entering the upstream flask at time  $t$ ) remaining in the flasks: at the time when the pressurizing period starts,  $t_s$ , the fraction of the flushing air remaining (a) in the upstream flask,  $c_1(t)$  and (c) in the downstream flask; at the time when the pressurizing is complete,  $t_e$ , the fraction of the pressurizing air remaining (b) in the upstream  $c_1'(t)$  and (d) in the downstream  $c_2'(t)$ . Note that at the time when the pressurizing period ends, the fraction of the flushing air in the upstream and the

downstream flask will be different as a result of flushing air moving from the upstream flask into the downstream flask.

When the flask sampling is completed, the flask pressure is  $p_e$ , and the fraction of all flushing air in the flask is

$$F_{1f} = \frac{P_s}{P_e} / \frac{P_e}{P_s} = \left(\frac{P_s}{P_e}\right)^2 \quad (\text{A.17})$$

and the fraction of all pressurizing air in the flask is

$$F_{1p} = 1 - \left(\frac{P_s}{P_e}\right)^2 \quad (\text{A.18})$$

Based on Eq.A.4, A.14-16, the weighting function for integrating in situ measurements to compare with the upstream flask is described as

$$W_1(t) = \begin{cases} W_{1f}(t) = \left(\frac{p_s}{p_e}\right)^2 \cdot e^{-(t_s-t)/\tau} / \int_0^{t_s} e^{-(t_s-t)/\tau} dt & 0 < t < t_s \\ W_{1p}(t) = \left(1 - \left(\frac{p_s}{p_e}\right)^2\right) \cdot \frac{dp(t)}{dt} \cdot \frac{p(t)}{p_e} / \int_{t_s}^{t_e} \frac{dp(t)}{dt} \cdot \frac{p(t)}{p_e} dt & t_s \leq t < t_e \end{cases}$$

$$= \begin{cases} W_{1f}(t) = \left(\frac{p_s}{p_e}\right)^2 \cdot \frac{1}{\tau} e^{-(t_s-t)/\tau} / \left(1 - e^{-t_s/\tau}\right), \tau = \frac{p_s}{2 \cdot \frac{dp(t_s)}{dt}} & 0 < t < t_s \\ W_{1p}(t) = \frac{2 \cdot p(t)}{p_e^2} \cdot \frac{dp(t)}{dt} & t_s \leq t < t_e \end{cases} \quad (\text{A.19})$$

## A2.2 Downstream flask

During the flushing period ( $0 < t < t_s$ ), the incoming air mixes with the air in the upstream flask and flows through the downstream flask. When the pressurizing starts ( $t = t_s$ ), the air already in the downstream flask is preserved. The mass balance for the air in the *upstream* flask at any time  $t$  can be written as:

$$V \cdot \frac{dc_2(t')}{dt'} = f_0 \cdot c_1(t') - f_0 \cdot c_2(t') \quad (\text{A.20})$$

where  $c_1(t')$ ,  $c_2(t')$  are, at any given time  $t'$  ( $t < t' < t_s$ ), the fractions of the air (in the upstream flask at time  $t$ ) remaining in the upstream and the downstream flasks, respectively, given the boundary condition  $c_1(t) = 1$ ,  $c_2(t) = 0$ ;  $V$  is the volume of the flask, and  $f_0$  is the volume flow rate at the ambient pressure  $p_s$ .

The solution of the equation is

$$c_2(t', t) = \frac{t' - t}{\tau} \cdot e^{-(t' - t)/\tau}, \tau = \frac{V}{f_0} \quad (\text{A.21})$$

At the end of the flushing period, i.e.,  $t' = t_s$ , the fraction of the air (in the upstream flask at time  $t$ ) remaining in the downstream flask is

$$c(t_s, t) = \frac{t_s - t}{\tau} \cdot e^{-(t_s - t)/\tau}, \tau = \frac{V}{f_0} \quad (\text{A.22})$$

According to Eq.A.20, for the air entering the upstream flask at any given time  $t$  (with the volume  $f_0 \cdot dt$ ), the remaining volume in the downstream flask at time  $t_s$  is  $f_0 \cdot dt \cdot \frac{t_s - t}{\tau} \cdot e^{-(t_s - t)/\tau}$ . Besides, a fraction of flushing air in the upstream flask flows into the downstream flask during the pressurizing period, and according to Eq.A.14, at time  $t_e$ , the fraction of the air (in the upstream flask at time  $t_s$ ) flowing into the downstream flask is  $1 - \frac{p_s}{p_e}$ . As a result, at time  $t_e$ , for the air entering the upstream flask at any given time  $t$  (with the volume  $f_0 \cdot dt$ ), the remaining volume in the downstream flask is  $f_0 \cdot dt \cdot \left( \frac{t_s - t}{\tau} \cdot e^{-(t_s - t)/\tau} + \left(1 - \frac{p_s}{p_e}\right) \cdot e^{-(t_s - t)/\tau} \right)$ , which is proportional to the weighting function  $W_{2f}(t)$ :

$$W_{2f}(t) \sim \left( \frac{t_s - t}{\tau} \cdot e^{-(t_s - t)/\tau} + \left(1 - \frac{p_s}{p_e}\right) \cdot e^{-(t_s - t)/\tau} \right) \quad (\text{A.23})$$

During the pressurizing period, the fraction of the air (in the upstream flask at time  $t$ ) coming into the downstream flask can be derived from Eq.A.14:

$$c'_2(t_e, t) = 1 - \frac{p(t)}{P_e} \quad (\text{A.24})$$

According to Eq.A.21, for the air entering the flask at any given time  $t$  (with the volume  $f(t) \cdot dt$ ), the weighting function  $W_{2p}(t)$  is then proportional to  $f(t) \cdot dt \cdot \left(1 - \frac{p(t)}{P_e}\right)$ :

$$W_{2p}(t) \sim f(t) \cdot \left(1 - \frac{p(t)}{P_e}\right) \sim \frac{dp(t)}{dt} \cdot \left(1 - \frac{p(t)}{P_e}\right) \quad (\text{A.25})$$

When the flask sampling is completed, the flask pressure is  $p_s$ , and the fraction of flushing air in the downstream flask is

$$F_{2f} = \frac{V + V \cdot \left(1 - \frac{p_s}{P_e}\right)}{V \cdot \frac{p_e}{p_s}} = 2 \cdot \frac{p_s}{p_e} - \left(\frac{p_s}{p_e}\right)^2 \quad (\text{A.26})$$

and the fraction of pressurizing air in the downstream flask is

$$F_{2p} = 1 - F_{2f} = \left(1 - \frac{p_s}{P_e}\right)^2 \quad (\text{A.27})$$

Based on Eqs.A.23 and A.25-27, the weighting function for the downstream flask is described as:

$$W_2(t) = \begin{cases} W_{2f}(t) = \left(2 \cdot \frac{p_s}{p_e} - \left(\frac{p_s}{p_e}\right)^2\right) \cdot \frac{\left(\frac{t_s - t}{\tau} \cdot e^{-(t_s - t)/\tau} + \left(1 - \frac{p_s}{P_e}\right) \cdot e^{-(t_s - t)/\tau}\right)}{\int_0^{t_s} \left(\frac{t_s - t}{\tau} \cdot e^{-(t_s - t)/\tau} + \left(1 - \frac{p_s}{P_e}\right) \cdot e^{-(t_s - t)/\tau}\right) dt} & 0 < t < t_s \\ W_{2p}(t) = \left(1 - \frac{p_s}{P_e}\right)^2 \cdot \frac{\frac{dp(t)}{dt} \cdot \left(1 - \frac{p(t)}{P_e}\right)}{\int_{t_s}^{t_e} \frac{dp(t)}{dt} \cdot \left(1 - \frac{p(t)}{P_e}\right) dt} & t_s \leq t < t_e \end{cases}$$

$$= \begin{cases} W_{2f}(t) = \left(2 \cdot \frac{p_s}{p_e} - \left(\frac{p_s}{p_e}\right)^2\right) \cdot \frac{\left(\frac{t_s-t}{\tau} \cdot e^{-(t_s-t)/\tau} + \left(1 - \frac{p_s}{p_e}\right) \cdot e^{-(t_s-t)/\tau}\right)}{\left(2 - \frac{p_s}{p_e}\right) \cdot \tau \cdot \left(1 - e^{-t_s/\tau}\right) - t_s \cdot e^{-t_s/\tau}}, \tau = \frac{p_s}{2 \cdot \frac{dp(t_s)}{dt}} & 0 < t < t_s \\ W_{2p}(t) = \frac{2}{p_e} \cdot \frac{dp(t)}{dt} \cdot \left(1 - \frac{p(t)}{p_e}\right) & t_s \leq t < t_e \end{cases}$$

(A.28)

## **Acknowledgements**

This thesis would not have been possible without encouragement and support from many people. First of all, I am heartily thankful to my thesis advisor, Christoph Gerbig, for his guidance throughout my Ph.D. study. He has introduced me into the field of atmospheric science and provided an insightful view of studying the global carbon cycle. I especially thank him for facing difficulties together with me, and with an optimistic attitude. I am strongly impressed by his broad knowledge, extensive experience, and the ability of performing both experimental and modeling work with high scientific standards. His intelligence, kindness, and encouragement will always inspire me. It has been an honor to work with him.

Furthermore, I am very grateful to Prof. Martin Heimann, Prof. Wolfgang Weigand, and Karl Kuebler for active participants in my regular Ph.D. advisory committee meeting. I am thankful for their overall thinking on my thesis, help in the strategy plan, as well as specific useful recommendations. I have learned from them how to fulfill the requirements for getting a PhD degree. Without their generous contribution, this thesis would not have come to a good shape in a reasonable period.

Special thanks are given to Julia Steinbach who introduced to me many things in the laboratory, in our institute, and in Jena when I started at the Max Planck Institute for Biogeochemistry. I would like to thank Jan Winderlich for the wonderful collaboration on the laboratory work and numerous discussions on scientific issues. It has been a pleasure for me to share the office with Julia and Jan for more than 3 years. They are

always kind in assisting me in occasions when I have German language problems, and I am grateful for their help in translating the abstract of my thesis into German.

I feel grateful for many of my colleagues who supported me. I would like to thank Julia Marshall who did amazing proof-reading for my thesis and gave me lots of comments. I thank Reimo Leppert, Frank Voigt, Bernd Schloeffel, Falk Haensel, Michael Hielscher, and René Schwalbe for supporting me in testing the analyzers in the laboratory and I am very grateful for the support from Olaf Kolle and Martin Hertel in the field experiment. I would like to thank Marc Geibel for helping me drive during the “car experiment”. I thank Stephan Baum for getting me the flask analysis results. I am grateful for the help of Annette Hoefler in the water vapor test experiment. I am thankful for the discussions with Willi A. Brand, Armin Jordan, and Bert Steinberg about gas analysis techniques. I feel grateful for the discussions on my modeling work with Ute Karstens, Christian Roedenbeck, Roberto Kretschmer, Dhanyalekshmi Kuttappan Pillai, Veronika Beck, and the programming support from Thomas Koch. I appreciate the help from Lavrič Jošt for presenting my poster at EGU2010 when I was writing my thesis. I am grateful for general discussions with Dietrich Feist, Ravan Ahmadov, Bakr Badawy, Valentina Sicardi, Kristina Trusilova, Rona Thompson, and Gionata Biavati, Gregor Schuermann, and Soenke Zaehle.

I am grateful for the strong support from Aaron Van Pelt, Chris Rella, and Eric Crosson from Picarro Inc. I am thankful for the great collaboration with the BARCA team (Steve C. Wofsy, Victoria Y. Chow, Elaine W. Gottlieb, Bruce C. Daube, Greg W. Santoni, Marcos Longo, Pedro Celso, Daniel Gramacho, Paulo Artaxo, Fernando Morais, Alcides

C. Ribeiro, Karla Longo, Kenia Wiedemann, Megan M. Bela, J. William Munger, Meinrat O. Andreae, Niklas Juergens). Special thanks go to Steve C. Wofsy for his valuable ideas and full support for my research work. I am thankful for the discussions and information sharing with Colm Sweeney and Anna Karion. I thank Krzysztof Katrynski for assisting in getting regular aircraft measurements and Elena Popa for providing me the data from the tall tower at Bialystok. This work was supported by the European Commission through the IAGOS project. I feel grateful for the help and support from Hans-Werner Paetz, Herman Smit, and Andreas Volz-Thomas from the institute of chemistry and dynamics of the geosphere in the Juelich research center.

I would like to take the opportunity to thank the IT department for the support to the computing, the library staff to help me get access to literatures, Bodo Wild for ordering many stuff, and Andreas Kramer for organizing all the shipments. I am grateful to Karen Harm for assisting me in organizing my trips, to Corinne Sacher for managing my project-related stuff, and to Silvana Schott for helping me with the design of my posters, presentations, and webpage.

I wish to thank all my friends in Jena. The list of individuals will be beyond the page limit, but I give special thanks to Youmin Chen, Dabang Jiang, Kewei Yang, Ming Chen and Ben Herzog, for their heartfelt friendships.

Finally, I owe my deepest gratitude to my wife Mengsu Huang for her full support during my Ph.D. study. Without her love and understanding, this thesis would not have been completed. I am indebted to my parents for their understanding and support.



# CURRICULUM VITAE

## Education:

- 2006 – present    Max Planck Institute for Biogeochemistry, Jena, Germany
- 2006 – present    Friedrich Schiller University of Jena, Jena, Germany
- 2002 – 2005        Tsinghua University, Beijing, China  
Master in Electronic Engineering
- 1998 – 2002        University of Science and Technology of China, Hefei, China  
Bachelor in Theoretical and Applied Mechanics  
Bachelor in Electronic Information Science (secondary)

## Publications&Patent:

- **Chen, H.**, Winderlich, J., Gerbig, C., et. al: High-accuracy continuous airborne measurements of greenhouse gases (CO<sub>2</sub> and CH<sub>4</sub>) using the cavity ring-down spectroscopy (CRDS) technique, Atmos. Meas. Tech., 3, 375-386, 2010
- Winderlich, J., **Chen, H.**, Gerbig, C., et. al: Continuous low-maintenance CO<sub>2</sub>/CH<sub>4</sub>/H<sub>2</sub>O measurements at the Zotino Tall Tower Observatory (ZOTTO) in Central Siberia, Atmos. Meas. Tech., 3, 1113-1128, 2010
- Li Zhang, **Huilin Chen**, Chao Wu, Liang Xun. An Approach to Achieving Graphics & Texts Carving using Computer's Virtual Printing Technology. Patent: Publication number: CN1588276,2005

Jena, 30.09.2010

Huilin Chen

## **Selbständigkeitserklärung**

Ich erkläre, dass ich die vorliegende Arbeit selbständig und unter Verwendung der angegebenen Hilfsmittel, persönlichen Mitteilungen und Quellen angefertigt habe.

Jena, 30.09.2010

Huilin Chen